Università degli Studi di Napoli Federico II
Dipartimento di Scienze Fisiche

Tesi di Dottorato in Fisica Fondamentale ed Applicata

Determination of the $pp \to ZX \to \mu^+\mu^- X$ inclusive cross section with a simultaneous fit of Z yield, muon reconstruction efficiencies and High Level Trigger efficiency.

Pasquale Noli

Tutor:
Chiar.mo Prof. C. Sciacca
Chiar.mo Dr. L. Lista
Chiar.mo Dr. F. Fabozzi

Coordinatore:
Chiar.mo Prof. L. Marrucci

XXII ciclo 2006-2009

Contents

Introduction

The behaviour of all known subatomic particles can be described within a single theoretical framework called the Standard Model. This quantum field theory incorporates the constituents of matter which are classified in two different fermion families, quarks and leptons, and the fundamental forces except the gravity, mediated by boson particles which are introduced via the requirement for the theory to be invariant under local gauge transformations. Although the Standard Model has been experimentally tested at the per mille level accuracy by the high-precision measurements of the last decades carried out at LEP, SLC, HERA, and Tevatron, it remains not completely satisfactory. A cornerstone of the Standard Model is the mechanism of spontaneous electroweak symmetry breaking proposed to generate the masses of all the observed elementary particles by introducing a doublet of complex scalar fields. This so-called Higgs mechanism predicts the existence of one scalar particle, the Higgs boson, whose mass is the only unknown fundamental parameter of the theory. However, the Higgs particle has not been observed in experiments so far and only indirect constraints on its mass have been inferred from the high-precision data. Moreover, there are several phenomena that induce to believe that the Standard Model is only an effective description of the structure of matter up to an energy scale $\Lambda \sim TeV$, and that, therefore, there must be a truly fundamental underlying theory. Most of the extensions of the theory that have been proposed to solve the shortcomings of the Standard Model, have a common intriguing feature: they predict the existence of new particles with mass of the order of TeV/c^2, whose production requiring energies higher than those reached by past and present particle accelerators. This led to the design of the Large Hadron Collider (LHC), a high-energy, high-luminosity proton-proton collider, which is being installed at the European Laboratory for Nuclear Research ($CERN$) in Geneva and that in these days, end of november of 2009, is getting ready to operate. With a designed center-of-mass collision energy of $\sqrt{s} = 14\ TeV$ and a luminosity of $10^{34} cm^{-2} s^{-1}$, it is a machine of unprecedented complexity and potential. It will be the first accelerator to provide parton-parton collisions up to energies of about 1 TeV, the energy scale relevant to electroweak symmetry breaking and at which New Physics are expected to appear. In order to carry out the whole scientific programme of LHC, four big experiments are built in the as many four beams interaction points: AL-

ICE, ATLAS, CMS, and LHCb. CMS, acronym of Compact Muon Solenoid, is a multi-purpose experiment developed inside and around a high-field solenoid that provides a magnetic field of 4 Tesla. Like most modern particle detectors, CMS is composed by many sub-detectors generally grouped into inner tracker, calorimetry and muon system. The main distinguishing features of CMS are a full-silicon-based inner tracking system ever built, a homogeneous scintillating-crystals-based electromagnetic calorimeter that, united to the high-field solenoid, allows excellent muon and charged-particle identification and momentum resolution, good electromagnetic energy resolution, and good missing-transverse-energy measurements. These features will allow CMS to carry out of the full LHC physics programme.

The inclusive production of vector gauge bosons W and Z with their subsequent leptonic decay will be among the first physical signals to be measured at CMS. Characterized by relatively large cross-sections and clean and simple experimental signatures coupled with precise theoretical predictions, they will be the ″Standard Candle ‶measurements of LHC. They will be essential for the calibration of the detectors and to establish their performance. Events containing Z boson also constitute the main source of background for the Higgs searches in the so-called ″golden-plate ‶channel ($H \rightarrow 4\mu$) as well as in many searches beyond the Standard Model. Therefore a precise understanding of Z boson production processes is critical before any discovery can be made.

This thesis is set in a such context . The aim is the development of an entirely data-driven analysis strategy for the inclusive $Z \rightarrow \mu^+\mu^-$ cross section measurement. This analysis has to be robust and to be applied to the first data taken at LHC. he analysis method is based on a simultaneous fit of the yield of $Z \rightarrow \mu^+\mu^-$ events and the average reconstruction muon efficiencies in the tracker and in the muon detector, as well as the isolation cut and trigger efficiencies without depending on Monte Carlo simulation. The fit strategy foresees a classification of events with at least one reconstructed $Z \rightarrow \mu^+\mu^-$ candidate in suitable different categories. The yields of these samples are related in different ways to the efficiencies to be determined. In addition the Z peak shape model in each of these samples is not parameterized according to a-priori Monte Carlo function, but is sampled from the data.

The thesis is organized in four chapters: the first two chapters are focused on the detailed description of the main topics of the LHC physics programme, as well as the accurate description of LHC and CMS, underlying their peculiarities and performances. In the third chapter the reconstruction of muons and Z boson decaying into a muon pair is described. The performances of the reconstruction algorithms are shown as well as the kinematic properties of reconstructed muons and Z bosons. In the last chapter the analysis strategy is minutely described. The fit performances are stadied both comparing the results of different analysis on data sample corresponding at different integreted luminosities, and through a accurate toy Monte Carlo analysis. Finally a first study on the systematic error

affecting the cross section measurement is reported.

Chapter 1

Physics at Large Hadron Collider

The *Standard Model* [1, 2, 3] of particle physics is a Quantum Field Theory based on a $SU(3)_c \otimes SU(2)_L \otimes U(1)_Y$ *local gauge symmetry* that describes the fundamental building blocks of matter and their interaction. The above symmetry can be satisfied only if the matter and the interaction fields are massless: a mechanism known as *spontaneous symmetry breaking* is used in the Standard Model to provide elementary particles with mass. This mechanism requires the existence of a new, still unobserved, field known as *Higgs* field.

Although the Standard Model has been verified with remarkable accuracy, i.e. to precision of order of 0.1% or better in most cases, by experiments performed at various machines (e.g. LEP collider), the Standard Model could not be the ultimate theory of elementary particles and their interactions. There are, indeed, numerous indications about this: the recent evidence of atmospheric [4] and solar [5] neutrino oscillations, and the unability of the Standard Model to give satisfactory answers to fundamental questions [6] such as the baryogenesis and the matter-antimatter asymmetry in the universe, the origin of dark matter, the size of the cosmological constant, and the unification of fundamental interactions.

This chapter is a brief introduction to the Standard Model with the aim of introducing the physics program that the *Large Hadron Collider* [7] is expected to explore. The Large Hadron Collider, instead, will be presented in the chapter 2.

1.1 The Standard Model of Particle Physics

The Standard Model of elementary particles is a very successful description of the interactions of the fundamental components of matter. It is a relativistic quantum field theory that describes the interactions of fundamental fermions (quarks and leptons), mediated by gauge vector bosons (see Fig. 1.1). Quarks are triplets under the $SU(3)_c$ group, and therefore undergo strong interactions.

Leptons, on the other hand, are singlets under $SU(3)_c$. The left-handed states

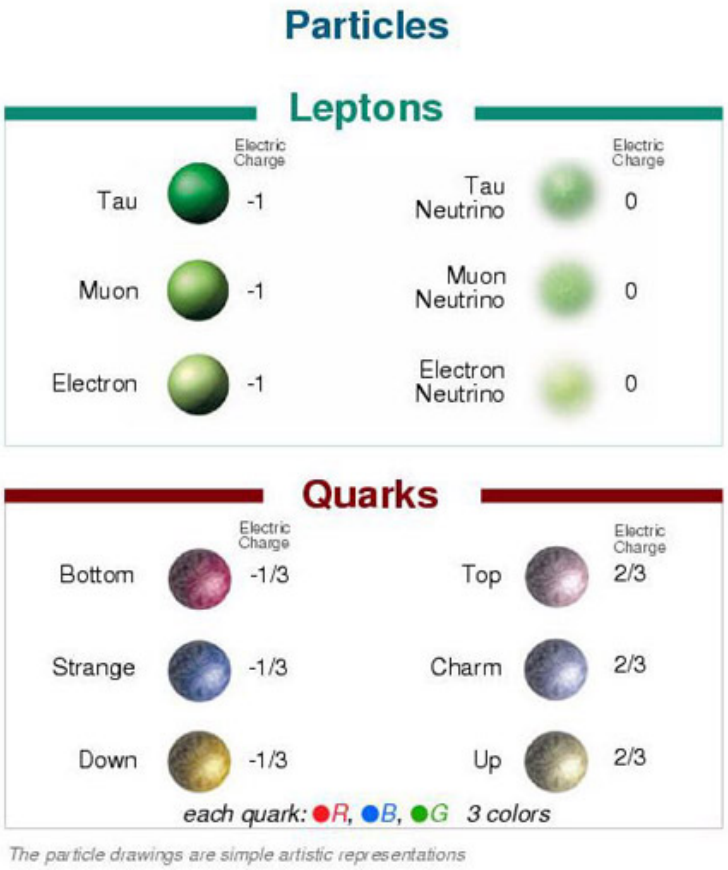

Figure 1.1: *Fundamental fermions.*

of fermions are $SU(2)_L$ doublets, while their right-handed partners transform as $SU(2)_L$ singlets. Right-handed and left-handed fermions forms different multiplets of the $SU(2)_L$ group, describing parity violation within the theory framework. The Standard Model includes three generations or families of fermions, all of them identical except for the mass.

The existence of the gauge bosons and the form of their interactions are dictated by local gauge invariance, a manifestation of the symmetry group of the theory, $SU(3)_c \otimes SU(2)_L \otimes U(1)_Y$. It combines the electroweak theory proposed by Glashow, Salam and Weinberg to describe the electromagnetic and weak interactions, based on the gauge symmetry group $SU(2)_L \otimes U(1)_Y$, with Quantum Chromodynamics, which is the theory of the strong interactions and is based on the symmetry group $SU(3)_c$. The theory is perturbative at sufficiently high energies and renormalizable, and thus describes these interactions at the quantum level.

1.1.1 The simplest gauge theory: the Quantum Electro-Dynamics

Consider a Lagrangian density [8]

$$L_0 = \overline{\psi}(x)\left(i\gamma^\mu\partial_\mu - m\right)\psi(x) \tag{1.1}$$

of free fermion. Through the minimal substitution

$$\partial_\mu \rightarrow D\mu = [\partial_\mu + iqA_\mu(x)] \tag{1.2}$$

(where q is the charge of particle annihilated by the field $\psi(x)$) we obtain the Lagrangian density of a fermion into electromagnetic field

$$L = \overline{\psi}(x)\left(i\gamma^\mu D_\mu - m\right)\psi(x) = L_0 - q\overline{\psi}(x)\gamma^\mu\psi(x)A_\mu \tag{1.3}$$

We require invariance of resulting theory under gauge transformation of the electromagnetic field

$$A_\mu(x) \rightarrow A^{'}{}_\mu(x) = A_\mu(x) + \partial_\mu f(x), \tag{1.4}$$

where $f(x)$ is a real differentiable function. The invariance is ensured if we couple the transformation (1.4) with the trasformation of Dirac field $\psi(x)$ and $\overline{\psi}(x)$.

$$\begin{aligned} \psi &\rightarrow \psi^{'}(x) = \psi(x)e^{-iqf(x)} \\ \overline{\psi} &\rightarrow \overline{\psi'}(x) = \overline{\psi}(x)e^{iqf(x)}. \end{aligned} \tag{1.5}$$

The coupled transformations (1.4) and (1.5) form the gauge transformation and any theory which is invariant under a gauge transformations, is a gauge theory. The Quantum Electrodynamics [9] (QED) is the simplest example.
In the a above discussion we started from the electromagnetic interaction. The gauge invariance of electromagnetic potential required the local phase transformations of Dirac field to restore the invariance of theory. We can try to reverse this argument and start from the invariance of the free - fermion lagrangian (1.1) under the (1.5) transformations of the Dirac fields $\psi(x)$ and $\overline{\psi}(x)$. Under these transformations the lagrangian density L_0 becomes:

$$L_0 \rightarrow L^{'} = L_0 + \overline{\psi}(x)\gamma^\mu\psi(x)\left(\partial^\mu f(x)\right)$$

and the second term breaks the invariance of the theory. The invariance of theory is then restored by introducing a modified derivative, D_μ, that transforms like $\psi(x)$ itself:

$$D_\mu\psi(x) \rightarrow e^{-iqf(x)}D_\mu\psi(x). \tag{1.6}$$

To form such a covariant derivative D_μ, a vector field A_μ must be introduced, with the transformation property such that the unwanted term in the 1.6 cancels. This can be accomplished by construction

$$D_\mu \equiv \partial + iqA_\mu \tag{1.7}$$

where q is an arbitrary constant and A_μ transforms as (1.4). The constructed covariant derivative indeef satisfies the (1.6). The invariance of the lagrangian (1.1) is now obtained by replacing ∂_μ by D_μ:

$$L = \overline{\psi}(x)\left(i\gamma^\mu D_\mu - m\right)\psi(x) = \overline{\psi}(x)\left(i\gamma^\mu \partial_\mu - m\right)\psi(x) \\ -q\overline{\psi}(x)\gamma^\mu\psi(x)A_\mu \equiv L_0 + L_I. \tag{1.8}$$

The term L_I that arises from the theory invariance request under $SU(1)$ transformations, couples the Dirac fields with the vector field A_μ, imposing the interaction between Dirac field and vector field A_μ.
Since the electromagnetic strenght tensor

$$F_{\mu\nu} \equiv \partial_\mu A_\nu - \partial_\nu A_\mu \tag{1.9}$$

is invariant under gauge transformations (1.4), so is the lagrangian for free gauge field

$$L_A = -\frac{1}{4}F_{\mu\nu}F^{\mu\nu}. \tag{1.10}$$

This lagrangian together with (1.8) describes the Quantum Electro-Dynamics.

We can conclude that the gauge invariance of electromagnetic field introduces the local transformations of matter field and minimal substitution, on the other hand the local phase transformations of matter fields introduces the gauge field coupled with matter ones through the replacement of the ordinary derivative $\partial_\mu\psi(x)$ with the covariant derivative $D_\mu\psi(x)$.

1.1.2 The ElectroWeak theory

Applying what we learned from the previous section, we can formulate the electroweak interactions as gauge theroy.
The physics history is rich of attempts to construct a gauge theroy for the (electro)weak interactions Starting from Schwinger that in the end of 1950's, suggested a model based on the group $O(3)$ with a triplet gauge fields (V^+, V^-, V^0). where V^0 was identified with the photon, up to Glashow (a similar model proposed by Salam and Ward in 1964) [1, 2, 3], that in 1961 noticed that in order to accommodate both weak and electromagnetic interactions we should go beyond the $SU(2)$ isospin structure, that was able to take in the account only the $V - A$ structure of weak interaction.
He suggested the gauge group $SU(2)_L \otimes U(1)_Y$, where the $U(1)_Y$ was associated to the leptonic hypercharge (Y) that is related to the weak isospin (T) and the electric charge through the analogous of the Gell-MannNishijima formula

$$Q = I_3 + \frac{Y}{2}. \tag{1.11}$$

This now theory requires four gauge bosons: a triplet massless vector fields $W_\mu^{1,2,3}$, associated to the generators of $SU(2)_L$ and a neutral vector field (B_μ) related to the generator of $U(1)_Y$. The corrisponding physical charged weak bosons, appear as a linear combination of W^1 and W^2,

$$W_\mu^\pm = \sqrt{\frac{1}{2}}\left(W_\mu^1 \pm iW_\mu^2\right), \tag{1.12}$$

while the photon and a neutral weak boson Z are both given by a mixture of W^3 and B

$$A_\mu = B_\mu \cos\theta_W + W_\mu^3 \sin\theta_W, \tag{1.13}$$

$$Z_\mu = -B_\mu \sin\theta_W + W_\mu^3 \cos\theta_W, \tag{1.14}$$

where θ_W is the *Weinberg angle*.
Following the recipe of gauge theory, he introduced the fermions-gauge bosons coupling via the covariant derivatives distinguishing between left (L) and right (R) components of fermions for $V-A$ structure of weak interactions,

$$D_\mu^L \rightarrow \partial_\mu + i\frac{g}{2}\tau^i W_\mu^i + i\frac{g^{'}}{2}YB_\mu, \tag{1.15}$$

$$D_\mu^R \rightarrow \partial_\mu + i\frac{g^{'}}{2}YB_\mu, \tag{1.16}$$

where g and $g^{'}$ are the coupling constant associated to groups $SU(2)_L$ and $U(1)_Y$. After the minimal substitution into the free-fermion lagrangian

$$\begin{aligned} L_0 \rightarrow L_{ewk} = L_0 + L_I = L_0 + \\ \overline{\psi_L}(x)i\gamma^\mu(\partial_\mu + i\frac{g}{2}\tau^i W_\mu^i + i\frac{g^{'}}{2}YB_\mu)\psi_L(x) + \\ \overline{\psi_R}(x)i\gamma^\mu(\partial_\mu + i\frac{g^{'}}{2}YB_\mu)\psi_R(x). \end{aligned} \tag{1.17}$$

We can rewrite the interaction lagrangian L_I in terms of physical vector field ($W_\mu^\pm$, A_μ and Z_μ) and weak and charge currents (J^μ and s^μ).

$$\begin{aligned} L_I = \frac{-g}{2\sqrt{2}}[J^{\dagger\mu}W_\mu + J^\mu W_\mu^\dagger] - \frac{g^{'}}{e}s^\mu[-\sin\theta_W Z_\mu + cos\theta_W A_\mu] \\ -J_3^\mu g[-\cos\theta_W Z_\mu + sin\theta_W A_\mu] - g^{'}[-\sin\theta_W Z_\mu + cos\theta_W A_\mu]. \end{aligned} \tag{1.18}$$

Identifing A_μ with the electromagnetic field that is coupled to electric charge through the usual term $-s^\mu A_\mu$, the coefficient of $J_3^\mu A_\mu$ must vanish, and that of $s^\mu A_\mu$ must be -1. This implies that

$$g\sin\theta_W = g^{'}\cos\theta_W = e. \tag{1.19}$$

In the end, we obtain the final expression for the interaction lagrangian:

$$L_I = \frac{-g}{2\sqrt{2}}[J^{\dagger\mu}W_\mu + J^\mu W_\mu^\dagger] - \tag{1.20}$$
$$s^\mu A_\mu - \frac{g}{cos\theta_W}[J_3^\mu - \sin^2\theta_W \frac{s^\mu}{e}]Z_\mu.$$

and the final version of ElectroWeak lagrangian.

1.1.3 The Higgs mechanism

Figure 1.2: *Storical comics presented at CERN, to explain the Higgs mechanism in simple way.*

The Standard Model, as described above, cannot account for massive bosons and fermions as observed in Nature. This can be seen observing that a massive fermions term:

$$m_e\overline{\psi}_e(x)\psi_e(x) \tag{1.21}$$

would mix up the left- and right-handed fermions or a massive boson term:

$$\frac{1}{2}mA_\mu A^\mu \tag{1.22}$$

would break the gauge invariance $SU(2)_L \otimes U(1)_Y$.
In order to allow massive particles, we need to break the electroweak symmetry in such a way that all succefull symmetry predictions are still preserved. Moreover, the $W^\pm$ and Z must acquire large masses keeping the photon massless. This can be achieved through the *spontaneous symmetry breaking* mechanism, in which the lagrangian density describing the dynamics of the theory is still invariant under the gauge transformations but the ground state (*vacuum*) no longer possesses the gauge symmetry. In the Standard Model, we need an external field to break the electroweak gauge symmetry: the *Higgs Field* [10]. It is a scalar field with the characteristic property that its ground state energy is non-zero. The Standard Model is defined using the simplest realization of Higgs mechanism that allows to

break $SU(2)_L \otimes U(1)_Y \rightarrow U(1)_Y$. Introducing the Higgs field, a $SU(2)_L$ doublet of complex scalar fields:

$$\phi = \begin{pmatrix} \phi^+ \\ \phi^0 \end{pmatrix} = \frac{1}{\sqrt{2}} \begin{pmatrix} \phi_1 + i\phi_2 \\ \phi_3 + i\phi_4 \end{pmatrix} \tag{1.23}$$

with lagrangian L and scalar potential $V(\phi)$ given by

$$L_{Higgs} = (D_\mu \phi)^\dagger (D^\mu \phi) - V(\phi) = (D_\mu \phi)^\dagger (D^\mu \phi) - \mu^2 \phi^\dagger \phi - \lambda (\phi^\dagger \phi)^2 \tag{1.24}$$

where D_μ is the 1.15. For $\mu^2 < 0$ e $\lambda > 0$ the potential has a circle of non-zero

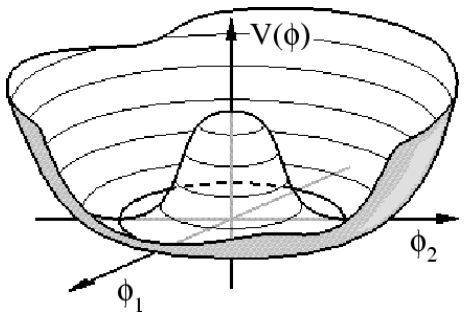

Figure 1.3: *Higgs potenzial for* $\mu^2 < 0$ *e* $\lambda > 0$.

degenerate minima (Fig. 1.3) for

$$\phi^\dagger \phi = \frac{1}{2} \left({\phi_1}^2 + {\phi_2}^2 + {\phi_3}^2 + {\phi_4}^2 \right) = \frac{\mu^2}{2\lambda} \equiv \frac{v^2}{2}. \tag{1.24}$$

So we can define the higgs doublet in this way

$$\phi = \frac{1}{\sqrt{2}} \begin{pmatrix} 0 \\ v + h(x) \end{pmatrix} \tag{1.25}$$

breaking spontaneously the simmetry.
Developing the covariant derivative we get the:

$$(D_\mu \phi)^\dagger (D^\mu \phi) \rightarrow \frac{1}{2} \partial_\mu h(x) \partial^\mu h(x) + \frac{1}{2} \left(\frac{1}{2} g v \right)^2 Z^\mu Z_\mu + \left(\frac{g v}{2 \cos \theta_W} \right)^2 W^+ W^- + ... \tag{1.25}$$

The introducing the spontaneous breaking mechanism give mass at vector bosons $W^\pm$ and Z by interaction with the Higgs field with non-zero *vacuum* value and we can found the expressions of their masses:

$$m_{W^\pm} = \frac{1}{2} g v, \tag{1.25}$$

$$m_Z = \frac{gv}{2\cos\theta_W}, \tag{1.25}$$

that depend on v, g and λ. The first two parameters can be derived from measured quantities such as the Fermi weak constant G_F, the electric charge e and $\sin^2\theta_W$. The thus obtained valus of m_W and m_Z are very close to measured values 80.398 $\pm$ 0.025 and 91.1876 $\pm$ 0.0021 GeV, respectively. The Higgs mechanism provides a remarkbly simple and successful solution to electroweak symmetry breaking problem. However the parameter λ is characteristic of ϕ field, is a free paramter of the theory, related to Higgs mass by the relation:

$$m_H = \sqrt{2\lambda}v \tag{1.25}$$

that can therefore not be predicted by the theory.
So far no experimental evidence of a Higgs particle has be found, but if it exist, from theoretical and experimental considerations, its mass must lie into the energy range accessible at the Large Hadron Collider. In fact, first of all, the Higgs potential is affected by radiative corrections, which involve the mass of bosons and fermions and dipends on the *renormalization scale* Λ. The radiative corrections could change the shape of Higgs potential, so that it might have more than an absolute minumum, rending the *vacuum* state unstable. The request of *vacuum stability* up to a certain scale Λ, imposes a lower bound on m_H .
On the other hand, due to the running of the coupling, λ increases with the energy scale. The requesting that it remains finite up to a scale Λ imposes an upper bound. If the Standard Model remains valid up to the Planck scale ($\Lambda = 10^{19}$ GeV), the Higgs mass must be in the range $130 \div 200$ GeV/c^2. While assuming the Standard Model to be valid only up to 1 TeV, the Higgs mass can be up to 700 GeV/c^2 . On the other hands direct measurements (see Fig. 1.4) at LEP exclude the region below 114.4 GeV/c^2 at 95% confidence level while in March of 2009 the experiments CDF and D0 at Tevatron excluded range in the $160 \div 170$ GeV/c^2 at same confidence level. The region is extended up to 180 GeV/c^2 at confidence level of the 90%.

1.2 Physics at Large Hadron Collider

The Higgs mechanism has received no experimental confirmation as yet, and the lower limit on the mass of the Higgs boson ($m_H > 114.4$ GeV from direct searches at LEP) has become close to the indirect upper bound derived from a fit to the electroweak data ($m_H < 167$ GeV at the 95% C.L.), which starts to raise questions about the internal consistency of the theory. In addition, the generation of fermion masses spoils the simplicity of the theory introducing new parameters. The above arguments require new and more fundamental physics. There are today several candidate scenarios for physics beyond the Standard Model, including *Supersymmetry* (SUSY) [11, 12, 13, 14], *Technicolour* [15] and

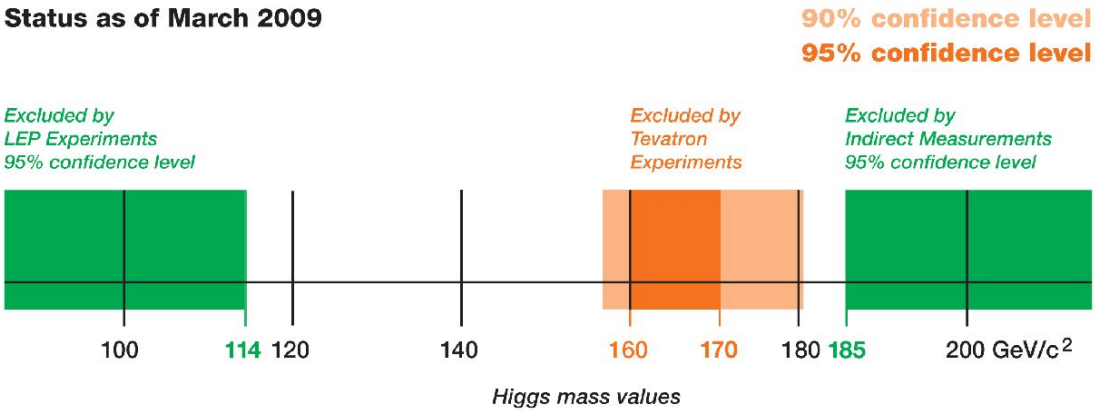

Figure 1.4: *Experimental bound of Higgs mass.*

theories with *Extra-dimensions* [16].
All of them predict new particles in the TeV mass region.

Thanks to a seven-fold increase in energy and ten-fold increase of nominal luninosity, compared to Tevatron, the Large Hadron Collider (see Ch will enter new physics territory, allowing to extend our knowledg of elementary process that rule the nature, and the origin of the universe.
Operation at a high-energy and high-luminosity will become, the LHC a factory of possible new particles with masses up to a few TeV which have reasonable couplings to Standard Model particles.

At the same time, several experimental challenges are required, on the trigger and detector performance. First of all at the LHC, the high transverse momentum (p_T) event rate will be dominated by QCD jet production, a strong process with a huge cross-section. In contrast, the most interesting physics channels are usually much rarer either because they involve the production of heavy particles, or because they arise from electroweak processes as W or Higgs production. Therefore, in contrast to leptonic machines, there is no hope for experiments at the LHC to detect this processes if they decay into jets, unless it is produced in association with other particles giving a cleaner signature, since such final states will be buried by the much larger QCD background. Decays into leptons or photons have to be used instead, so that in general only a fraction of the available cross-section is *de facto* usable.
In addition, the QCD cross-sections grows much faster with $\sqrt{s}$ than electroweak one (LHC could be considered essentially a gluon-gluon collider) then, although signal rates will be larger at the LHC than at the Tevatron, signal-to-background ratios are expected to be worse in many cases.

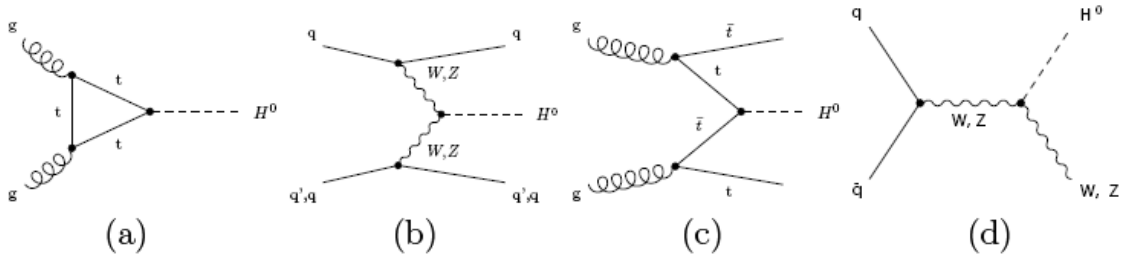

Figure 1.5: *Main Feynman diagrams contributing to the production of a Standard Model Higgs boson at the LHC: (a) gg-fusion, (b) WW and ZZ fusion, (c) associated ttH production, (d) associated WH and ZH production.*

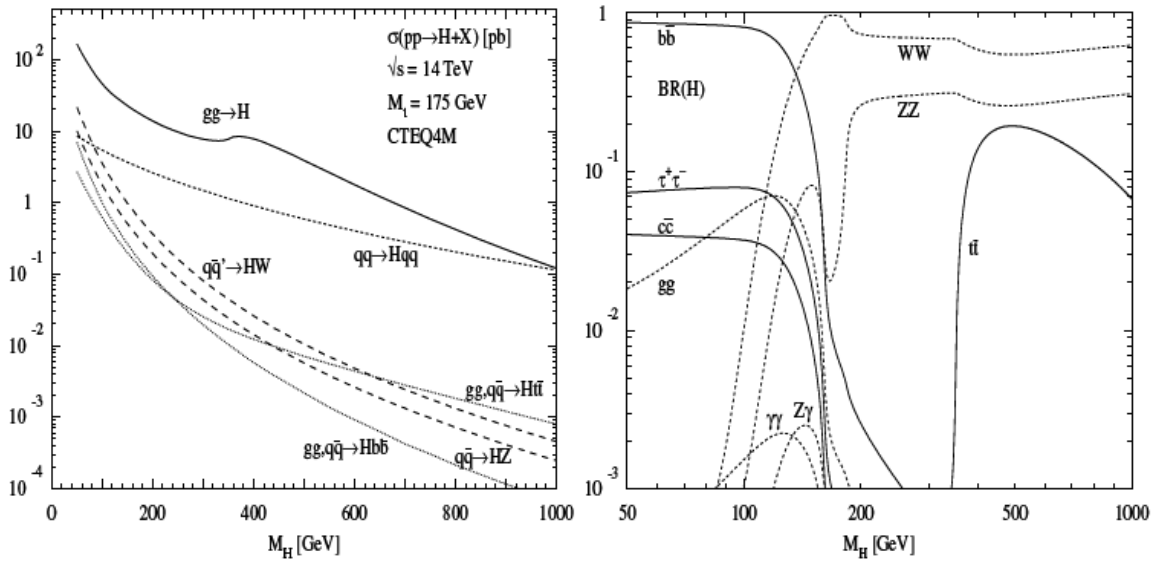

Figure 1.6: *The Higgs production cross-section as function of m_H (left); Higgs decay branching ratio as a function of m_H (right).*

1.2.1 Searches for the Standard Model Higgs boson

The production of a Standard Model Higgs, as shown in figures 1.5 and 1.6, is expected to proceed mainly from gluon-gluon fusion through a top-quark loop. Vector boson (WW, ZZ) fusion contributes (1.5(b)) about 20% of the cross-section for $m_H \sim 120$ GeV and becomes more and more important with increasing Higgs mass. This process has a clean signature, made by two jets emitted in the forward regions of the detector and very little activity in the central one. Others Higgs production processes, like $t\bar{t}$ pair (1.5(c)) or a W/Z boson (1.5(d)), has a smaller cross-section.

The Higgs decay modes and branching fraction are known, because the Standard Model predics that this particle couples to fermions and bosons with strenght proportional to their mass (1.2.1), (1.2.1) and (1.2.1).

$$g_{Hff} = \frac{m_f}{v}, \tag{1.25}$$

$$g_{HZZ} = \frac{{m_Z}^2}{v}, \tag{1.25}$$

$$g_{HWW} = \frac{2{m_W}^2}{v}. \tag{1.25}$$

Therefore, for a light Higgs boson ($m_H < 120$ GeV) the favorite decay is into $b\bar{b}$. However, the QCD jet background is so high at LHC that it will be almost impossible to observe $b\bar{b}$ decay (except associated with ttH or WH production) The most favorite channel is $H \to \gamma\gamma$ which despite the very low branching ratio ($\sim 10^{-3}$) has a very clean signature. Excellent performance of the electromagnetic calorimeters is crucial for good π^0 rejection, since a mass resolution of $\sim 1\%$ is needed to observe a narrow signal peak on top of the irreducible background.

For larger Higgs masses, the production of WW and ZZ pairs becomes possible; the branching ratio is high, but purely hadronic final states are again not accessible. $H \to 4l$ is the *golden-plated* channel for Higgs search. The channel

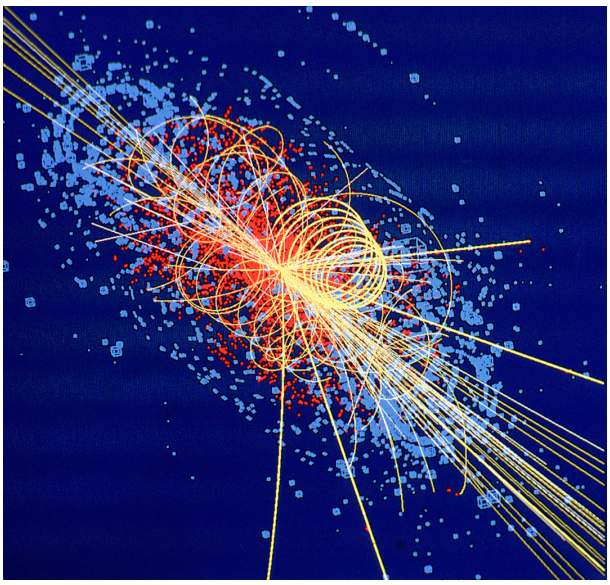

Figure 1.7: *A simulated $H \to 4l$ event seen by CMS.*

$H \to WW$ has the disadvantage that final leptonic states have at least one neutrino, however it remains a good discovery channel, especially for $m_H \approx 2m_W$

ZZ branching ratio drops to 20% as it is shown in Fig. 1.6(b). For very high Higgs masses the Higgs width becomes also very broad and the reconstruction of a mass peak becomes difficult (see fig 1.8).

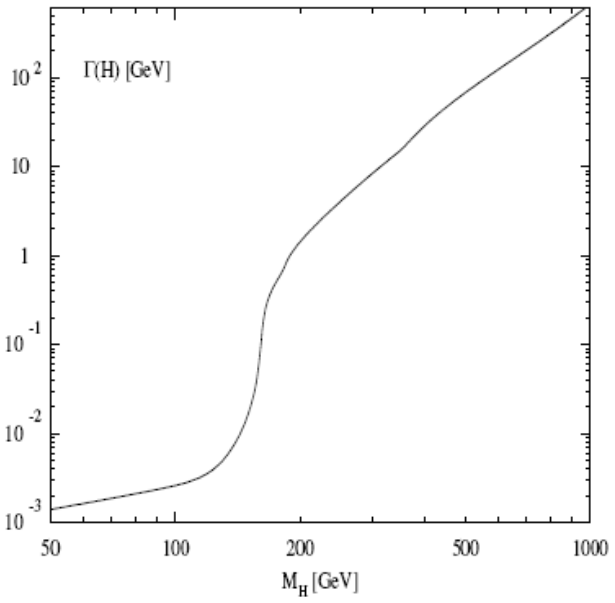

Figure 1.8: *Width of Higgs boson as function of its mass.*

With more integrated luminosity than 10 fb^{-1}, the observation of the Higgs boson will become unambiguous as the Fig. 1.9 shows.

It should also be noticed that both the multipurpose detectors, ATLAS and CMS, conceived to detect the largest possible number of decays, will provide the discovery robustness and additional hints to understand the nature of the signal. In conclusion, after the first years of operation the LHC should provide the final word about the Standard Model Higgs mechanism: if nothing is found, other mechanisms will be investigated.

1.2.2 W and Z at LHC

The LHC will be a W and Z factory: with a production rate up to 6 times higher than at Tevatron, the experiments ATLAS and CMS expect to collect, already for an integrated luminosity as low as 10 pb^{-1}, $\approx 10^4$ Z and $\approx 10^5$ W events decaying to each leptonic avour (e, μ, τ) at $\sqrt{s} = 14TeV$ as it is shown in the Fig.1.10.

Characterized by relatively large cross-sections and clean and simple experimental signatures coupled with precise theoretical predictions, they will be the Standard Candle for many LHC early measurements. They will be essential in the

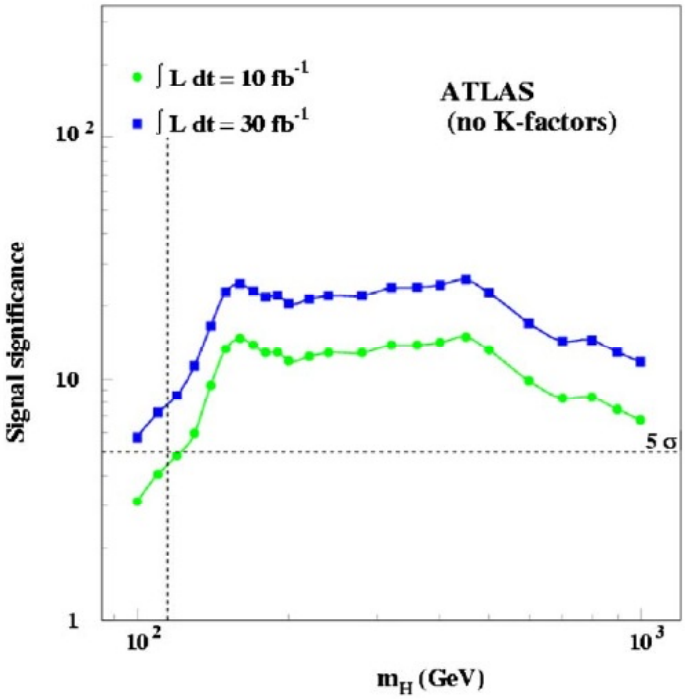

Figure 1.9: *The expected signal significance for the discovery of a SM Higgs boson as a function of its mass, for integrated luminosities of 10 fb^{-1} (dots) and fb^{-1} (squares). The vertical line shows the mass lower limit from LEP. The horizontal line indicates the minimum significance (5σ) needed for discovery.*

early LHC running for the calibration/alignment of the detectors and to establish their performance. These $pp \rightarrow W+X$ and $pp \rightarrow Z+X$ events also constitute the main source of background for Higgs searches in the golden plated channel and, in addition, in many searches beyond the Standard Model to be carried out at the LHC, and therefore a precise understanding of these processes is critical before any discovery can be made. Their study represents a first step in the detailed understanding of reference physics processes at the LHC: transverse momentum spectra, associated jet activity, beyond-leading-order effects, and Parton Density Function (PDF's). For example, studies of the charge asymmetry in $W \rightarrow \mu\nu$ (Fig. 1.11) can provide constraints on PDF's.

The signature for Z decaying to leptons is one of the cleanest to be found in a detector at a hadron collider: two isolated, high p_T leptons of opposite sign, with a resonant mass around the Z peak (Figure 1.12). The background expected is very small, less than 0.3% ($W \rightarrow l\nu$, $Z \rightarrow \tau\tau$, $t\bar{t}$, QCD), and can be estimated directly from data, either from a fit to the whole mass range (as we will can see in

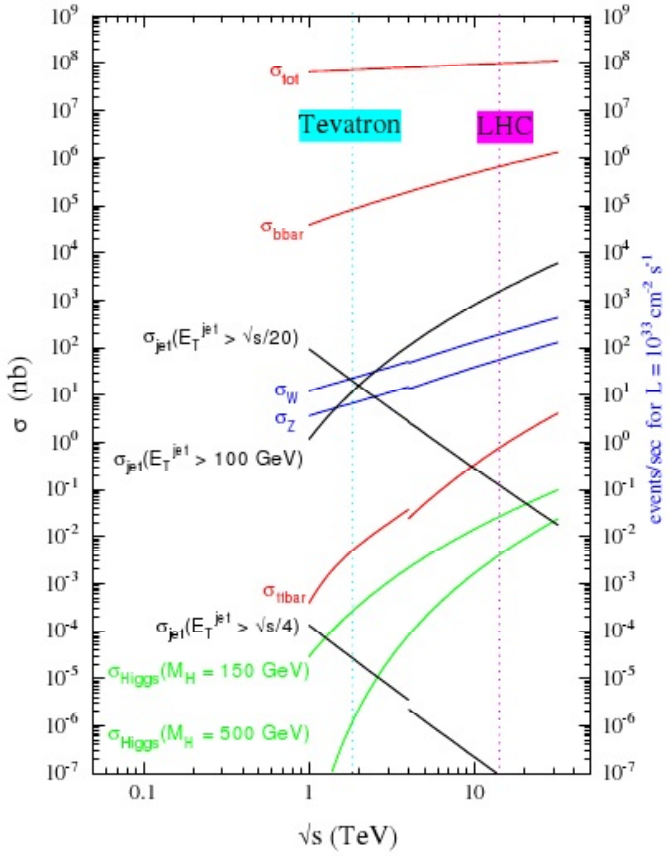

Figure 1.10: *Production cross-sections for various processes at hadron colliders (pp and $p\overline{p}$), as a function of the machine centre-of-mass energy. The discontinuities in some of the curves are due to the transition from pp to $p\overline{p}$ collisions.*

this work), from the sidebands, or from charge-correlation. The Z leptonic decay constitutes therefore an ideal sample for computing lepton efficiencies through tag and probe techniques [17, 18], based on the requirement of strict criteria on one of the two leptons present in the event to obtain a clean control sample and computing the efficiency on the remaining lepton.

$W^{\pm}$ events (1.13) are characterized by a single isolated, high p_T lepton, coupled with an missing energy caused by the presence of a neutrino. This causes an higher background contamination than in the Z case, so several data-driven techniques for background estimation (in particular the QCD) are developed. The main are the Template Method [17] and the Matrix $ABCD$ method [17]. The first one is based on the similarities between Z and W kinematics, it models the missing energy distribution of signal and QCD background from $Z \rightarrow l^{+}l^{-}$

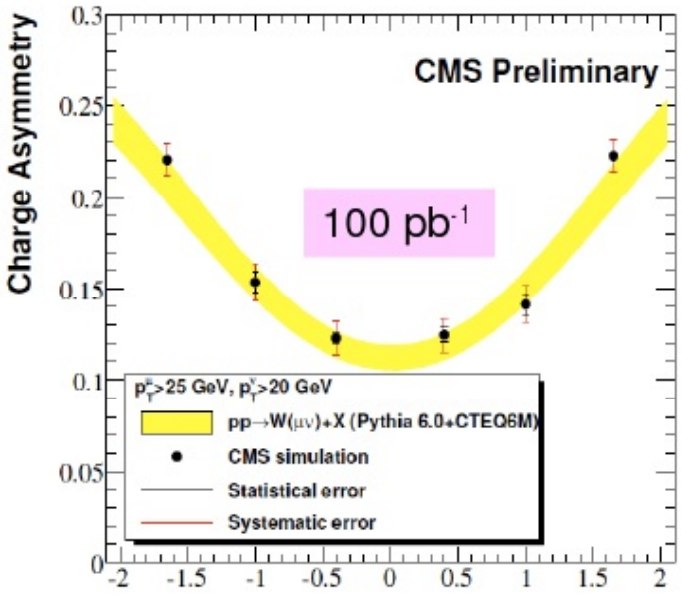

Figure 1.11: *The maesured charge asymmetry result at* $100pb^{-1}$.

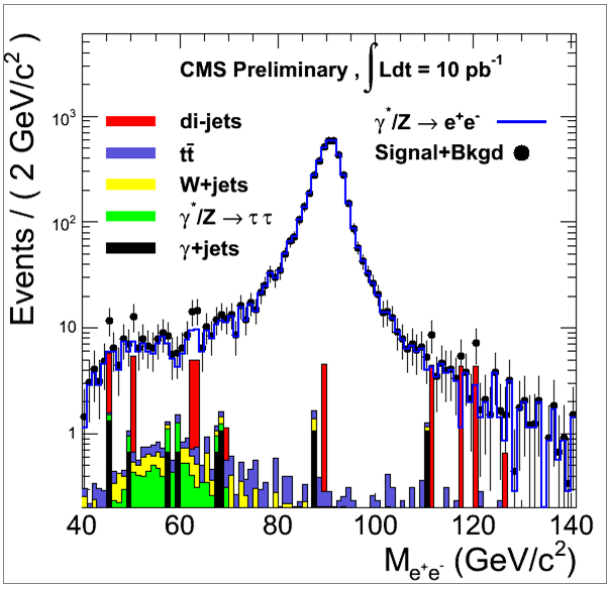

Figure 1.12: *Invariant mass distribution of* $Z \rightarrow e^+e^-$

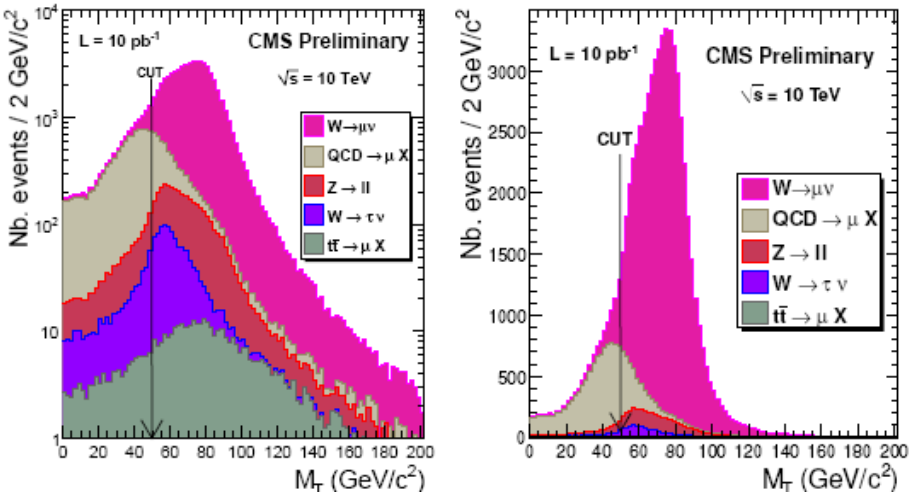

Figure 1.13: *Invariant transverse mass distribution of* $W \rightarrow \mu\nu$

to extrapolate by a fit on data the number of signal events. The second, the $ABCD$ method, is able to extropolate the number of QCD events by counting it in suitable sidebands obtained from a two dimensional scatter-plot of the data sample as a function of two uncorrelated variables.

1.2.3 Top quark Physics

The top quark plays a central role in the physics programs of present and future high energy physics collider experiments. It is, indeed, a privileged tool for precise studies of the Standard Model being far the heaviest fundamental particle and the only quark decaying before hadronization takes place. As a consequence, a precise measurement of its mass constitutes a crucial test of the electroweak sector and puts indirect constraints onto the Higgs boson mass via radiative corrections, while its very short lifetime ($\sim 10^{-25}s \ll$ hadronization time) offers a unique window on bare quarks. Top quark events are also a major source of background for many search channels, and precise understanding of top signal is crucial to claim new physics discoveries.
Beause of limited statistics, thirteen years after its discovery at the Tevatron, top production and decay mechanisms is still poorly known. LHC will be a top factory [19] [20], with cross-sections for producing $t\bar{t}$ pairs and single tops roughly 100 times larger than at Tevatron: 8 millions of $t\bar{t}$ and 3 millions of single tops will be produced per year (at $\sqrt{s} = 14TeV$ and $L = 10^{33}s^{-1}cm^{-2}$), corresponding to 10 fb^{-1}.
Moreover, its high mass, suggests that the top quark could be bound to new physics process. Examples include the possible existence of charged Higgs bosons,

or possibly large flavor changing neutral currents in top decays. The top decay to a light charged Higgs boson, $t \to H^+ b$, can be searched for through an excess of $t\bar{t}$ events with τ-jets or a deficit of dilepton events. In the Standard Model, flavor changing neutral currents ($FCNC$) top decays are highly suppressed ($BR < 10^{-13} \div 10^{-10}$) while in several extensions of the Standard Model can lead to very significant enhancements of them up to 10^{-3} which could be detected directly in $t\bar{t}$ events. The current limits on the branching ratios of FCNC processes can be improved by a factor 10^2 to 10^3 already with 10 fb^{-1}, such a sensitivity allowing to probe models beyond the Standard Model.

1.2.4 b Physics

CP-violation is one of the outstanding questions in particle physics. It was first discovered and established in the kaon system, for which the most precise measurement today comes from the CERN NA48 experiment [21, 22]: $Re(e^{'}/e) = (14.7 \pm 2.2) \times 10^{-4}$. The LEP experiments and CDF have performed many studies of the B-system, but only in the year 2001, with the advent of the SLAC and KEK B-factories, the first significant observation of CP-violation in B-decays has been obtained. The BaBar [23, 24] and Belle [25] experiments, operating at the PEP II/SLAC [26] and KEKB/KEK e^+e^- machines, respectively, have unambiguously established the non-vanishing value of $\sin 2\beta$, one of the angles of the CKM unitarity triangle (present world average: $\sin 2\beta = 0.736 \pm 0.049$). The most intriguing issue in this field, relevant to both particle physics and cosmology, is that the above experimental measurements confirm, within their uncertainties, the CP-violation predicted by the Standard Model, which is a consequence of the quark mass generation and of a phase in the quark-mixing CKM matrix. The problem is that this amount of CP-violation is insufficient to explain baryogenesis and the ensuing matter-antimatter asymmetry in the universe, which calls for additional contributions from new physics. The task of present and future B-physics experiments is therefore to clarify this puzzle, by performing precise, comprehensive, and redundant studies of CP-violating effects in the B-system, which should test the internal coherence of the Standard Model (and disclose possible inconsistencies), shed some light on the origin of CP-violation, and probe the existence of new physics.

In the field of b-physics, LHC will benefit from a very large $b\bar{b}$ production cross section. The main interest is the study of the neutral B meson, and in particular of CP violation in the $B_d^0 - \overline{B_d^0}$ and $B_s^0 - \overline{B_s^0}$ systems. b-quark physics program will be important, especially during the first phase of LHC operation (first few years). In fact once the machine achieves the design luminosity, b-quark physics will become exceedingly difficult due to the large hadronic background and pile-up. For these reasons a dedicated experiment, LHCb, has been built to develop fully this fundamental scientific program.

1.2.5 Searches for Supersymmetry and beyond

Supersymmetry (SUSY) is a theory establishing a symmetry relating fermions and bosons, or better matter fields and force fields. It is one of the best motivated scenario today for physics beyond the Standard Model. It does not contradict the precise electroweak data; it predicts a light Higgs boson, as favoured by electroweak data, it allows unification of the gauge couplings at the Grand Unification scale and it provides a candidate particle for the universe cold dark matter. In spite of these numerous motivations, we have no experimental evidence for Supersymmetry. Direct searches for SUSY particles,so colled *sparticles*, at LEP and Tevatron have been unsuccessful.

At the LHC energy, the dominant SUSY process is expected to be the production of pairs of squarks or gluinos, because these are strongly-interacting particles with QCD-type cross-sections. For instance, a sample of about 10^4 $\widetilde{q}\,\widetilde{q}$, $\widetilde{g}\,\widetilde{g}$ and $\widetilde{q}\,\widetilde{g}$ events should be produced after only 1 year of data taking at $L = 10^{33} cm^{-2} s^{-1}$ at 14 TeV if squarks and gluinos have masses of $\sim 1 TeV/c^2$. Because these sparticles have mass at least $200 - 300 GeV/c^2$, given the present Tevatron limits, they are expected to decay through long chains with several intermediate steps, and hence should give rise to very crowded final states containing in general several jets, leptons and missing transverse energy. Such spectacular signatures can be easily separated from Standard Model processes, for instance by selecting events with many high-p_T jets and large missing transverse energy. As a consequence, SUSY discovery at Large Hadron Collider could be relatively fast and easy.

1.2.6 Studies of quark-gluon plasma

The LHC will also be able to collide beams of nuclei, thereby providing ultra-relativistic heavy-ion interactions at an energy of 5.5 TeV (30 times higher than that that of RHIC at BNL [27], todays most powerful ion collider) per nucleon, i.e. a total centre-of-mass energy of more than 1000 TeV in the case of lead beams[19]. These collisions will allow the study of strongly interacting matter in unprecedented and extreme conditions of energy density and temperature. In these conditions, a phase transition from ordinary hadronic matter to a plasma of deconfined quarks and gluons is expected to happen. Because the opposite transition (i.e. from plasma to hadronic matter) is believed to have taken place about 10 μs after the Big Bang, these studies should help understand the evolution of the early universe. In addition, they should address the fundamental questions of quark confinement and approximate chiral-symmetry restoration. Heavy ions collisions will be studied with a dedicated detector, Alice, but also with ATLAS and CMS.

Chapter 2

The Large Hadron Collider and the Compact Muon Solenoid

The Large Hadron Collider (LHC) [7] is proton-proton (ion-ion) collider built in the already existing LEP tunnel at CERN of Geneva.
It will yield head-on collisions of two proton beams of 7 TeV each, with a design luminosity of $L = 10^{34} cm^{-2} s^{-1}$. In addition, in some dedicated run, it will collide ion beams at energy of 2.76 TeV/nucleon, yielding a total centre- of-mass energy of 1.15 PeV and a nominal luminosity of $L = 10^{27} cm^{-2} s^{-1}$. Collisions between ion beams will be provided principally at Interaction Point 2 (Fig2.3) for the specialised ALICE detector. The total proton-proton cross-section is more than 110 mb and the expected accumulation of data, expressed in terms of the integrated luminosity L, should reach $O(100) fb^{-1}$ per year at maximum machine luminosity. These data together with the data of ion-ion collisions, will allow the accomplishment of the huge scientific program decribed in the previous chapter. Four experiments, namely ATLAS, ALICE, CMS and LHCb, built on LHC four interaction points, will carry out this fascinating scientific program. This charapter will give a description of LHC and CMS.

2.1 The Large Hadron Collider

The Large Hadron Collider (Fig. 2.1) is a two-ring-superconducting-hadron accelerator and collider installed in the existing 26.7 km tunnel that was constructed between 1984 and 1989 for the CERN LEP machine. The LEP [28, 29] tunnel has eight straight sections and eight arcs and lies between 45 m and 170 m below the surface on a plane inclined at 1.4% sloping towards the Leman lake. There are two transfer tunnels, each approximately 2.5 km in length, linking the LHC to the CERN accelerator complex that acts as injector. Full use has been made of the existing structures, even if modifications and additions were also needed. In fact, the underground and surface structures at Points 1 and 5 for ATLAS [30]

and CMS [31], respectively, are new, while those for ALICE [32] and LHCb [33], at Points 2 and 8, respectively, were originally built for LEP.

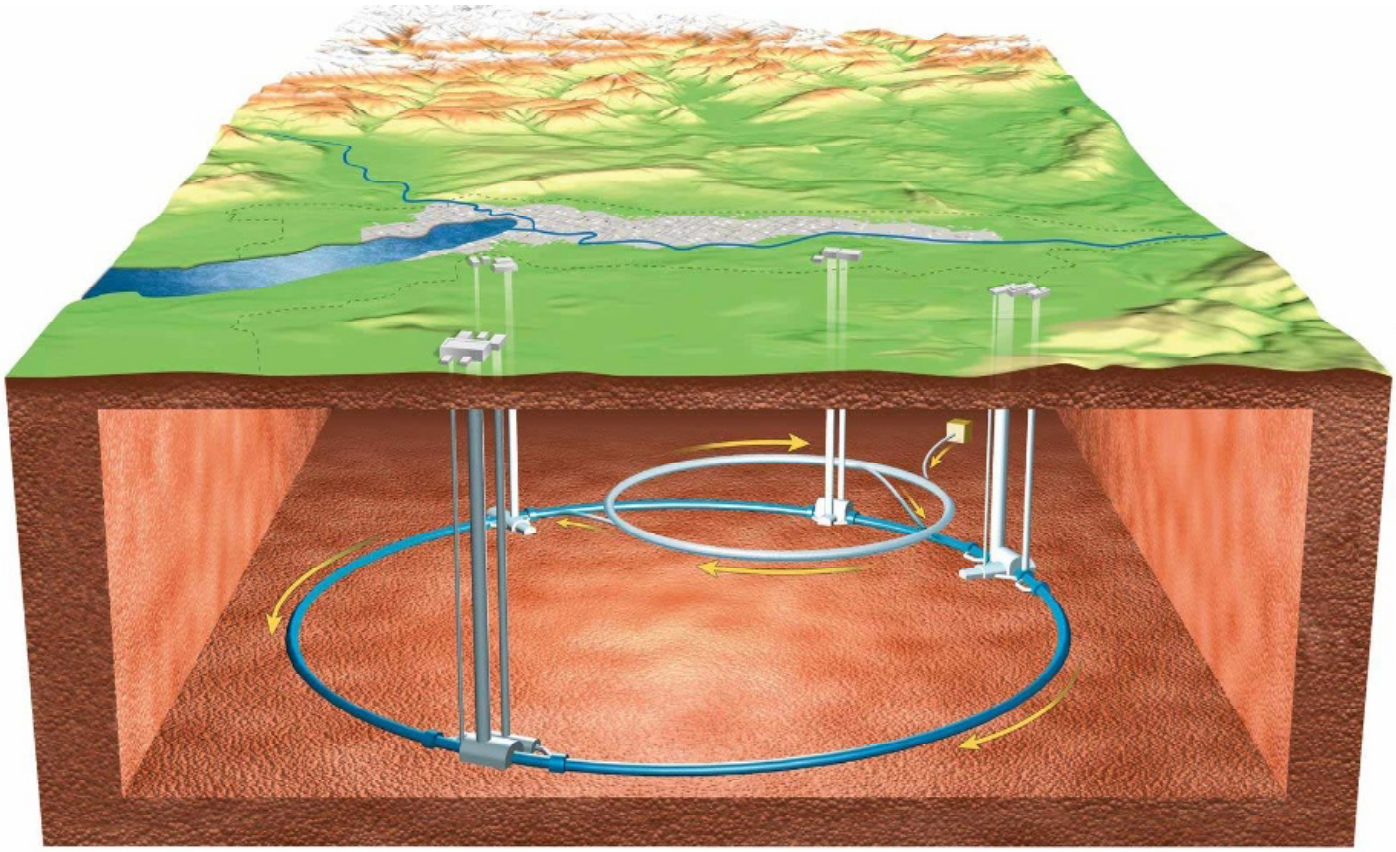

Figure 2.1: *Schematic view of underground where LHC is built.*

2.1.1 Acceleration chain

The LHC relies on a chain of several subsystems from the source to the final acceleration step LINAC2 Proton SynchrotronBooster (PSB) Proton Synchrotron (PS) Super Proton Synchrotron (SPS), as shown in Fig. 2.2.
These accelerator systems are inherited from LEP. Both PS and SPS were old machine and not optimised to be LHC injector, they were upgraded to meet the very stringent needs of the LHC: many high intensity proton bunches with small transverse and well defined longitudinal emittances. The protons originate in a 92 keV duoplasmatron source, fed with H_2 gas, yielding a 300 mA beam current. The protons from this source are collected as an input to LINAC2, which increases their energy up to 50 MeV. This linac supplies the PSB with protons for an increase in energy up to 1.4 GeV. All protons are then accelerated by the

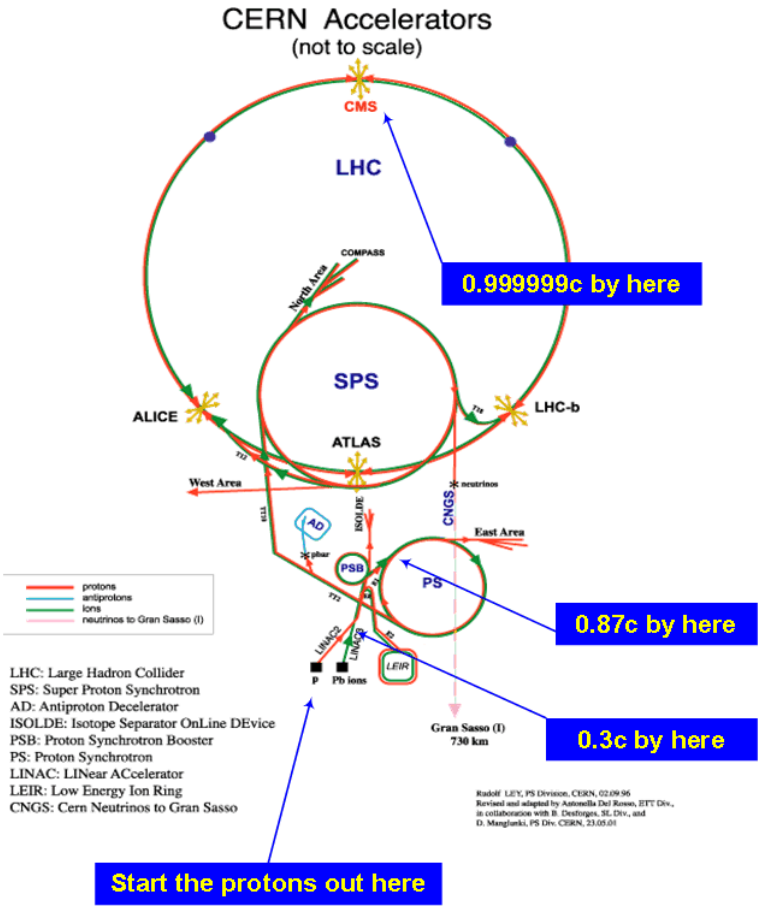

Figure 2.2: *The LHC injector complex.*

PS, up to 25 GeV and subsequently by the SPS, up to 450 GeV. The PS also builds up the proton bunches, with a 24.95 ns separation and less than 4 ns time extension. Finally, the SPS injects both beams into the LHC pipes.

The final step of beams acceleration, takes place in LHC. LHC consists of two beams, counter-circulating in separate vacuum chambers which are horizontally spaced by 194 mm. Only at about 100 m before the impact point (IP), the beam pipes joint into a single piece. Thanks to 8 resonant cavities, these two pulsed beams are accelerated up to 7 TeV. The electrical field of these radio frequency (RF) cavities oscillates at 400.8 MHz to achieve a 0.5 MeV/turn energy kick. At top energy, the field strength reaches about 5.5 MV/m. The beams are steered by 1232 cryogenic dipole magnets with a field of $B = 8.33T$ that allows a bending of $0.6 \sim$ mm per m. These dipoles are immersed in a pressurised bath of superfluid helium at about 0.13 MPa (1.3 bar) at 1.9 K to maintain a superconducting state, storing an energy of about 600 MJ. The choice of superfluid, instead of supercrit-

ical Helium like at Tevatron, HERA and RICH, allows larger temperature range, before a quenching.
Space limitations in the tunnel and the need to keep costs down, have led to the adoption of the two-in-one, or twin-bore, design for almost all of the LHC superconducting magnets.
This design accommodates the windings for the two beam channels in a common cold mass and cryostat, with magnetic flux circulating in the opposite sense through the two channels. This makes the magnet structure complicated, especially for the dipoles, for which the separation of the two beam channels is small enough that they are coupled both magnetically and mechanically.

Both beams are sampled in bunches of protons. Depending on the luminosity goal, the number of bunches can vary, but this number should always comply with the LHC 40.08 MHz clock. The clock rhythm creates 3564 slots for bunches, repeated every 24.95 ns. Not all slots are used, leaving some collision - free latencies for experiment activities like online calibration, subdetector synchronisation or electronics front-end reset.

A high luminosity bunch train thus corresponds to 2808 bunches, in either beam, with 25 ns separation and 1.15×10^{11} proton per bunch.

2.1.2 Lattice layout

The two LHC symmetrical rings are divided into eight octants and arcs and eight straight sections approximately 528 m (Fig. 2.3). The two high luminosity experimental insertions are located at diametrically opposite straight sections: the ATLAS experiment is located at Point 1 and the CMS experiment at Point 5.

The other two large experiments, ALICE and LHCb, are located at Point 2 and at Point 8, respectively, where the machine reaches a lower luminosity of $L = 5 \times 10^{32}\ cm^{-2}\ s^{-1}$. The remaining four straight sections do not have beam crossings. The two beams are injected into the LHC in two different octants, octant 2 and octant 8 respectively for clockwise and anticlockwise beam.
The octants 3 and 7, instead, contain two collimation systems for the beam cleaning.
The insertion at Point 4 contains two RF systems: one independent system for each LHC beam.
The straight section at Point 6 contains the beam dump insertion, where the two beams are vertically extracted from the machine using a combination of horizontally deflecting fast-pulsed and vertically-deflecting magnets.

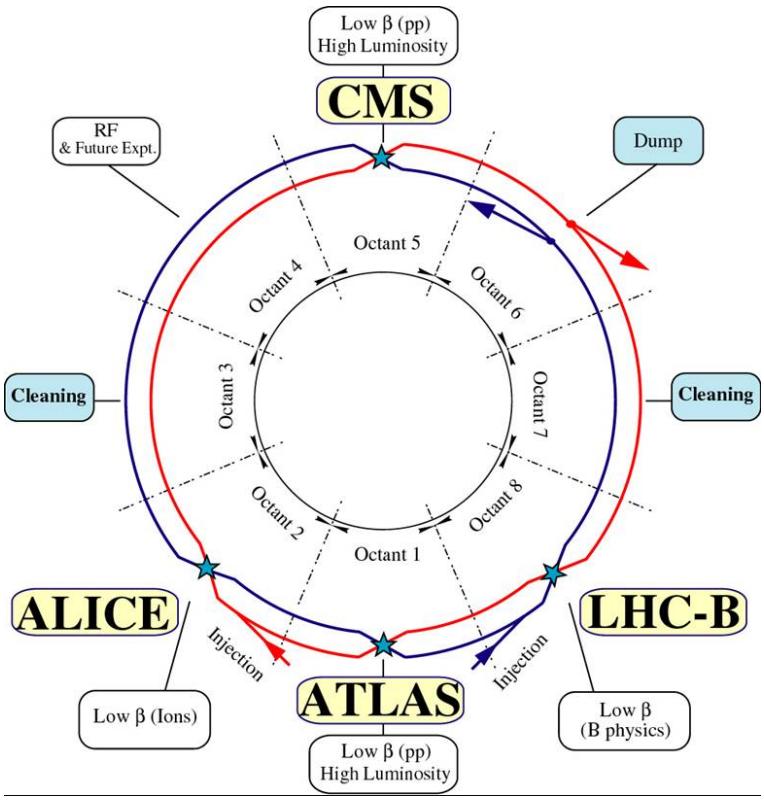

Figure 2.3: *Lattice layout of LHC.*

2.1.3 Luminosity evolution

The number of events per second generated in the LHC collisions is given by:

$$N = L\sigma \tag{2.0}$$

where σ is the cross section for the collision process under study and L the machine luminosity. The machine luminosity depends only on the beam parameters and can be written, for a Gaussian beam distribution, as:

$$L = \frac{N_b^2 n_b f_{rev} \gamma_r}{4\pi\varepsilon_n \beta^*} F, \tag{2.0}$$

where N_b is the number of particles per bunch, n_b the number of bunches per beam, f_{rev} the revolution frequency, γ_r the relativistic gamma factor, ε_n the normalized transverse beam emittance, β^* the beta function at the collision point, and F the geometric luminosity reduction factor due to the crossing angle at the interaction point (IP). The knowledge of all these parameters is expected to be known with a precision of 5%, which is assumed to be achieved after $\sim 1 fb^{-1}$ of

collected data. Before reaching this integrated luminosity, the expected precision on the luminosity measurement is approximately 10 %[].

The LHC luminosity is not constant over physics a run, but decays due to the degradation of intensities and emittances of circulating beams. The main cause of the luminosity decay during nominal LHC operation is the beam loss from collisions. The initial decay time of the bunch intensity, due to this effect, is:

$$\tau_{nuclear} = \frac{N_{tot,0}}{L\sigma_{tot}k} \tag{2.0}$$

where $N_{tot,0}$ is the initial beam intensity, L the initial luminosity, σ_{tot} the total cross section ($\sigma_{tot} = 11omb$ at 14TeV) and k the number of impact points (IPs). Assuming, for example, an initial peak luminosity of $L = 10^{34}cm^{-2}s^{-1}$ and two high luminosity experiments, the above expression yields an initial decay time of

$$\tau_{nuclear} = 44.85h. \tag{2.0}$$

Other effects play a role in the luminosity decrease and are characterised by a corresponding lifetime, like the intrabeam scattering (IBS) and the interaction with residual gas:

$$\tau_{IBS} \sim 80h, \tag{2.0}$$

$$\tau_{resgas} \sim 100h. \tag{2.0}$$

In summary, the net expected luminosity lifetime in a run (at maximum luminosity) is:

$$\frac{1}{\tau_L} = \frac{1}{\tau_{nuclear}} + \frac{1}{\tau_{IBS}} + \frac{1}{\tau_{resgas}}, \tag{2.0}$$

$$\tau_L \sim 22h. \tag{2.0}$$

2.1.4 Integrated Luminosity

The time needed to make the LHC operative, the required *turnaround time* (T_{turn}) is about 70 minutes. Indeed the beam filling and complex magnet system rumping up are thorny and meticulous operations. In detail, LHC filling riquires 12 cicles of the SPS that in turn needs 4 cycles of the PS synchrotron, for a total time of about 4 minutes. This time has to be added to the time for the injection set up. An additional 4 SPS cycles for 3 pilot bunches are required. The LHC operators spend at least two minutes to evaluate the measurements of each pilot bunch shot and to readjust the machine settings, leading the beam filling time up to 16 minutes.

In addition, the minimum time required for ramping the beam energy in the LHC from 450 GeV to 7 TeV is approximately 20 minutes.
This quantities have to be considered theoretical, indeed the experience done at others hadronic machines like HERA, for example, suggest a T_{turn} 6 times longer, leading the LHC operative time to 7 hours.
Let's define the T_{run}, the total length of the luminosity run, the integrated luminosity over one run yields as:

$$L_{int} = L_0 \tau_L (1 - e^{\frac{T_{run}}{\tau_L}}). \tag{2.0}$$

Therefore, assuming that a luminosity lifetime of 20 hours, and an average turnaround time (beetwen of 7 hours and 1.15 hours), the optimum run time is 12 hours. If the machine can be operated for 200 days per year, the total integrated luminosity per year will be in the range of $80 fb^{-1}$ to 120 fb^{-1} at peak luminosity.

2.1.5 Detectors at LHC insertions

In the four interaction points of the LHC four big experiments are built, to carry out completely the bold scientific program and to ensure the redundance of results. Two general purpose experiments, ATLAS (A Toroidal LHC Apparatus, Fig. 2.4) and CMS (Compact Muon Solenoid, Fig. 2.5) and two middle-size specialised experiments, ALICE (A Large Ion Collider Experiment, Fig. 2.6) and LHCb (LHC beauty experiment, Fig. 2.7).

The physics programmes of CMS and ATLAS are very broad, ranging from precision electroweak measurements to the potential discovery of a rich zoology of new particles predicted by theories of physics beyond the Standard Model. With two different detector designs and different approaches to data analysis the CMS and ATLAS collaborations will be able to cross check each others results and to ensure the redundance of their measurements.
LHCb will study CP violation through b-quark physics and make precision measurements of rare decays.
ALICE has been designed to study the physics of heavy ion collisions in specialised LHC runs with beams of lead and gold nuclei.
Next section will give a general overview of the CMS detector.

2.2 The Compact Muon Solenoid

The Compact Muon Solenoid is a high granularity detector built around and inside a superconducting solenoid that provides a strong magnetic field of 4 T. Inside it, the inner tracking comprises a Pixel detector (3 barrel layers of and 2 end cap disks on each side) surrounded by the Silicon Strip detector (10 barrel layers, 9 disks on each side). Its high granularity (70 millions pixels, 10 millions

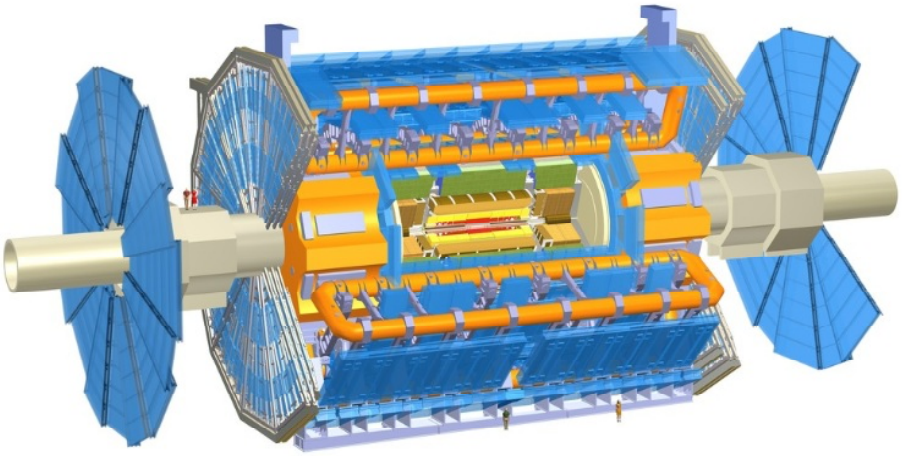

Figure 2.4: *Schematic view of Atlas.*

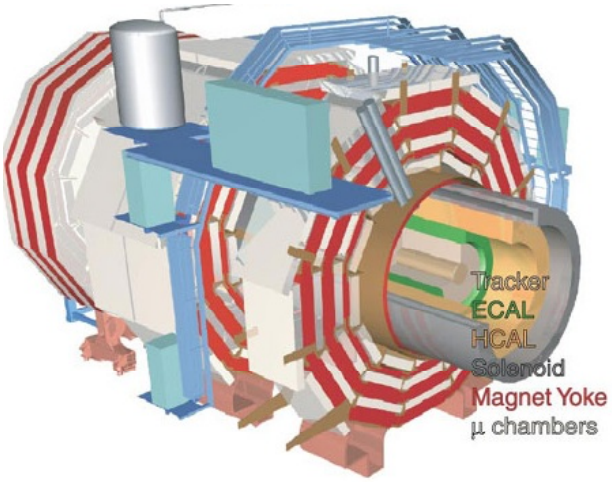

Figure 2.5: *Schematic view of CMS.*

strips) and precision ensures good track reconstruction efficiency. It is surrounded by Electromagnetic calorimeter ($ECAL$) made of 76000 lead tungstate crystals grouped in 36 barrel and 4 endcap supermodules. The brass-scintillator sampling hadron calorimeter ($HCAL$) completes the in-coil detectors.
To ensure hermeticity the in-coil calorimetric system is extended, away from the central detector, by the hadron outer detector (HO) and a quartz fiber very forward calorimeter (HF) to cover $|\eta| < 5$.

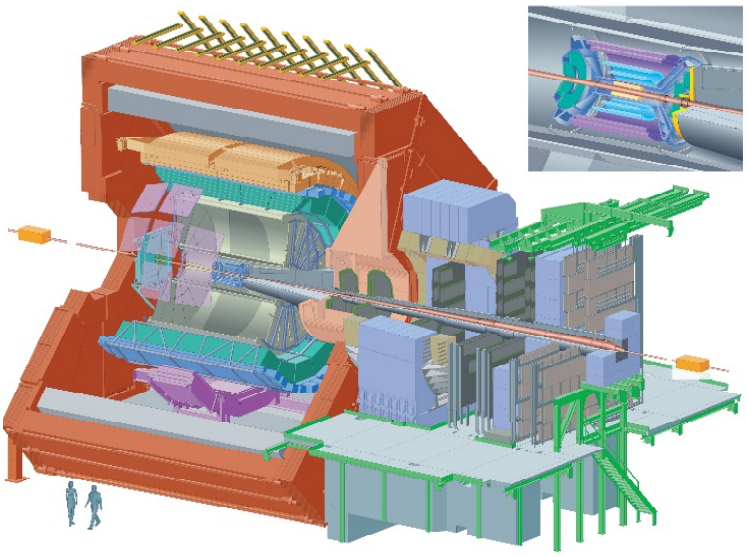

Figure 2.6: *Schematic view of Alice.*

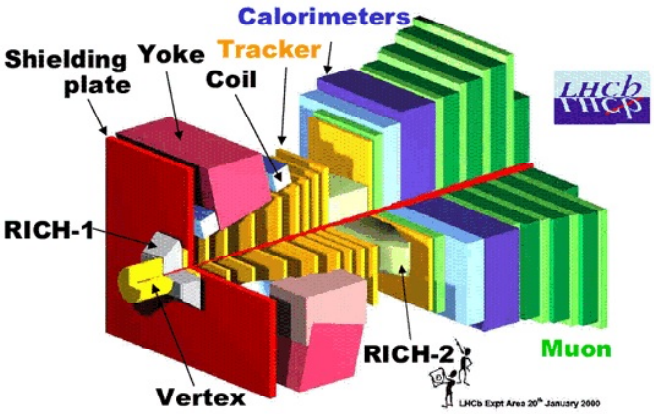

Figure 2.7: *Schematic view of LHCb.*

Outside the solenoid a muon system is built in the magnet steel return yoke. It's formed by 4 stations of muon chambers: Drift Tube (DT) in the barrel region, Cathode Strip Chambers (CSC) in the endcap, Resistive Plate Chambers in both parts (RPC), providing muon detection redundancy.
Only two trigger levels are employed in CMS. The Level-1 Trigger ($L1$) is im-

plemented using custom hardware processors and is designed to reduce the event rate to 100 kHz during LHC operation using information from the calorimeters and the muon detectors. It is operates nearly deadtime-free and synchronously with the LHC bunch crossing frequency of 40 MHz. The High Level Trigger (HLT) is implemented across a large cluster of commodity computers referred to as the event filter farm, and provides further rate reduction to $O(100)$ Hz using filtering software applied to data from all detectors at full granularity.
The overall dimension of CMS are a length of 21.6 m, a diameter of 14.6 m and a total weight of 12500 tons.
In the CMS collaboration is adopted the following system of coordinates. The x-axis points radially inward towards the centre of the LHC and the y-axis points upwards away from the centre of the Earth. The azimuthal angle ϕ is measured in the $x - y$ plane and the polar angle θ is measured from the z-axis which is orthogonal to the $x - y$ plane. beam axis. Another useful observable is the rapidity:

$$y = \frac{1}{2} \ln \frac{E + p_z}{E - p_z} = \tanh^{-1} \frac{p_z}{E} \tag{2.0}$$

where E is the particles energy, p_z the projection of particles momentum along the beam direction. Under a boost along z with speed β, y undergoes the following transformation: $y \rightarrow y \tanh^{-1} \beta$, hence rapidity differences are invariant, thus the shape of the rapidity distribution dN/dy is invariant. In the ultrarelativistic approximation the rapidity y is the same as the pseudorapidity η dened as:

$$\eta = \ln \tan(\theta/2). \tag{2.0}$$

2.2.1 Inner Tracker

The expected LHC physics program requires a robust, efficient and precise reconstruction of the trajectories of charged particles with transverse momentum above 1 GeV. The CMS tracking detector [31, 34, 35] (Fig. 2.8) has been designed to measure the momentum of charged particles over the fiducial range $|\eta| < 2.5$. In addition it allows accurate measurements of secondary vertices and impact parameters, fundamental for the identification of heavy flavours decays. Together with the electromagnetic calorimeter and the muon system the tracker has to identify electrons and muons, respectively. Tau leptons are a signature in several discovery channels and need to be reconstructed in one-prong and three-prong decay topologies.
At LHC energy and design luminosity, each bunch crossing will create on average about 1000 particles hitting the tracker. This will lead to a hit rate density of 1 MHz/mm^2 at a radius of 4 cm, 60 kHz/mm^2 at a radius of 22 cm and 3 kHz/mm^2 at a radius of 115 cm. To keep the occupancy at or below 1%, three different types of subdetectors are used: pixel detectors up to a radius below 10 cm, silicon micro-strip detectors in intermediate radius (10cm$< r <$55 cm) and

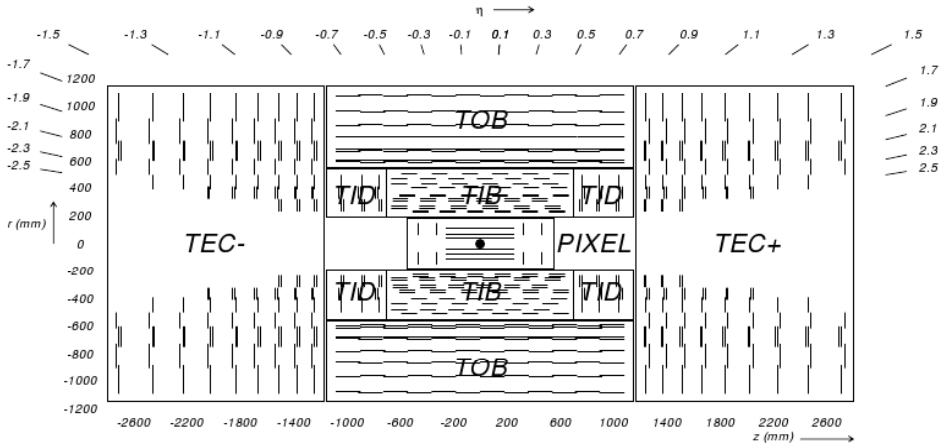

Figure 2.8: *Schematic cross section through the CMS tracker system. Each line represents a detector module. Double lines indicate back-to-back modules which deliver stereo hits.*

in the outer region but with increased strip pitch. The CMS tracker is composed of 4.4 millions n-type silicon pixel and 15400 strip detector modules divided in two subdetectors Pixel and Silicon tracker. With about 200 m^2 of active silicon area, it is the largest silicon tracker ever built. CMS is the first experiment

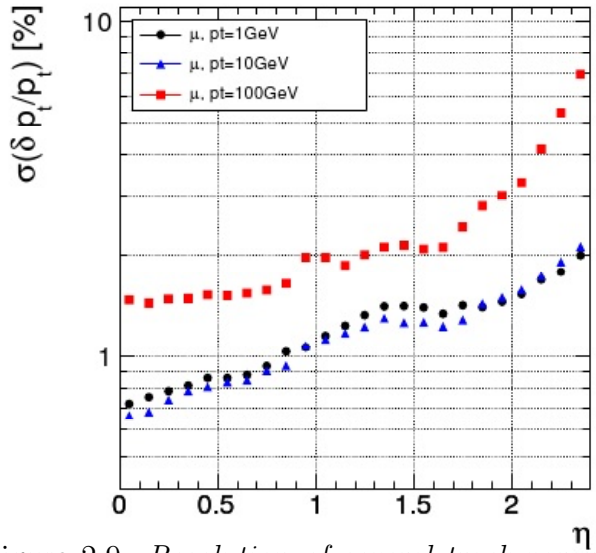

Figure 2.9: *Resolution of several track parameters for single muons with transverse momenta of 1, 10 and 100 GeV: transverse momentum.*

using silicon detectors in the outer tracker region.

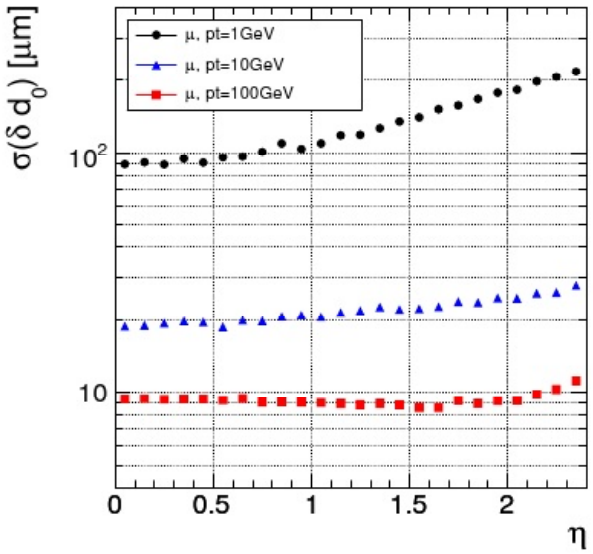

Figure 2.10: *Resolution of several track parameters for single muons with transverse momenta of 1, 10 and 100 GeV: transverse impact parameter.*

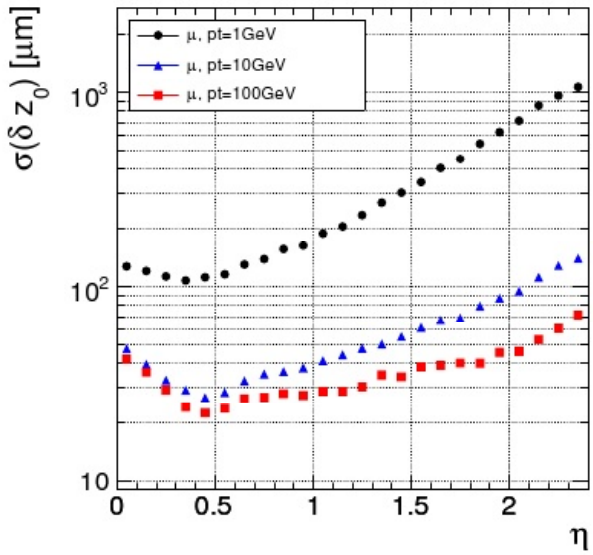

Figure 2.11: *Resolution of several track parameters for single muons with transverse momenta of 1, 10 and 100 GeV:longitudinal impact parameter.*

Figures 2.9, 2.10, and 2.11 show the expected resolution of transverse momentum, transverse impact parameter and longitudinal impact parameter, as a function of the pseudorapidity, for single muons of transverse momenta of 1, 10 and 100 GeV/c. For high momentum tracks, 100 GeV/c, the transverse momentum res-

olution is around 1÷2% up to $|\eta| \sim 1.6$, beyond which it degrades due to the reduced lever arm. At low transverse momentum the multiple scattering in the tracker material dominates while at higher transverse momentum, 100 GeV/c, multiple scattering accounts for 20÷ 30%. The transverse and the longitudinal impact parameter resolution reaches 10 μm for high p_T tracks, dominated by the resolution of the first pixel hit, while at lower momentum it is degraded by multiple scattering.

Pixel tracker

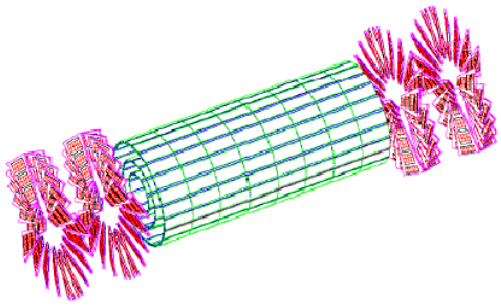

Figure 2.12: *Schematic view of Pixel Trecker system.*

The pixel system is the part of the tracking system closest to the interaction region providing the innermost tracking information. It is formed by pixel cells with size of 100 μm $\times$ 150 μm, that allows a resolution of about 10 μm for the $r-\phi$ coordinate and of about 20 μm for the r-z measurement. These contribute to a precise measurement of tracking point secondary vertices. Thanks to the fine granularity it is expected to have a mean occupancy of 10^{-4} in each LHC bunch crossing. It consists of three barrel layers (BPix) and two endcaps (FPix) and is illustrated in Fig. 2.12. The barrel layers have radii of 4.4 cm, 7.3 cm and 10 cm while the endcap disks are positioned at $\pm$34.5 cm and $\pm$46.5 cm from the nominal interaction in the z direction.

Silicon tracker

The silicon tracker is composed of two different regions: the barrel and endcap (Fig. 2.8).
The barrel region is divided into two parts: the TIB (Tracker Inner Barrel) and the TOB (Tracker Outer Barrel). The TIB comprises the first four layers of detectors characterised by a cell size of 10 cm $\times$ 80 μm made with double-sided (stereo) modules, composed by two detectors mounted back-to-back with the strips tilted by 100 mrad. This solution gives a single hit resolution of 23-34 μm

in $r-\phi$ and 230 μm in z. The TOB is made of six layers. Being further from the interaction point in a region of lower particle density, it is constructed by silicon microstrip detectors with a larger cell size of at most 25 cm $\times$ 180 μm. It ensures a low occupancy in each LHC bunch crossing of around 1% and a resolution of 35-52 μm in $r-\phi$ and 530 μm in z.
The endcaps are divided into the TID (Tracker Inner Disks) and TEC (Tracker End Cap). The three disks of the TID fill the gap between the TIB and the TEC while the TEC comprises nine disks that extend into the region 120 cm $< |z| <$ 280 cm. Both parts are composed of wedge shaped modules arranged in rings, centred on the beam line, and have strips that point towards the beam line.

2.2.2 ECAL

The electromagnetic calorimeter [31, 36, 37] (Fig. 2.13) was designed for the exploration of accurate measurements of the energy and position of electrons and photons. Rare physics processes, such as $H \rightarrow \gamma\gamma$, imposes the strictest requirements on its performance. The calorimeter can also measure the energy of electrons and positrons from the decay of $W^{\pm}$ and Z bosons produced in the decay of an intermediate to high mass Higgs boson. The natural choice to achieve this task is a homogeneous calorimeter. It is composed by 75848 finely segmented lead tungstate ($PbWO_4$) crystals, characterised by high density (8.28 g/cm^3), short radiation length ($X_0 = 0.89cm$), small Molire radius (2.2 cm) and high radiation-hardness. These ensure a fine granularity and a compact calorimeter that are appropriate choice for operation at LHC. Moreover, these crystals are characterised by a very short scintillation-decay time that allows the electronics to collect about 80% of the scintillation light within 25 ns. The relatively low light yield (about 4.5 γ/MeV at 18°) of the crystals requires photodetectors with intrinsic high gain that can operate in a magnetic field. Silicon avalanche photodiodes (APDs) and vacuum phototriodes (VPTs) are used in the barrel and in the endcaps respectively. The Ecal consists of two different parts, a barrel one and an endcap one.

The barrel part (EB) covers the pseudorapidity range $|\eta|$ <1.479. The barrel granularity is 360-fold in ϕ and (2×85)-fold in η, resulting in a total of 61200 crystals. The crystals have a tapered shape, slightly varying with position in η. They are mounted in a quasi-projective geometry to avoid cracks aligned with particle trajectories, so that their axes make a small angle (3°) with respect to the nominal interaction vertex, in both the ϕ and η projections. Crystals are trapezoidal, with a square front face of 22×22 mm^2 corresponds to approximately $\Delta\eta \times \Delta\phi = 0.0174 \times 0.0174$, and 26×26 mm^2 at the rear face. The crystal length is 230 mm corresponding to 25.8 X_0. The barrel crystal volume is 8.14 m^3 and the weight is 67.4 tons.
The endcaps (EE) covers the rapidity range $1.479 < |\eta| < 3.0$. It consists of identically shaped crystals grouped in mechanical units of 5×5 supercrystals (SCs)

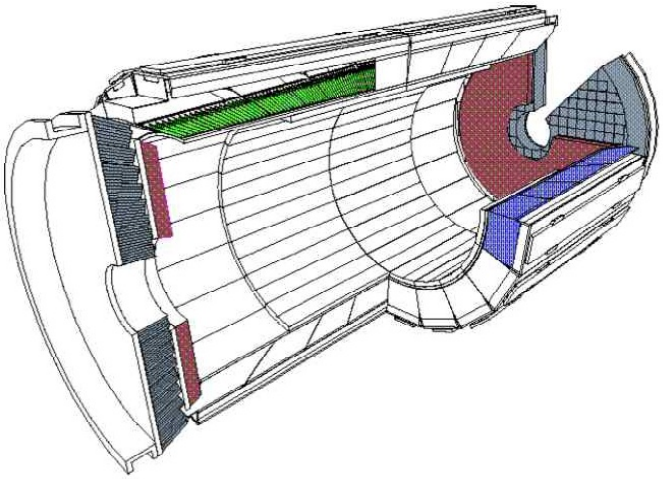

Figure 2.13: *Schematic view of ECAL system.*

consisting of a carbon-fibre alveola structure. Each endcap is divided into 2 halves, or ″Dees ‶. Each Dee holds 3662 crystals. These are contained in 138 standard SCs and 18 special partial supercrystals on the inner and outer circumference. The crystals are arranged in a $x - y$ grid and they point approximately to the interaction point: the axes are tilted at 2°÷ 8°with respect to the line from the nominal vertex position. As for EB, the EE crystals have a trapezoidal shape with a square front face of 28.6×28.6 mm^2 and 30×30 mm^2 rear face: they have a length of 220 mm corresponding at 24.7 X_0. The endcaps crystal volume is 2.90 m^3 and the weight is 24.0 tons.
A pre-shower detectors (SE) [38] are installed in front of each endcaps, consisting of two lead radiators and two planes of silicon strip detectors, with a total radiation length of $3X_0$. It allows rejection of photon pairs from π_0 decays and improves the estimation of the direction of photons, to improve the measurement of the two-photon invariant mass.
The energy (E) resolution of a calorimeter is usually parameterised as

$$\left(\frac{\sigma}{E}\right)^2 = \left(\frac{a}{E}\right)^2 \oplus \left(\frac{b}{E}\right)^2 \oplus c^2 \tag{2.0}$$

where a is the stochastic term and it includes the effects of fluctuations in the number of photo-electrons as well as in the shower containment, b is the noise from the electronics and pile-up and c is a constant term related to the calibration of the calorimeter. The values of the three constants measured on test beams are reported in Table 2.1. The different contributions as a function of the energy are shown in Fig. 2.14.

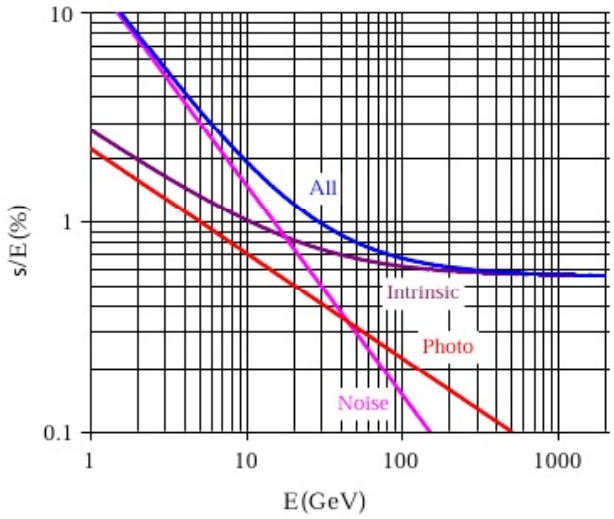

Figure 2.14: *Different contributions to the energy resolution of the ECAL.*

Contribution	Barrel (η=0)	endcap (η=2)
Stochastic term	2.7%	5.7%
Constant	0.55%	0.55%
Noise (low luminosity)	0.155 GeV	0.205 GeV
Noise (hight luminosity)	0.210 GeV	0.245 GeV

Table 2.1: *Contributions to the energy resolution of ECAL.*

2.2.3 HCAL

The HCAL [31, 39, 40, 41] includes four distinct calorimeter subsystems: the hadron calorimeter barrel (HB), the outer calorimeter (HO), the endcap calorimeter (HE) and the forward calorimeter (HF) (see Fig. 2.15).
The HB and the HE are sampling calorimeters where the absorber material is brass and the active material is scintillator. They are inside the CMS superconducting solenoid cryostat and they are separated by a gap which is located approximately at a polar angle of 57 degrees, but is not projective to the center of CMS. They share the pseudorapidity range between 1.3 and 1.4 to minimize the effect of the uninstrumented gap. The HB covers the $|\eta|$ range from zero to approximately 1.4 while HE covers the $|\eta|$ range from 1.3 to 3.0. The construction of HB is in 20 degrees in azimuth wedges, where each wedge has four 5 degrees ϕ sectors. In HE the brass is a single unit for each layer, but the scintillators are

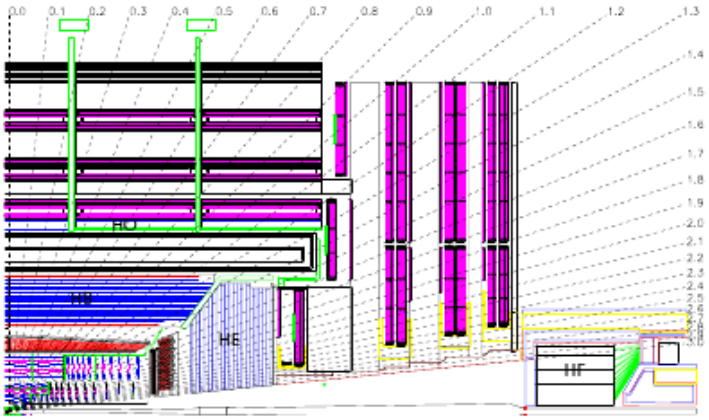

Figure 2.15: *Longitudinal view of the CMS detector showing the locations of the hadron barrel (HB), endcap (HE), outer (HO) and forward (HF) calorimeters.*

constructed in 20 degrees in ϕ wedges, each one has four ϕ segments.
The HB thickness is limited by the magnet cryostat to 5.8 interaction lengths at $\eta = 0$ and 10 interaction lengths at $\eta = 1.2$. As a consequence, layers of scintillators are placed outside the solenoid cryostat to catch the energy leakage of the HB and constitute the outer hadron calorimeter (HO). HO construction is in 30 degrees parts, where each unit has four η and six ϕ segments. The calorimeter tower segmentation in η and ϕ of HB, HE and HO subsystems is 0.087×0.087 except in HE at $|\eta|$ above 2.5 where it is 0.175×0.175.
HF is composed of quartz fiber and iron and covers the forward region of $|\eta|$ between 3.0 and 5.2 to ensure the hermeticity on all solid angle. HF is also constructed in 20 degrees wedges and each wedge contains two 10 degrees ϕ sectors. It is located at a distance of 6 m from the HE and 11.2 m from the IP. The HF will be in the higher radiation environment of all CMS subdetectors. In a typical event the energy density will be approximately about $7\div8$ times greater than the central region. To deal with this challenging environment quartz fibres were chosen as the active medium embedded in an absorber of diffusion welded steel plates. The HF is segmented with 0.175×0.175 except for $|\eta|$ above 4.7 where the segmentation is 0.175×0.35.
Portions of each of the four HCAL subsystems were placed in a CERN test beam to measure the characteristics and obtain a reference calibration. The electromagnetic calorimeter (ECAL) was also included the test beam setup.The hadronic energy resolution is parameterized as

$$\frac{\sigma}{E} = \frac{a}{\sqrt{E}} \oplus b, \tag{2.0}$$

where a is the stochastic and b the constant term. For the barrel HCAL and ECAL combination, one measures $a = 84.7 \pm 1.6\%$ and $b = 7.4 \pm 0.8\%$. The energy resolution of the endcap is similar to the barrel. The corresponding values for HF are $a = 198\%$ and $b = 9\%$.

2.2.4 Muon system

As implied by the experiments middle name, the detection of muons is of central importance to CMS, being a powerful tool to recognize signatures of interesting processes, like the predicted golden-plate Higgs decays into ZZ or ZZ^* then decaying into four muons, over the very high QCD background rate expected at LHC with full luminosity or like many interesting SUSY processes involve muons in the final state. Therefore a precise and robust muon measurement was a central theme from its earliest design stages. The muon system [42, 43] has 3 functions: muon identification, momentum measurement, and triggering. The high magnetic field enables good muon momentum resolution ($\Delta p_T/p_t \sim 10\%$ at p_T= 1TeV) while the big amount of material in the flux-return yoke serves as hadron absorber for the identification of muons. The material thickness crossed by muons, as a function of pseudorapidity, is shown in Fig. 2.16. The muon

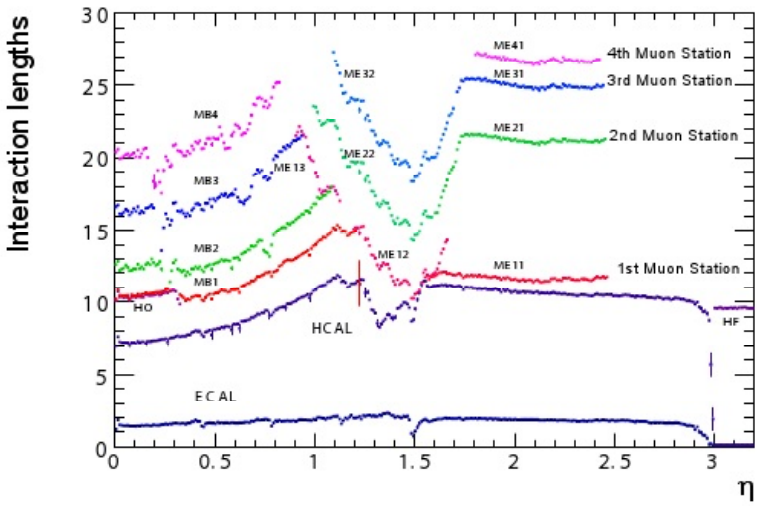

Figure 2.16: *Material thickness in interaction lengths at various depths, as a function of pseudorapidity.*

system of CMS is composed by 3 different types of gaseous particle detectors DT, CSC and RPC (Fig. 2.17). Due to the shape of the solenoid magnet the muon system was naturally driven to have a cylindrical *barrel* section and two planar *endcaps* regions. The berrel is composed of five mechanically independent

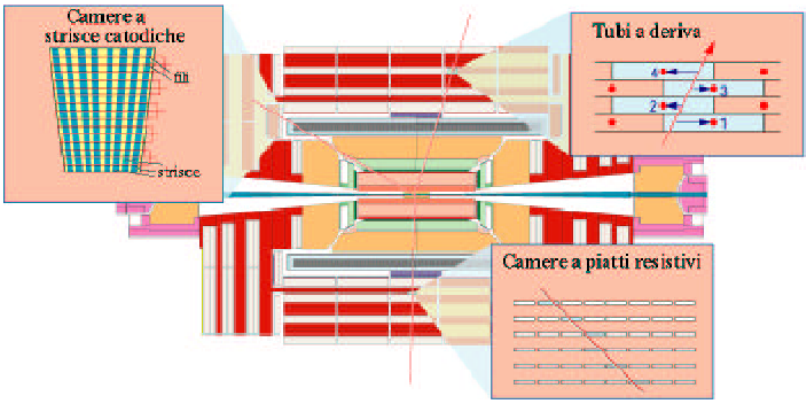

Figure 2.17: *Muon system.*

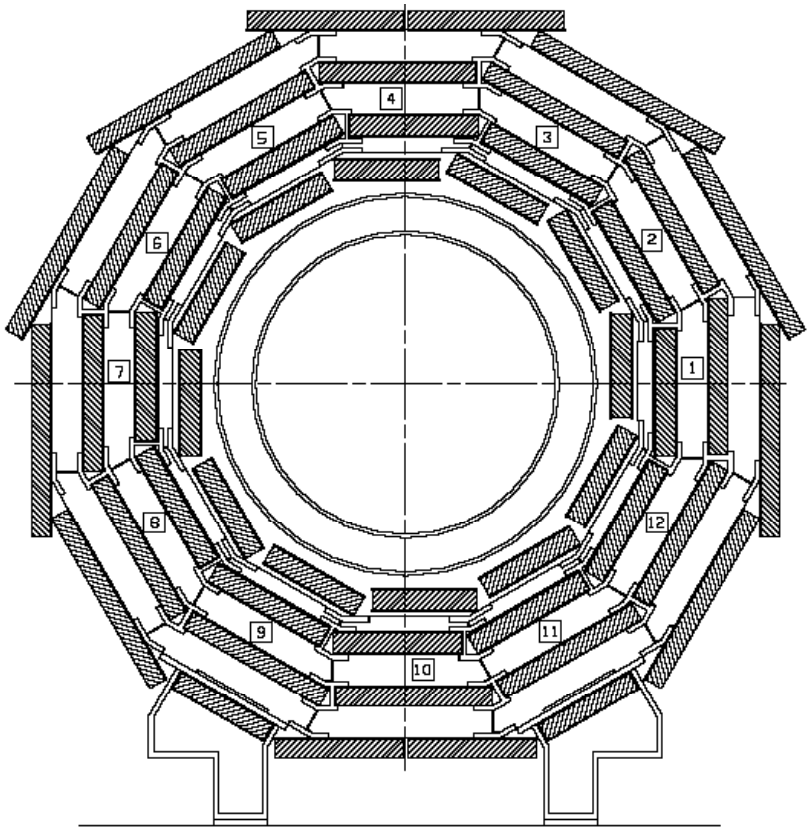

Figure 2.18: *Trasversal view of CMS barrel wheel.*

wheels (Wheel±1, Wheel±2, Wheel0). Each wheel is divided in twelve sectors (Fig. 2.18) and every sector consists of four detector stations integrated in the magnet return yoke. Each of the endcap (Fig. 2.19) is composed of four disks, called stations (ME1, ME2, ME3, ME4), that close the magnet circuit of CMS. The station ME1 is divided in three concentric rings, while the other three are composed of two rings. With this geometrical layout the muon detector elements cover the full pseudorapidity interval $|\eta|$ <2.4 with no acceptance gaps. The muon

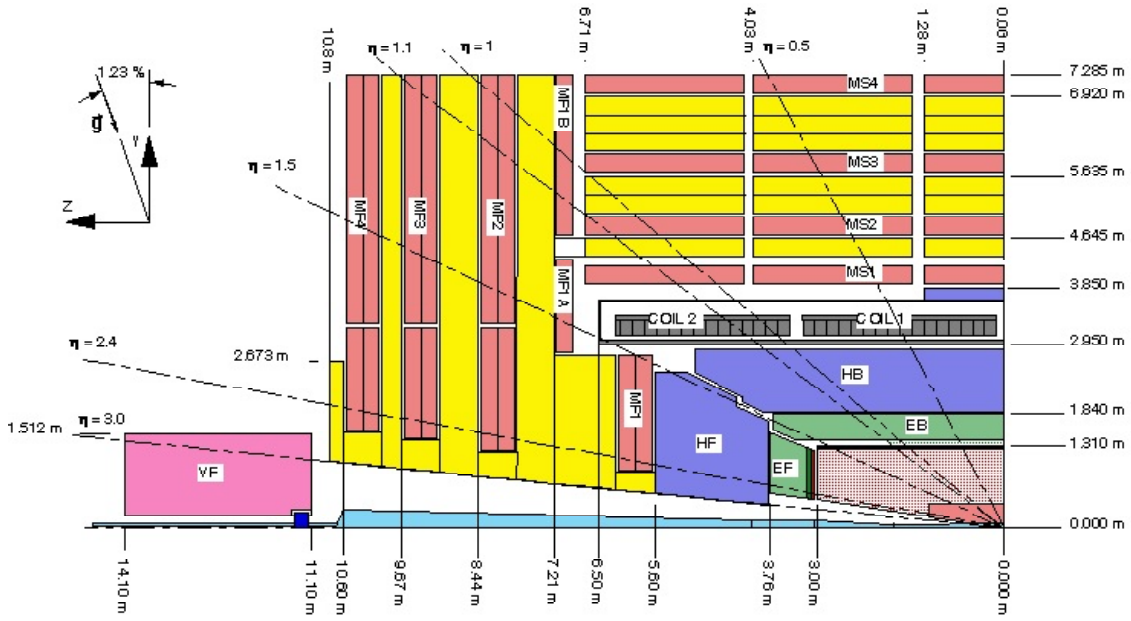

Figure 2.19: *Longitudinal view of CMS muon sistem, in which are shown the encap and three barrel wheels.*

system consists of about 25000 m^2 of detection planes, that allow robustness and redundancy.

In the barrel region, where the neutron-induced background is small, the muon rate is low and the magnetic field is uniform and mostly contained in the steel yoke, Drift chambers with standard rectangular drift cells are used. The DT chambers [31, 44] cover the pseudorapidity region $|\eta| < 1.2$. and are organized into 4 stations interspersed among the layers of the flux return plates.

The muon system uses cathode strip chambers [31, 45] (CSC), in the endcap regions of CMS, where the muon rates and background levels are high and the magnetic field is large and non-uniform. They are characterised by a fast response time, fine segmentation, and radiation resistance. CSCs cover an angular range between $|\eta|$ values of 0.9 and 2.4. They are organized in 4 stations in each end-

cap, with chambers positioned perpendicular to the beam line and interspersed between the flux return plates. The cathode strips of each chamber run radially outwards and provide a precision measurement in the $r-\phi$ bending plane. The anode wires run approximately perpendicular to the strips and are also read out in order to provide measurements of $|\eta|$ and the beam-crossing time of a muon.

To ensure redundancy and the highest efficiency in the possible high background rates, a complementary dedicated trigger system of resistive plate chambers was added in both the barrel and endcap regions. The RPCs [31, 46, 47] provide a fast, independent, and highly-segmented trigger in the rapidity range $|\eta| < 1.6$. The RPCs are double-gap chambers, operated in avalanche mode to ensure good operation at high rates. They produce a fast response of the order of few ns but a coarser position resolution than the DTs or CSCs. They also help resolve ambiguities in attempting to make tracks from multiple hits in a chamber. A total of 6 layers of RPCs are embedded in the barrel muon system, 2 chambers in each of the first two stations, and 1 in each of the last 2 stations. The redundancy in the first 2 stations allows the trigger algorithm to work even for low-p_T tracks that may not reach the outer 2 stations. In the endcap region, the RPC system composes of one plane in each of the 3 stations.

DT chambers

A schematic layout of a DT chamber and of a DT cell are shown in Fig. 2.20 and Fig. 2.21 respectively. In each chamber there are 12 layers of contiguous drift tube cells grouped in three SuperLayers (SL) with 4 staggered layers each. The innermost and outermost SLs are dedicated to hits measurement in the CMS bending plane ($r-\phi$ plane), while in the central SL the hits are measured along the beam axis ($r-z$ plane). The outermost stations (MB4) located outside the iron return yokes of the CMS magnet have only the two SLs measuring the hit position in the $r-\phi$ plane. Each cell has an area of 13×4.2 cm^2 where 4.2 cm is the distance beetwen two consecutive anode wire. The cells are separated by 1 mm thick aluminium and have a offset of half cell with respect to the upper and lower neighbor cell. With this design, the efficiency to reconstruct a high p_T muon track with a momentum measurement delivered by the barrel muon system alone is better than 95% in the pseudorapidity range covered by four stations, $|\eta| < 0.8$.

The 100 μm target chamber resolution in $r-\phi$ plane is achieved by the 8 track points measured in the two $r-\phi$ SLs, the single wire resolution being better than 250 μm. To perform a precise BX assignment the deviation from linearity of the space-time relation in each drift cell must be less than 100-150 μm. A multi-electrode design (1 anode wire, 2 field shaping strips, and 2 cathode strips) ensures this performance also in the regions with stray magnetic field.
The DT system consists of 130 chambers, 60 chambers located in the inner three wheel(0,±1) and 70 chambers in the outer ones(W±2), with about 172000 sensi-

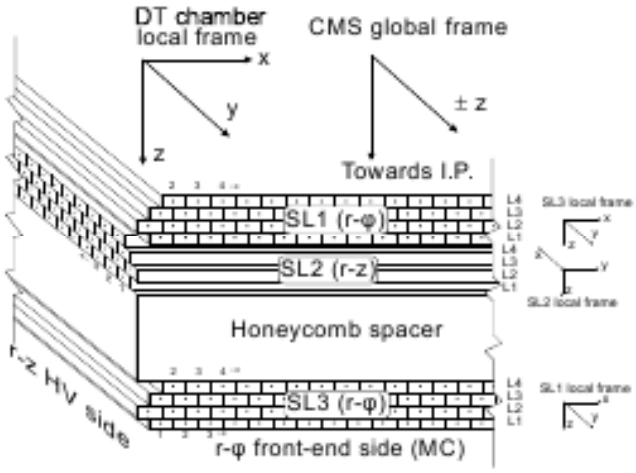

Figure 2.20: *A DT chamber in position inside the iron yoke; the view is in the $(r-\phi)$ plane. One can see the 2 SLs with wires along the beam direction and the other perpendicular to it. In between is a honeycomb plate with supports attached to the iron yoke.*

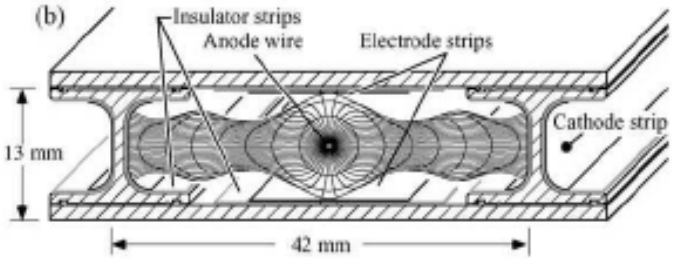

Figure 2.21: *Schematic view of a DT cell showing drift lines and isochrones.*

tive wires.

CSC chambers

The CMS Endcap Muon system will consist of 468 cathode strip chambers (CSC) arranged in groups as follows: 72 ME1/1, 72 ME1/2, 72 ME1/3, 36 ME2/1, 72 ME2/2, 36 ME3/1, 72 ME3/2, and 36 ME4/1 (Fig. 2.22). The de-scoped 72 ME4/2 chambers will not be available during early years of CMS operation. The chambers are trapezoidal and cover either 10°or 20°in ϕ; all chambers, except for

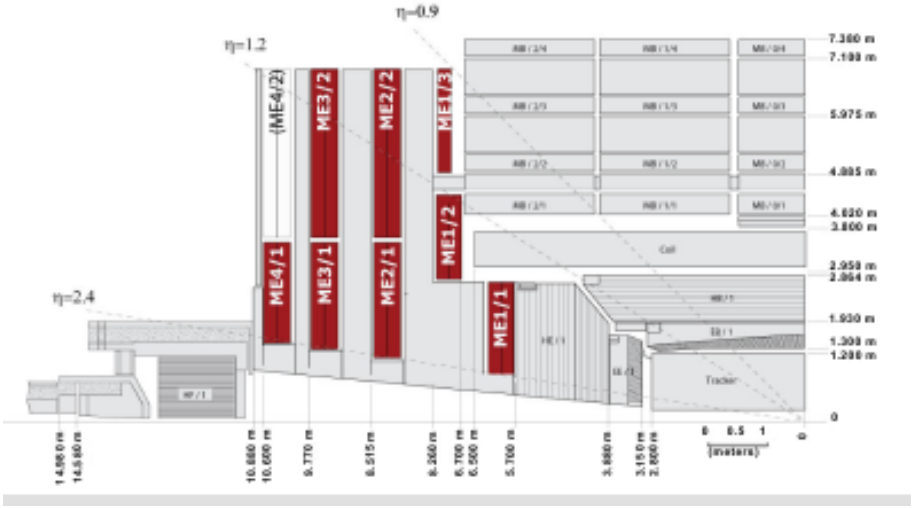

Figure 2.22: *Quarter-view of the CMS detector. Cathode strip chambers of the Endcap Muon system are highlighted.*

the ME1/3, overlap and provide contiguous ϕ-coverage. A muon in the pseudorapidity range $1.2 < |\eta| < 2.4$ crosses 3 or 4 CSCs. The CSCs are multiwire proportional chambers comprised of 6 anode wire planes interleaved among 7 cathode panels (Fig 2.23). Wires run azimuthally and define a tracks radial coordinate. Strips are on cathode panels and run lengthwise at constant $\Delta\phi$ width. The largest chambers, ME2/2 and ME3/2, are about 3.4×1.5 m^2 in size. The overall area covered by the sensitive planes of all chambers is about 5000 m^2, for a gas volume more than 50 m^3 , and a number of wires of about 2 million. There are about 9000 high-voltage channels in the system, about 220000 cathode strip read-out channels with 12-bit signal digitization, and about 180000 anode wire read-out channels. This system will ensure at least 99% efficiency per chamber for finding track stubs by the Level-1 trigger and at least 92% probability per chamber of identifying correct bunch crossings by the Level-1 trigger. This efficiency per chamber and 3-4 CSCs on a muon track path, ensure that the reconstructed muons will be assigned the correct bunch crossing number in more than 99% of cases. The CSC system guarantees a $r - \phi$ resolution at the Level-1 trigger of about 2 mm, that improves up to 75 μm in off-line reconstruction for ME1/1 and ME1/2 chambers and about 150 μm for all others.

RPC chambers

The Resistive Plate Chambers are gaseous parallel-plate detectors that combine adequate spatial resolution with a time resolution comparable to that of scintil-

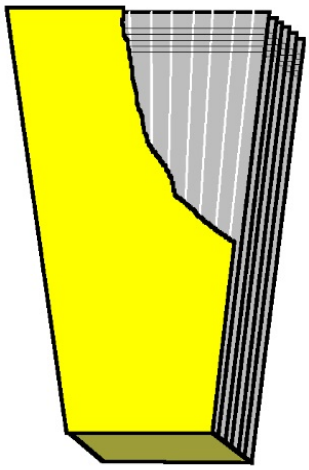

Figure 2.23: *Layout of a CSC chamber, made of 7 trapezoidal panels.*

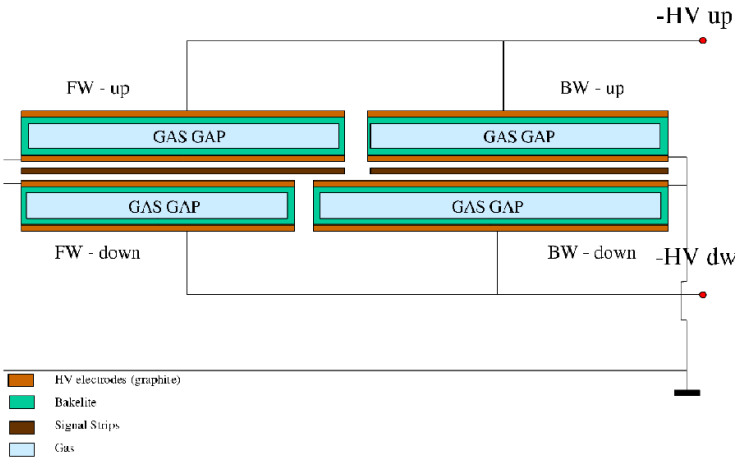

Figure 2.24: *Schematic view of a RPC chamber of CMS.*

lators (order of ns). These performances make, the RPCs capable of tagging the time of an ionising event in a much shorter time than the 25 ns between two

consecutive LHC bunch crossings (BX). Therefore, a fast dedicated muon trigger device based on RPCs can identify unambiguously the relevant BX to which a muon track is associated even in the presence of the high rate and background expected at the LHC. Signals from such devices directly provide the time and position of a muon hit with the required accuracy. A trigger based on RPCs has to provide the BX assignment to candidate tracks and estimate the transverse momenta with high accuracy in an environment where rates may reach 10^3 Hz/cm^2. The CMS RPC chambers consist of 2 or 3 double-gap modules:

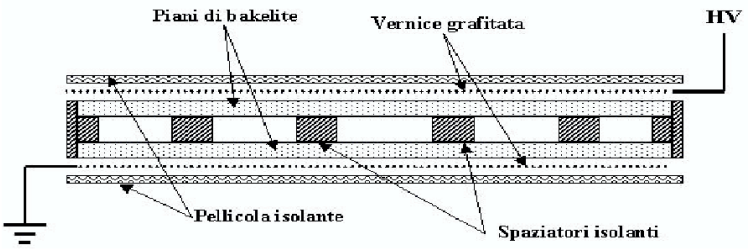

Figure 2.25: *A RPC single gap.*

forward, middle, backward (Fig. 2.24), made by two superimposed single gaps (up and down). Every single gap is formed by two bakelite electrode plates (Fig. 2.25) characterised by a bulk resistivity of $1 \div 2 \times 10^{10} \Omega cm$ mantained at a distance of 2 mm by polycharbonate bottons. This double-gap configuration with common read-out strips in between, allows to operate the single-gaps at lower gas gain (lower high voltage) with an effective detector efficiency higher than for a single-gap, because the induced signal is the sum of the 2 single-gap signals. The system works in avalanche mode or low gain mode, that ensures few deposit charge on the electrodes with small dead zone on the plate. This choice, imposed by high particle flux of LHC, requires a vary good front-end electronics enables to work with signal of a amplitude of few pC.
Six layers of RPC chambers are embedded in the barrel iron yoke, two located in each of the first and second muon stations (RB1, RB2) and one in each of the two last stations (RB3, RB4) (Fig 2.26). The redundancy in the first two stations allows the trigger algorithm to perform the reconstruction always on the basis of 4 layers, even for low p_T particles, which may stop inside the iron yoke. In total there are 480 rectangular chambers, each one 2455 mm long in the beam direction. Exceptions are the chambers in sector 3 of wheel-1 and sector 4 of wheel+1, which are 2055 mm long to allow passage of the magnet cooling chimney. Chambers RB1, RB2, and RB3 have widths 2080, 2500, and 1500 mm, respectively. The widths of the RB4 chambers which depend on the location. The strips run along the beam direction providing position measurements in the

$r - \phi$ plane .
In the endcap region, the baseline design foresees the instrumentation of the iron disks with 4 layers of RPCs to cover the region up to $|\eta| = 2.1$. They are mounted on both faces of the disks. The double-gaps in every station have a trapezoidal shape and are arranged in 3 concentric rings in the $r - \phi$ view. They overlap in ϕ to avoid dead space at chamber edges. Except for station 1, the chambers of the innermost ring span 20 in ϕ , all others span 10. However, in the first phase, due to budget limitations, only 3 layers up to $|\eta| = 1.6$ are built. A schematic view of endcap RPC system is given in Fig. 2.27.

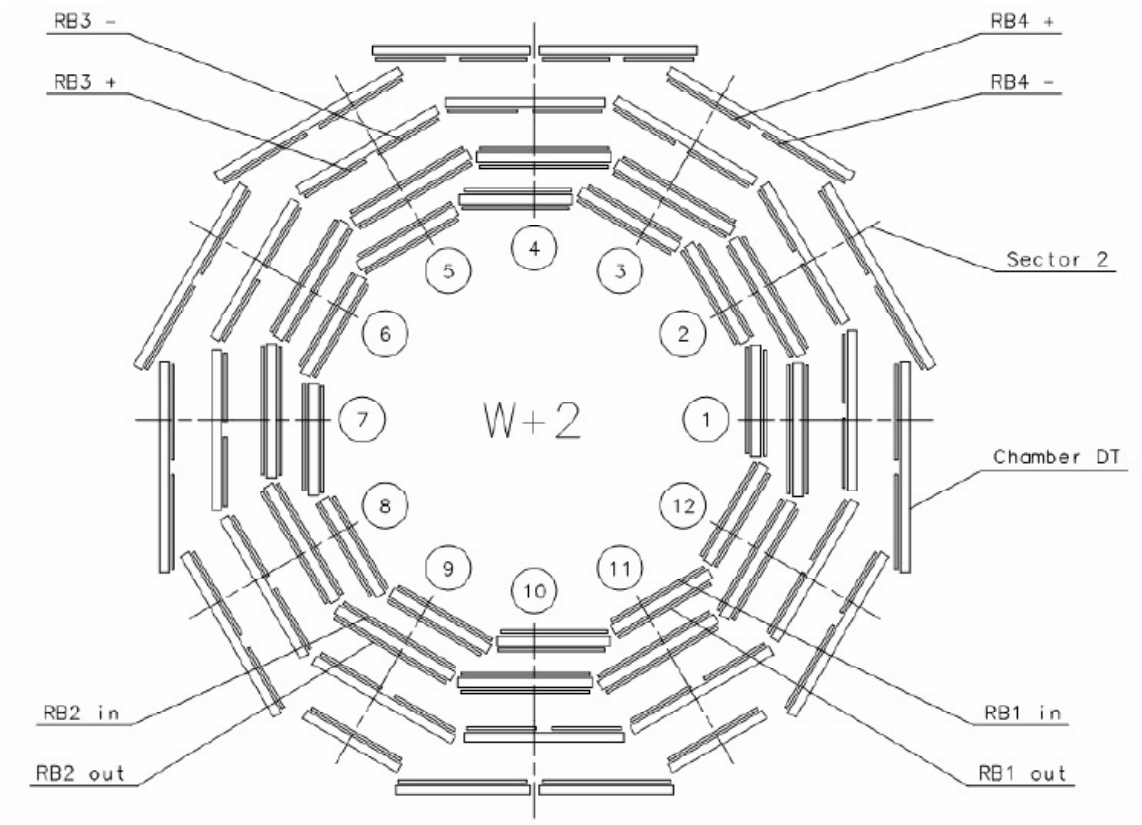

Figure 2.26: *Schematic layout of the barrel RPC system. Each wheel is divided into 12 sectors that are numbered as shown.*

2.2.5 The CMS Trigger

At the LHC nominal luminosity, the total event rate is of the order of 10^9 Hz. However, the rate of interesting events is very small(Fig 2.28). A large fraction of the event selection has to be performed on-line, since the raw event size is of

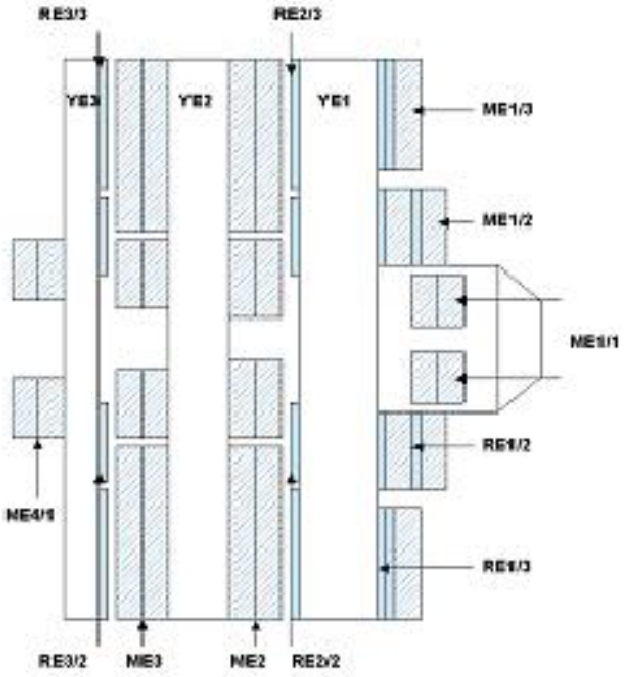

Figure 2.27: *Schematic layout endcap RPC system.*

the order of 1 MB and storing and processing the resulting amount of data would be prohibitively difficult and expensive. This task is performed by the trigger system, which is the vary first phase of the physics event selection process. The rate is reduced in two steps called Level-1 Trigger [31, 48] (L1) and High-Level Trigger [31, 49] (HLT), respectively (Fig. 2.29).

The Level-1 Trigger consists of custom-designed, largely programmable electronics, whereas the HLT is a software system implemented in a filter farm of about one thousand commercial processors. This allows full flexibility and optimisation of the algorithms. Although this classification is somewhat arbitrary, the HLT is further subdivided in logical levels (Level-2, Level-3). There rate reduction capability is designed to be at least a factor of 10^6 for the combined L1 Trigger and HLT. The design output rate limit of the L1 Trigger is 100 kHz. Only one third of this bandwidth is allocated, the rest being used as safety margin accounting for all uncertainties in the simulation of the basic physics processes.

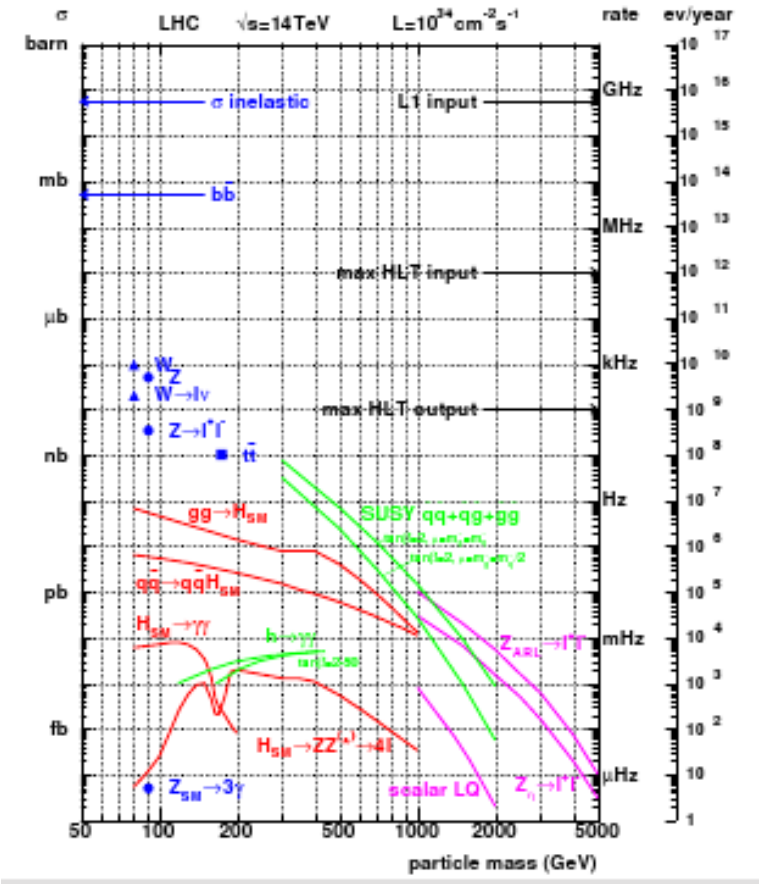

Figure 2.28: *Cross section and event rates at* $L = 10^{34} cm^{-2} s^{-1}$ *as a function of the mass of produced objects.*

Level-1 Trigger

The L1 (Fig. 2.30), implemented on custom programmable hardware, has to analyze every bunch crossing. This is achieved with a synchronous pipelined structure of processing elements, each taking less than 25 ns to complete. At every bunch crossing, each processing element passes its results to the next element and receives a new event to analyse. During this process, the complete detector data are stored in pipeline memories, whose depth is technically limited to 128 bunch crossings. The L1 decision is therefore taken after a fixed time of 3.2 μs. The L1 electronics is housed partly on the detectors, partly in the underground control room located at a distance of approximately 90 m from the experimental cavern, therefore the decision time must include also the transmission time between the detector and the counting room (a cable path of up to 90 m each way) and, in the case of Drift Tube detectors, the electron drift times (up to 400 ns). The

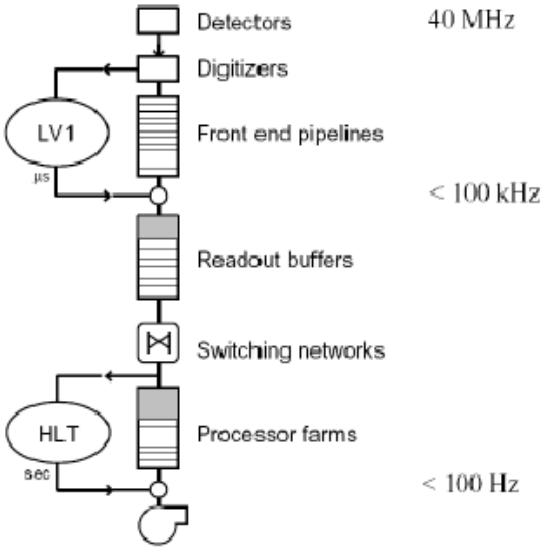

Figure 2.29: *Schematic view of the CMS Trigger system, in which the different trigger levels and event rates are shown.*

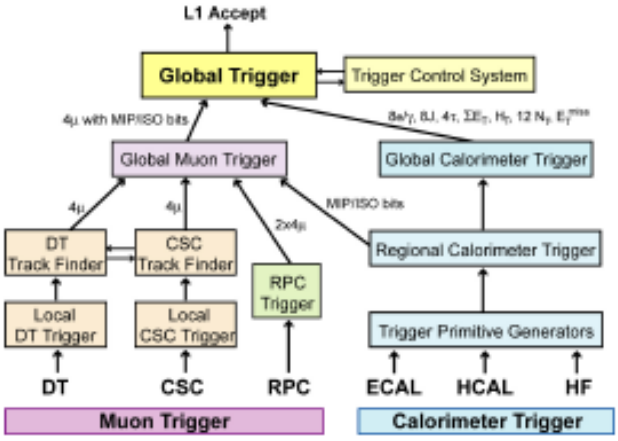

Figure 2.30: *Architecture of the L1 Trigger.*

effective time available for calculations can therefore be as low as 1 μs.

The Level-1 trigger is divided in three subsystems: the Calorimeter Trigger, the Muon Trigger and the Global Trigger. The Muon Trigger is further subdi-

vided in three independent systems for the DTs, CSCs and RPCs, respectively. The results of these three systems are combined by the Global Muon Trigger (see Fig 2.31). The Calorimeter and Muon Triggers do not perform any selection themselves. They identify trigger objects of different types: isolated and non-isolated electrons, photons and muons; forward, central and τ-jets. The four best candidates of each type are selected and sent to the Global Trigger, together with the measurement of their position, transverse energy or momentum, and a quality word. In addition the Calorimeter trigger send information about the total and missing transverse energy measurements. The Global Trigger selects the events according to programmable trigger conditions, that can include requirements on the presence of several different objects with energies or momenta above predefined thresholds. Topological conditions and correlations between objects can be required as well. Up of 128 of these conditions can be tested in parallel, and each can be pre-scaled to accept only a fraction of selected events.

Calorimeter trigger

The Calorimeter Trigger begins with trigger tower energy sums formed by the ECAL, HCAL and HF upper level readout Trigger Primitive Generator (TPG) circuits from the individual calorimeter cell energies. For the ECAL, these energies are accompanied by a bit indicating the transverse extent of the electromagnetic energy deposit. The TPG information is transmitted over high speed copper links to the Regional Calorimeter Trigger (RCT), which finds candidate electrons, photons, taus, and jets. The RCT separately finds both isolated and non-isolated electron/photon candidates. The RCT transmits the candidates along with sums of transverse energy to the Global Calorimeter Trigger (GCT). The GCT sorts the candidate electrons, photons, taus, and jets and forwards the top 4 of each type to the global trigger. The GCT also calculates the total transverse energy and total missing energy vector. It transmits this information to the global trigger as well. The RCT also transmits an $\eta - \phi$ grid of quiet regions (region where the energy deposit are below a programmable threshold) and a MIP bit (energy deposit comparable to a Minimum Ionising Particle) to the global muon trigger for muon isolation cuts.

For trigger purposes, the calorimeters are subdivided in towers with a size of $\Delta\eta \times \Delta\phi = 0.087 \times 0.087$ up to $\eta = 2$. At higher pseudorapidity values $\Delta\eta$ increases up to 0.35. Trigger towers match the granularity of HCAL up to η larger than 1.74; above that value, physical HCAL towers have twice the ϕ dimension of the trigger tower. In the barrel ECAL, each tower corresponds to 5 $\times$ 5 crystals, while the ECAL endcap crystals are arranged in a $x - y$ geometry, and a variable number of crystals is grouped, matching as much as possible the HCAL trigger tower boundaries. Towers are defined also in the very forward calorimeter, with a size of $\Delta\eta \times \Delta\phi = 0.348 \times 0.5$. The trigger towers are organised in calorimeter regions, each formed by 4×4 trigger towers, with a size

of about $\Delta\eta \times \Delta\phi = 0.35 \times 0.35$. Very forward calorimeter towers constitute a region by themselves, due to their low size.

Muon trigger

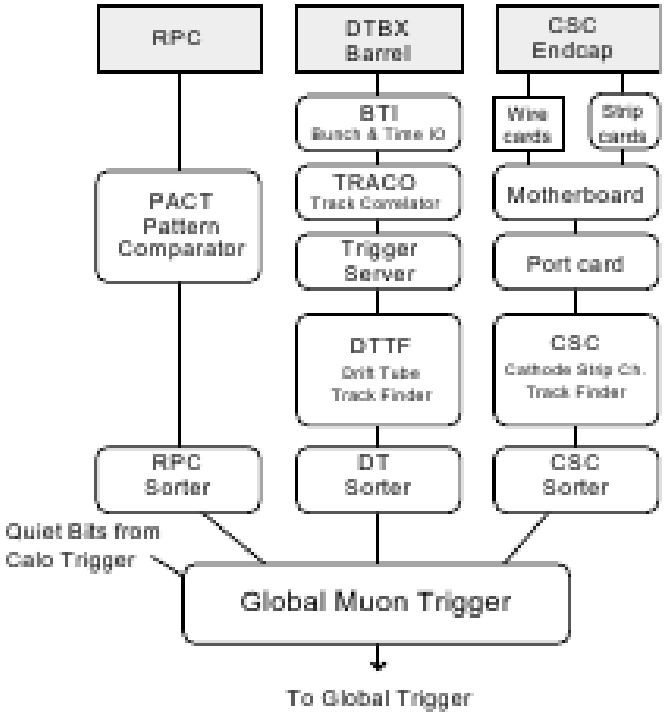

Figure 2.31: *Architecture of the L1 muon Trigger.*

The Muon Trigger (Fig. 2.31) has the task to identify muons, reconstruct their position and transverse momentum and provide bunch crossing assignment with high purity and efficiency. Even if the design coverage is $|\eta| \leq 2.4$, the not complete installation of electronics in the forward CSC station ME1/1, imposes that the L1 trigger acceptance rise up to $|\eta| < 2.1$. Each of the muon subdetectors of muon system have a L1 muon trigger systems with own trigger logic.

The Barrel Muon Drift Tubes are equipped with Bunch and Track Identifier (BTI) electronics that finds track segments from coincidences of aligned hits in 4 layers of one drift tube superlayer. The track segments positions and angles are sent to the Track Correlator (TRACO), which attempts to combine the segments from the two SLs measuring the ϕ coordinate. The best combinations from all TRACOs of a single chamber together with the SL η segments are collected by

the Trigger Server. The Trigger Server then sends the best two segments (if found) to the Track Finder, which combines the segments from different stations into full muon tracks and assigns p_T values to them.

The CSC form Local Charged Tracks (LCT) from the Cathode Strips, which are combined with the anode wire information for bunch crossing identification on a Trigger Motherboard. The LCT pattern logic assigns a p_T and quality, which is used to sort the LCT on the Motherboard and the Muon Port Card (MPC) that collects LCTs from up to 9 CSC chambers. The top 3 LCTs from all the MPCs in a sector are transmitted to the CSC Track Finder, which combines the LCTs into full muon tracks and assigns p_T values to them. The CSC and DT Track-Finders exchange track segment information in the region where the chambers overlap.

The RPC strips are connected to a Pattern Comparator Trigger (PACT), which is projective in η and ϕ. The PACT forms trigger segments which are connected to segment processors which find the tracks and calculate the p_T. The RPC logic also provides some hit data to the CSC trigger system to improve resolution of ambiguities caused by 2 muons in the same CSC.

The Global Muon Trigger sorts the RPC, DT and CSC muon tracks, converts these tracks into the same η, ϕ and p_T scale, and validates the muon sign. It then attempts to correlate the CSC and DT tracks with RPC tracks. It also correlates the found muon tracks with an η-ϕ grid of quiet calorimeter towers to determine if these muons are isolated.

Up to four muon candidates satisfying some minimal quality criteria and with the highest p_T are forwarded to the Global Trigger for further processing. The two main L1 muon triggers are the single-muon and double-muon triggers. The type of events contributing to the Level-1 muon trigger rate depends on the p_T threshold used. Pion and kaon decays dominate in the p_T region around 5 GeV/c (although the probability of decay in the volume in front of the calorimeter is small, the number of hadrons is very high). Leptons from b and c-quark decays dominate in the 5 GeV/c $< p_T <$ 35 GeV range, whereas at higher p_T values $Z \rightarrow \mu\mu$ and $W \rightarrow \mu\nu$ events are the main components. At a luminosity of $10^{32} cm^{-2} s^{-1}$, the L1 single-muon rate is about 1 kHz for thresholds as low as 7 GeV/c while the di-muon rate is smaller than 200 Hz at the lowest useful threshold of 3 GeV/c.

L1 Global Trigger

The L1 Global Trigger is responsible for collecting objects created from the Calorimeter and Muon Triggers and for making a decision whether to retain the event or not. If the event is accepted the decision in sent to the Timing Trigger and Control System, that commands the readout of the remaining subsystems. In order to take the decision, the L1 Global Trigger sorts the ranked objects produced by calorimetry and muon system and checks if at least one of

the thresholds in the Level-1 Trigger table is passed. Since there are large uncertainties in the cross section of many processes, the L1 trigger thresholds for the initial low luminosity data taking have been designed for an output rate of 16 kHz, instead of the planned 50 kHz, that is the design limit for low luminosity. The L1 trigger table is reported in Table 2.2.

Trigger	Threshol (GeV/c^2 or GeV/c)	Rate (kHz)	Cumulative Rate (kHz)
Inclusive isolated e/γ	29 (34)	3.3 (6.5)	3.3 (6.5)
Di-e/di-γ	17 (19)	1.3 (3.3)	4.3 (9.4)
Inclusive isolated μ	14 (20)	2.7 (6.2)	7.0 (15.6)
Single τ -jet	86 (101)	2.2 (5.3)	10.1 (22.6)
Two τ-jet	59 (67)	1.0 (3.6)	10.9 (25.0)
1-jet, 3-jets, 4-jets	177,86,70 (250,110,95)	3.0 (3.0)	12.5 (26.7)
Jet $\times$ E_T^{miss}	86 $\times$ 46 (113 $\times$ 70)	2.3 (4.5)	14.3 (30.4)
e$\times$ jet	21$\times$ 45 (25$\times$ 52)	0.8 (1.3)	15.1 (31.7)

Table 2.2: *Level-1 Trigger table at low (nominal) luminosity. Thresholds correspond to* 95% *efficincy. Low luminosity:* $L = 10^{32} cm^{-2} s^{-1}$.

The CMS High Level Trigger

The High Level Trigger is designed to reduce the L1 output rate to the goal of 100 events/s that are definitely going to be written to mass storage. HLT code runs on commercial processors and performs reconstruction using the information from all subdetectors. Data read from subdetectors are assembled by a builder unit and then assigned to a switching network that dispatches events to the processor farm. The CMS switching network has a bandwidth of 1Tbit/s. This simple design ensures maximum flexibility to the system, the only limitation being the total bandwidth and the number of processors. The system can be easily upgraded adding new processors or replacing the existing ones with faster ones as they become available. Since the algorithm implementation is fully software, improvements in the algorithms can be easily implemented and do not require any hardware intervention. Event by event, the HLT code is run on a single processor, and the time available to make a decision is about 300 ms. The real-time nature of this selection imposes several constraints on the resources an algorithm can use. The reliability of HLT algorithms is of capital importance, because events not selected by the HLT are lost. In order to efficiently process events the HLT code has to be able to reject not interesting events as soon as possible; computationally expensive algorithms must run only on good candidates for interesting events. In

order to meet this requirement the HLT code is organized in a virtually layered structure:

- Level 2: uses only muon and calorimetry informations;
- Level 2.5: uses also the pixel informations;
- Level 3: makes use of the full information from all the tracking detectors.

Each step reduces the number of events to be processed in the next step. The most computationally expensive tasks are executed in the Level 3; time consuming algorithms such as track reconstruction are only executed in the regions of interest. Moreover, since the ultimate precision is not required at HLT, track reconstruction is performed on a limited set of hits, and is stopped once the required resolution is achieved. Table 2.3 summarizes the HLT requirements at low luminosity to match the cumulative rate of 100 Hz. Table 2.4 shows the expected efficiency for the benchmark physics channels.

Trigger	Threshold (GeV/c^2 or GeV/c)	Rate (kHz)	CPU time (kHz)
1e, 2e	29, 17	33, 1	160
1μ, 2μ	19, 7	25, 4	710
1τ, 2τ	86, 59	3, 1	130
Jet $\times$ E_T^{miss}	180 $\times$ 123	5	50
Inclusive b jets	237	5	300

Table 2.3: *High-Level Trigger thresholds at* $L = 10^{32} cm^{-2} s^{-1}$ *for various channels. The CPU time refer to a 1 GHz Intel Pentium III CPU.*

Channel	Efficiency
$H(115 GeV/c^2) \rightarrow \gamma\gamma$	77%
$H \rightarrow ZZ \rightarrow 4\mu$	99%
SUSY (0.5 TeV/c^2 sparticles	60%
$W \rightarrow e\nu_e$	67%
$W \rightarrow e\nu_\mu$	69%
$t\bar{t} \rightarrow \mu X$	72%

Table 2.4: *Performance of HLT selection at* $L = 10^{32} cm^{-2} s^{-1}$ *after applying the cuts listed in table 2.3.*

Chapter 3

Muon and Z boson reconstruction in the CMS detector

In a hadron collider leptons provide a clear signature for many of the most interesting physics processes, therefore a precise and fast reconstruction of the leptons is mandatory. In this context the muons play a key role as their parameters can be measured with great precision and, at least at high p_T, they can be identified unambiguously. Muon reconstruction [50] is also the first step of the reconstructed $Z \to \mu^+\mu^-$ decays.
In first part of this chapter the algorithms of the muon reconstruction and their performance will be described. The reconstruction in the muon spectrometer starts with the reconstruction of hit positions in the DT, CSC and RPC subsystems. Hits within each DT and CSC chamber are then matched to form segments (track stubs). The segments are collected and matched to generate seeds that are used as a starting point for the actual track fit of DT, CSC and RPC hits. The result is a reconstructed track in the muon spectrometer, and is called standalone muon. Standalone muon tracks are then matched with tracker tracks to generate global muon tracks, exploiting the full CMS resolution. Tracker muons are muon objects reconstructed with an algorithm that starts from a silicon tracker track and looks for compatible segments in the muon chambers. A unique collection of muon objects is assembled from the stand- alone, global, and tracker muon collections. Muon isolation quantities using calorimeter information and tracker tracks for muons defined at the three different levels are combined into the muon objects.
In second part of this chapter the strategy of the Z boson reconstruction from a muons pair will be described and the comparison with Monte Carlo (MC) generated particles will be shown too.

3.1 Reconstruction steps

In order to reconstruct a physical particle traveling through the detector, the hits from the position sensitive detectors are associated together using a pattern recognition algorithm to associate the measurements with trajectories. Independently of the sub detector information used the procedure from hits to tracks follows the same sequence and reconstructing and parameterizing a track occurs in four stages:

1. trajectory seeding,
2. trajectory building,
3. trajectory cleaning,
4. trajectory smoothing.

The characteristics of the trajectory as it travels through the detector are finally used to define its momentum, charge, and particle identification [51, 52].

3.1.1 Trajectory seeding

The initial point for the track reconstruction is determined using an estimated trajectory state or set of hits that are compatible with the assumed physics process. The most common types of trajectory seeds in CMS are hit-based seeds and state-based seeds and it is assumed that the trajectories, and therefore the trajectory seeds, are compatible with the beam spot. Hit-based seeds require a hit-pair or hit-triplet compatible with the beam spot to provide the initial vector. Additional options are that the seed direction meet certain criteria, or that the hits be located in a certain geometric region of the detector. State-based seeds do not require any hits and are specified by an initial momentum and direction.

3.1.2 Trajectory building

The Trajectory building starts at the position specified by the trajectory seed, and the building then proceeds in the direction specified by the seed to locate compatible hits on the subsequent detector layers. The track finding and fitting is accomplished using a combinatorial Kalman filter [54] where the full knowledge of the track parameters at each detector layer is used to find compatible measurements in the next detector layer, forming combinatorial trees of track candidates. The Kalman filter method uses an iterative approach to update the trajectory estimate to the next surface with known equations of motion. In this process, the trajectory state which is propagated to the next detector layer is then updated with the information of a compatible hit. The final trajectory estimate is properly weighted with information from the last measurement and the information

with predicted state based in all preceding detectors. Several propagators are used during the muon track reconstruction to predict the state of a muon given its initial state vector. The propagators provide a solution for muon transport in the detector accounting for perfect knowledge of magnetic field B, and energy loss in detector material to predict the mean expected path as well as provide a propagation of initial state errors (covariance matrix) to the propagation final point including material effects like multiple scattering and energy loss fluctuations.
Three propagators are used at different stages of muon reconstruction: the *analytic with material* propagator [50] , the *Runge-Kutta* propagator [50], and the *stepping-helix* propagator [50]. The first two propagators are used extensively inside the silicon tracker volume, while the latter is predominantly used to propagate muons outside the tracker volume.

3.1.3 Trajectory cleaning

The Trajectory building produces a large number of trajectories, many of which share a large fraction of their hits. In the cleaning stage, ambiguities among the possible trajectories are resolved and a maximum number of track candidates are kept.

3.1.4 Trajectory smoothing

Since the Kalman filter is performed incrementally, the full information of all measurement is included only at the last step. The trajectory smoothing consists of recalculating the track parameters at each measurement point by a backward fitting (smoothing) so that they include the information of all measurements. Thus, the Kalman filter provides a good method in track finding/fitting since it is linear in the measurements, and its backward complement makes use of the full information, thereby providing room for robustness.

3.2 Standalone muon reconstruction

The standalone muon reconstruction starts at the level of the individual chambers in the muon system. The results are track segments in the Drift Tubes and in the Cathode Strip Chambers, and three-dimensional points in the Resistive Plate Chambers. Despite being different, all of them represent a measurement and therefore they are generally referred as reconstructed hits (*RecHits*) and implemented with the same interface. This feature is crucial for the next step of the muon reconstruction (section 3.1).
Based on the Kalman filter technique, the off-line of track reconstruction starts with the estimation of the seed state from track segments, while the on-line starts

from the trajectory parameters estimated in the L1 trigger. The track is then extended using an iterative algorithm which updates the trajectory parameters at each step and, in order to reduce the possible bias from the seed, a pre-filter can be applied before the final filter. Once the hits are fitted and the fake trajectories removed, the remaining tracks are extrapolated to the point of closest approach to the beam line. In order to improve the p_T resolution a beam-spot constraint is applied.

3.2.1 Local reconstruction in DT

The position of hits in single drift cells is estimated from TDC measurements. This is done in two steps: initially, an average value for the drift velocity is used to fit a two-dimensional segment in the superlayer. The unknown bunch crossing that originated the hits is a parameter of the fit, which uses the mean-timer technique ([]). The parameters obtained are then used to determine the correct effective drift velocity, refine the hit position and the fit. In each chamber, the segments reconstructed in the two $r-\phi$ superlayers are then refitted together, and the result is combined with the segment in the $r-z$ superlayer to produce a three-dimensional segment. The direction resolution in the $r-\phi$ plane is about 0.9 mrad. In the $r-z$ (non-bending) plane, it is about 9 to 13 mrad for tracks in $|\eta| < 0.9$.

3.2.2 Local reconstruction in CSC

Each CSC plane measures a point in two dimensions. One coordinate is measured by the wires, which are read out in bunches resulting in a limited precision. The other coordinate is measured by the strips, where the charge distribution of a cluster of three neighbouring strips is fitted to the so-called Gatti function [] to obtain a precise position measurement. The hits in a chamber are used to fit a three-dimensional straight line segment. The direction resolution of the segment varies from 7 to 11 mrad in ϕ and from 50 to 120 mrad in θ for 50 GeV muons.

3.2.3 Local reconstruction in RPC

The hits produced by the RPCs are three-dimensional points. They are obtained by clustering the strips and calculating the centre of gravity of the area covered by the strips in the cluster (i.e. the width of the strips times their full length). Uncertainties are computed assuming that the hit can have happened anywhere in this area with flat probability, e.g. in the simplest case of a rectangular area they are equal to the length of each side divided by $\sqrt{12}$.

3.2.4 Seed generator

The algorithm is based on the DT and CSC segments (sections 3.2.1 and 3.2.2). A pattern of segments in the stations is searched for, using a rough geometrical criteria. Once a pattern of segments has been found (it may also consist of just one segment), the p_T of the seed candidate is estimated using parametrizations of the form:

$$p_T = A - \frac{B}{\Delta\phi} \tag{3.0}$$

For DT seed candidates with segments in MB1 or MB2, $\Delta\phi$ is the bending angle of the segment with respect to the vertex direction. This part of the algorithm assumes the muon has been produced at the interaction point. If segments from both MB1 and MB2 exist, the weighted mean of the estimated p_T s is taken. If the seed candidate only has segments in MB3 and MB4, the difference in bending angle between the segments in the two stations is used to calculate p_T . In the CSC and overlap region, the seed candidates are built with a pair of segments in either the first and second stations or the first and third stations. $\Delta\phi$ is the difference in ϕ position between the two segments. Otherwise, the direction of the highest quality segment is used. Although this algorithm is currently used only for the off-line seeding, it can also be used for very fast muon reconstruction, and could be used in the HLT chain.

3.2.5 Pattern recognition and track reconstruction

In the standard configuration the seed trajectory state parameters are propagated to the innermost compatible muon detector layer and a pre-filter is applied in the inside-out direction. Its main purpose is to refine the seed state before the true filter. The final filter in the outside-in direction is then applied and the trajectory built. The algorithm is flexible enough to perform the reconstruction starting from the outermost layer instead of the innermost. The pre-filter step can optionally be skipped, hence increasing the speed of the reconstruction which could be important for the High Level Trigger. However, the standard reconstruction can already meet the strict HLT speed requirement. The pre-filter and filter are based on the same iterative algorithm used in two different configurations. In both cases it can be subdivided into different sub- steps: search of the next compatible layer and propagation of the track parameters to it, best measurement finding and possibly update of the trajectory parameters with the information from the measurement. The process stops when the outermost (for the pre-filter) or the innermost (for the filter) compatible layer of muon detectors is reached. At each step the track parameters are propagated from one layer of muon detectors to the next. A suitable propagator must precisely take into account material effects like multiple scattering and energy losses due to ionisation and bremsstrahlung in the muon chambers and in the return yoke. In

order to reduce the processing time, the propagator must be fast. The trajectory is extrapolated in sequential steps using helix parametrizations. The required precision is obtained by using smaller steps in regions with larger magnetic field inhomogeneities. Multiple scattering and energy losses in each step are estimated from fast parametrizations, avoiding time-consuming accesses to the detailed material and geometry descriptions. The resulting propagated state contains these effects in its parameters and errors. The best measurement is searched for on a χ^2basis. The χ^2compatibility is examined at the segment level, estimating the incremental χ^2given by the inclusion in the fit of the track segment. In case no matching hits (or segments) are found, the search continues in the next station. For the update of the trajectory parameters the pre-filter and the filter follow two different approaches. As the pre-filter should give only a first estimate of the track parameters, it uses the segment for the fit. The parameters are almost always updated as the χ^2cut imposed at this stage is loose (of the order of one hundred). The final filter instead uses the hits composing the segment with a tighter χ^2cut (of the order of 25) which can reject individual hits. This results in a more refined trajectory state. The RPC measurements are not aggregated in segments, so that for them the only distinction between the pre-filter and the filter is the χ^2 cut. The mechanism for updating the trajectory parameters can be seen as a combination of the predicted trajectory state and the hit in a weighted mean, as the weights attributed to the measurement and to the predicted trajectory state depend on the respective uncertainties. In order to finally accept a trajectory as a muon track, at least two measurements, one of which must be of the DT or CSC type, must be present in the fit. This allows rejection of fake DT/CSC segments due to combinatorics. Moreover the inclusion of the RPC measurements can improve the reconstruction of low momentum muons and those muons which escaped through the inter-space between the wheels (and the DT sectors), leaving hits in only one DT/CSC station. After the fake track suppression, the parameters are extrapolated to the point of closest approach to the beam line. In order to improve the momentum resolution a constraint to the nominal interaction point (IP) is imposed. The error of the IP: 15 μm, 15 μm, and 5.3 cm.

3.3 Track reconstruction in the Tracker

As in the muon system, the reconstruction process starts with the seed finding, but while in the muon system the trajectory is built during the pattern recognition, in the tracker the pattern recognition and the final fit are performed separately. Two different algorithms have been implemented. The first uses two or three consecutive hits, in the pixel and/or in the strip detector, to find the seeds. Based on the Kalman filter technique, the algorithm uses an iterative process to pass from one layer to the next and to perform the pattern recognition.

The principle is very similar to that used in the muon spectrometer alone (Section 3.2.5). The second algorithm, called road search, uses only the silicon strip detector to find the seeds: it takes one hit in the inner layer and one in the outer and considers the possible paths which can connect the two initial hits. The pattern recognition is performed collecting the measurements around the paths. Both the algorithms [51, 52] end with a final fit of the collected hits, followed by the suppression of fake tracks.

3.4 Matching tracker tracks to standalone muon tracks

The first step in reconstructing a global muon track is to identify the silicon tracker track to combine with the standalone muon track. This process of choosing tracker tracks to combine with standalone muon tracks is referred to as track matching. The large multiplicity of tracks in the central tracker necessitates the selection of a subset of tracker tracks that roughly correspond in momentum and position to the standalone muon track. The definition of the *region of interest* [54] (ROI) has a strong impact on the reconstruction efficiency, fake rate, and CPU reconstruction time. The second step is performed by propagating the muon and the selected tracker tracks onto the same plane and looking for the best χ^2 value from the comparison of track parameters. In the case of very poor χ^2 comparison which results in no matches, the matching is subsequently attempted by comparing the track separation in $\eta - \phi$ space. If there is a suitable match between tracker track and standalone muon track, then the hits from the tracker and the standalone muon track are combined in one collection and a final fit is performed over all hits. After the final global fit is made for all standalone track matches in the event, fake tracks are suppressed. The reconstruction of the muons ends with the matching of the global muon track and the energy deposits in the calorimeters.

3.5 High energy muon reconstruction

Muons with energies of several hundred GeV and more, have a high probability of producing electromagnetic showers in the iron of the CMS magnet return yoke. These large energy losses can significantly degrade the performance of the muon track fitter. Two main effects can contribute to this degradation:

- the muon can loose a large fraction of its energy, so that the part of the track following the energy loss should be discarded, being the particles momentum changed.

- the shower can contaminate the muon detectors, causing incorrect trajectory measurements in the local reconstruction algorithms. These measurements in the track fit can lead to incorrect reconstructed momentum values.

To minimize these effects, two different and complementary approaches have been developed. The first one is based on the fit of the hits from the tracker and the first muon station with hits, with the aim of minimizing the effect of a large change in muon momentum after showering. The second strategy, named *Picky muon* reconstruction, consists of a fit of the muon chamber hits selected by an algorithm applying tight cuts for hit compatibility with tracker track trajectory. This approach minimizes the influence of contaminated chambers, while preserving the hits from chambers providing good trajectory measurement, despite containing a shower. These two refits optimized for showering muons are considered along with the standard global muon fit and the fit using only the hits from the inner tracker, and the global goodness-of-fit of each four trajectories is evaluated. Two algorithms have been developed for selecting the best trajectory, basing the decision of the comparison of the goodness-of-fit variables. Known as the ″cocktails ‶algorithm, this was found to perform better than any of the four individual algorithms. The performance comparison between all the approaches is shown in Fig. 3.1

3.6 Tracker muon reconstruction

Standard muon track reconstruction starts from the muon system and combines standalone muon tracks with tracks reconstructed in the inner tracker. This approach naturally identifies the muon tracks in the detector. However, a large fraction of muons with transverse momentum below 6-7 GeV/c (see Fig. 2.16) does not leave enough hits in the muon spectrometer to be reconstructed as standalone muons. Moreover, some muons can escape in the gap between the wheels. A complementary approach consists in considering all silicon tracker tracks and identifying them as muons by looking for compatible signatures in the calorimeters and in the muon system. Muons identified with this method are called Tracker muons [55]. The algorithm for the muon identification of the tracker tracks extrapolates each reconstructed silicon track outward to its most probable location within each detector of interest (ECAL, HCAL, HO, Muon system).

The algorithm collects and stores all the relevant information into a final muon object. Specific muon identification criteria can be developed based on these variables [56]. However, if a global muon is reconstructed using the same silicon tracker track, the global muon fit is stored in the same muon object and the default momentum of the muon in the object is taken from the global muon fit. The momentum of the silicon tracker track fit is still retrievable through the reference to the silicon tracker track which is stored in the muon object.

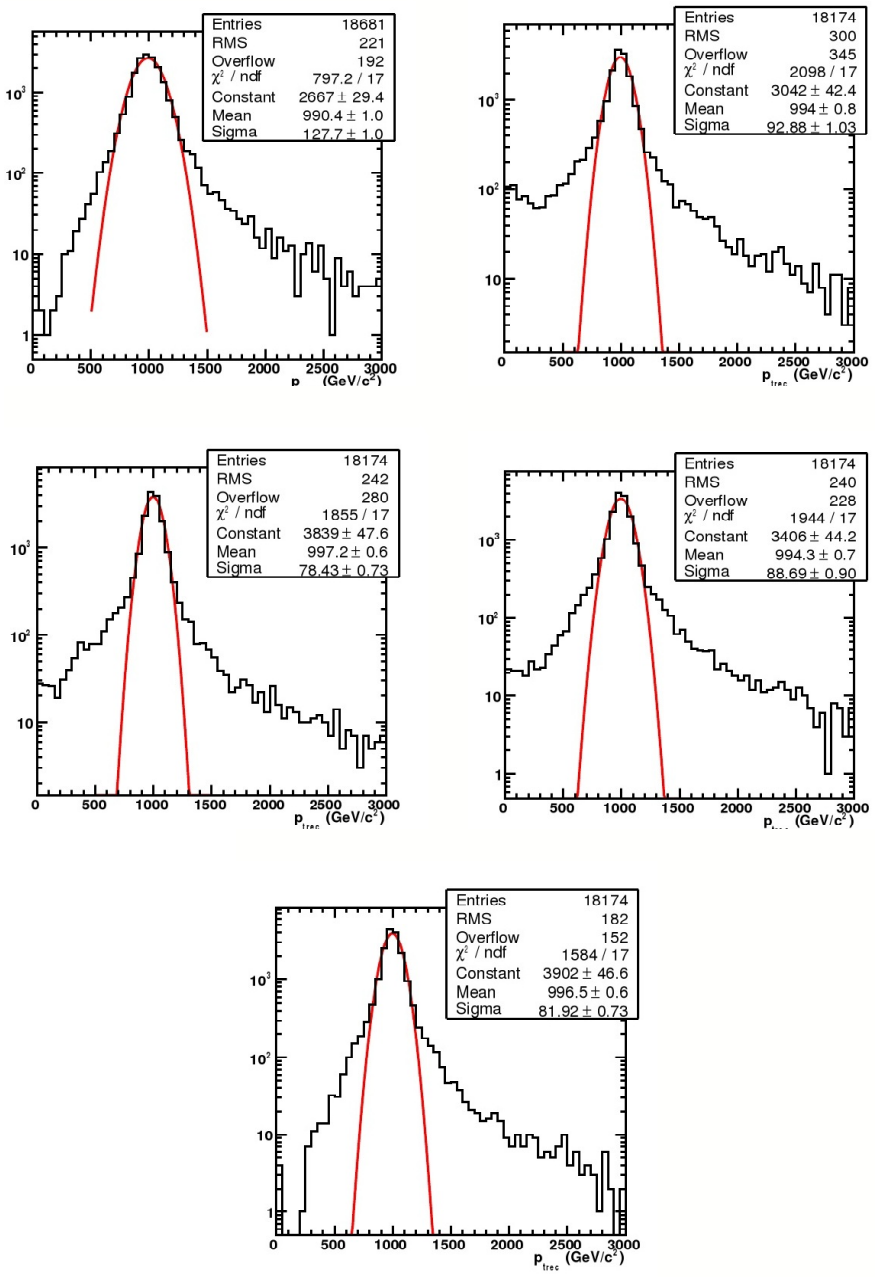

Figure 3.1: *Reconstructed p_T distributions for $p_T = 1TeV/c$ single muons for the different refits. Starting from the top left plot, the distributions show a fit with the Tracker only, followed by the default Global fit, First Muon Station, Picky muon reconstructor, and the cocktails algorithm.*

The muon identification efficiency improves by combining all three different approaches, identifying a muon as global one or standalone one or the tracker one.

3.7 Reconstrution efficiencies

Global, standalone and tracker reconstruction efficiencies as a function of η, ϕ and p_T, are shown in Figures 3.2, and 3.3. The standalone reconstruction efficiency

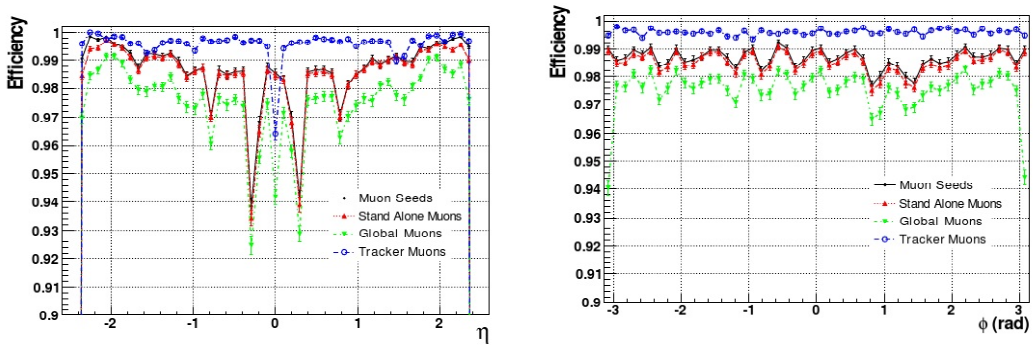

Figure 3.2: *Efficiencies of the different muon reconstruction steps as a function of η, ϕ.*

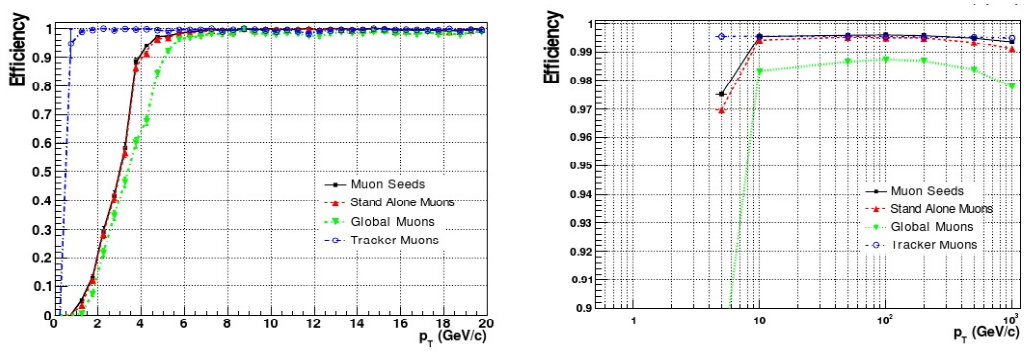

Figure 3.3: *Efficiencies of the different muon reconstruction steps as a function of p_T.*

has a dip at $|\eta| \sim 0.3$ which is due to a discontinuity between the central wheel and the contiguous ones. The $0.8 < |\eta| < 1.2$ region is problematic for the seed-finding algorithm because the DT and CSC segments are used together to

estimate the seed state. Moreover the standalone reconstruction efficiency has a periodic structure in the azimuthal angle due to the DT system segmentation in sectors. There is also a barrel inactive region at $\phi = 1.2$ because of the presence of instrumentation services (chimneys) in two wheels. The overall integrated efficiency, for momenta above 10 GeV/c, is more than 99%. For low momenta the efficiency decreases because a significant fraction of muons looses energy in the material before the muon stations or because of the bending in the magnetic field. At momenta of the order of TeV/c momenta the muon reconstruction efficiency also decreases, even if very slowly, due to the increased bremsstrahlung probability. The inner tracker is less affected by multiple scattering and energy loss than the muon system. Moreover the magnetic field in the tracker volume is homogeneous and almost constant. The integrated efficiency is almost constant for all p_T values and its value is above 99.5%. The efficiency loss at $|\eta| = 0$ is due to the tracker geometry: the tracker is made of two half-barrels joined together, and the junction surface is at $|\eta| = 0$. Also $|\eta| \sim 1.8$ is a problematic region for tracker track reconstruction because of the transition from TID to TOB/TEC subsystems. The global reconstruction efficiency is the product of the tracker, standalone and matching efficiency and for p_T between 10 GeV/c and 1 TeV/c it is larger than 98%. These efficiencies include, the efficiency of the matching of the standalone tracks with the inner tracker tracks: it is of the order of 99.5% and, at the first order, it does not depend on the muon kinematic but it depends mainly from the resolution of the standalone track parameters evaluated at the tracker surface.

3.8 Momentum resolution

The dependence of the p_T resolution on the p_T itself is described by the following formula:

$$\frac{\delta p_T}{p_T} = \frac{0.0136}{\beta BL}\sqrt{\frac{x}{X_0}}\sqrt{\frac{4A_N}{N}} \oplus \frac{\sigma \cdot p_T}{0.3BL^2}\sqrt{4A_N} \tag{3.0}$$

where $\beta = v/c$, x/X_0 is the thickness of the scattering medium in radiation lengths, B is the magnetic field value, L the length of the tracking system, N the number of measurements, σ their individual errors and:

$$A_N = \frac{180N^3}{(N-1)(N+1)(N+2)(N+3)}. \tag{3.0}$$

The first term represents the contribution of multiple scattering and it is constant with respect to p_T. This term is dominant in the standalone muon reconstruction particularly in the barrel and it has the effect to maintain the resolution almost constant up to 100 GeV/c. Above this value, the second term starts to become important. In the tracker the multiple scattering is lower than in the

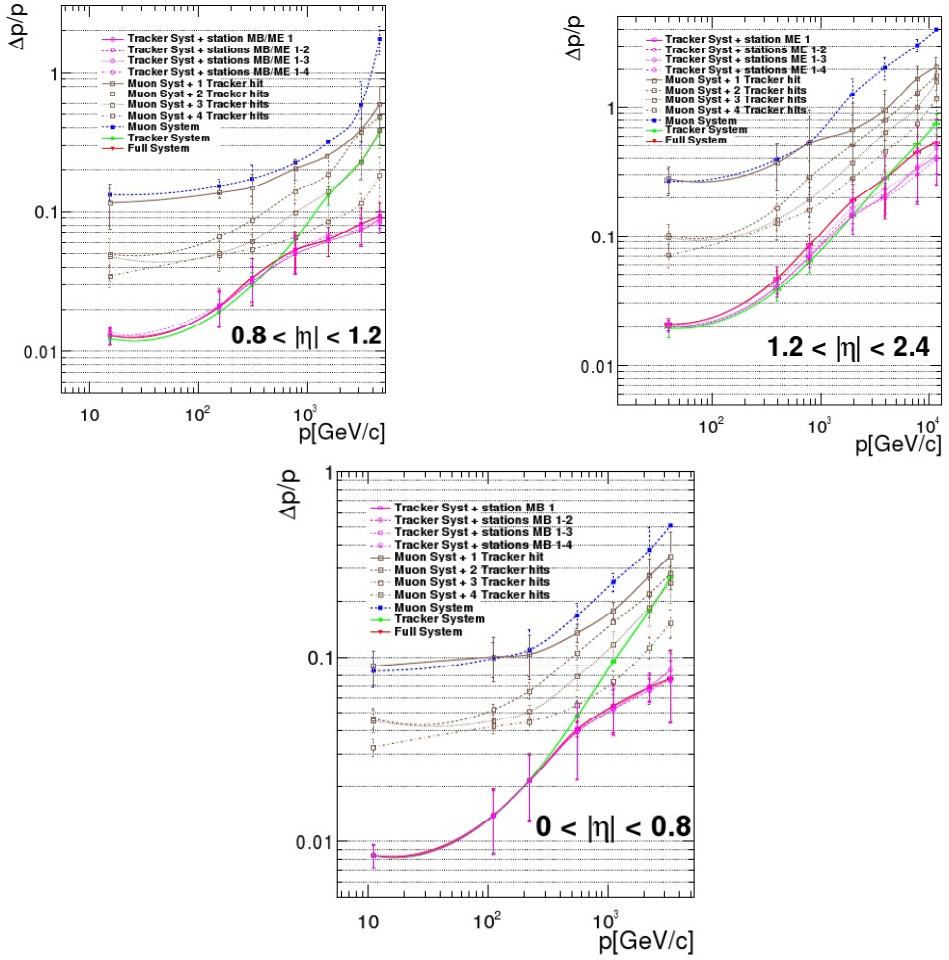

Figure 3.4: *Resolution in different η regions for the different muon reconstruction steps.*

muon system and the dominant term is the one directly related to measurement precision. As the p_T increases, the measurement term becomes more and more important, but can be balanced by a longer path length in the magnetic field (i.e. a larger L): this is accomplished using the tracker and the muon system together. The combination of the information from the tracker and the muon chambers ensures the best p_T estimation both at low and high momenta.
The Fig. 3.4 shows the transferse momentum resolution trend as function of transferse momentum itselfs for barrel, barrel-endcap overlap, and endcap regions.

3.9 Monte Carlo generation of pp collision event

The structure of events produced at high energy colliders is extremely complex, and numeric simulations are necessary to effectively simulate realistic events. Monte Carlo event generators are complex computer programs that subdivide the problem of producing realistic events into a sequence of tasks that can be handled separately with the help of both analytic and numeric computation. Different event generators exist that implement computations at different levels of precision and with different techniques. Typically, the highest precision calculations, that take into account several orders in perturbation theory, are only available for a limited number of processes, thus making it hard to derive predictions on inclusive quantities. On the other hand these quantities can often be described with reasonable precision with programs that implement lower order calculations. A schematic representation of the different components (and calculation steps) that are implemented in event generators is shown in Fig. 3.5.
The production of hadron-hadron collision events is the result of the following chain of calculations:

- The first step is the calculation of cross sections for the selected processes. Cross sections are calculated for a pair of incoming partons (quarks and gluons) extracted from the colliding hadrons.

- The event production starts with two colliding hadrons with given momenta. One parton out of each hadron is selected to enter the scattering process we are interested in. This step is often referred to as hard scattering generation. Final state partons and leptons are produced according to the calculated differential cross sections. Resonances produced in the event are decayed.

- When two partons take part in the scattering process, accelerated colour charges are present, thus bremsstrahlung can occur. This effect is called Initial State Radiation (ISR) and is simulated with the so called Initial State Parton Showers.

- Also the final state partons can produce further radiation, called Final State Radiation (FSR). Such radiation is simulated by the Final State Parton Showers.

- In addition to the partons taking part in the hard interaction, several other parton pairs can interact during a hadron-hadron collision, giving rise to interactions with smaller transferred momentum. These Multiple Parton Interactions (MPI) contribute to the so called underlying structure of the event. Such interactions need to be simulated too if we want to produce realistic events, and ISR and FSR need to be simulated for these collisions too.

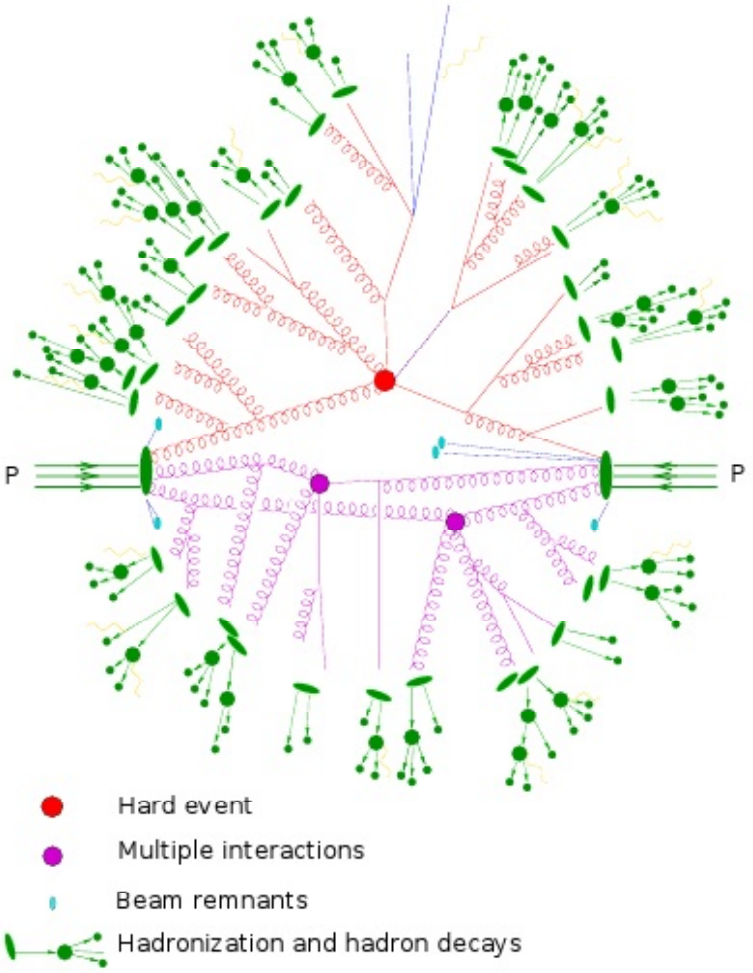

Figure 3.5: *A schematic representation of the generation of an event in a typical event generator. Partons from the two incoming hadrons participate in the hard scattering and in softer multiple interactions. Hadron remnants are treated. Quarks and gluons are turned into hadrons by hadronization and then hadrons decay.*

- Leftovers of the interacting hadrons needs to be simulated to balance the colour charge and for momentum conservation. The beam remnant handling is thus another step in the event generation.
- The calculations described so far are carried out in the perturbative regime, but, as the produced partons move apart from each other, the strong coupling constant gets stronger and stronger and confinement effects take place.

When the coupling constant is strong enough quark-antiquark pairs are produced from the vacuum and the partons turn into hadrons. This generation step is referred to as hadronization.

- Finally, the event generator takes care of decaying τ leptons and B-hadrons. In general particles with very short lifetime are decayed by the generator itself. Those that live enough to reach the detector are left undecayed.

Many generators exist nowadays that can make calculations up to several partons in the final state. Among the general purpose ones there are many tree-level generators: `PYTHIA` [57], `HERWIG` [58], `AlpGen` [59], `SHERPA` [60], `MADGRAPH` [61, 62] are able to make matrix element calculations for a number of processes, and to match the matrix element outcome with parton showers. A few generators which can perform the full Next-to-Leading Order (NLO) calculation with all virtual corrections included are also available for a limited number of processes, `MC@NLO` [63] generator is an example. Both `PYTHIA` and `MC@NLO` generated samples are simulated and reconstructed using the official CMS software package, `CMSSW` [64]. In this analysis I have used only the `PYTHIA` samples, while the `MC@NLO` sample has been used to determine the systematic error, of the $Z \to \mu^+\mu^-$ measurement, related to the Monte Carlo generator choice (see 4.10).

3.10 Digitization and the events reconstruction

After the generation of an event from pp collision, a second step consists on the simulation of the interactions of the generated particles with the detector elements as well as the dead materials. These are interpreted in terms of signal output from the front-end electronics (digis). This procedure is carried out with `GEANT4` [65] package properly interfaced to `CMSSW`.
Trigger and reconstruction algorithms collect the readout digis from the subdetectors to create complex physics objects like tracks, electromagnetic or hadronic showers. Informations from one or more detectors are combined together to correctly identify physics objects like electrons, photons, muons, hadronic showers etc. and to evaluate the related kinematic observables.

3.11 Z reconstruction algorithm

For each event the $Z \to \mu^+\mu^-$ candidates are built from all combinations of pairs of muons (*dimuons*) with opposite charges, detected in the angular acceptance of CMS $|\eta| < 2.4$. Muon candidates are classified according to the type of tracks they are associated to. They can be reconstructed in the inner tracker (tracker track muon), in the muon system (standalone muon), in the full CMS detector (global muon) as explained in the first part of this chapter. Figure 3.6 shows

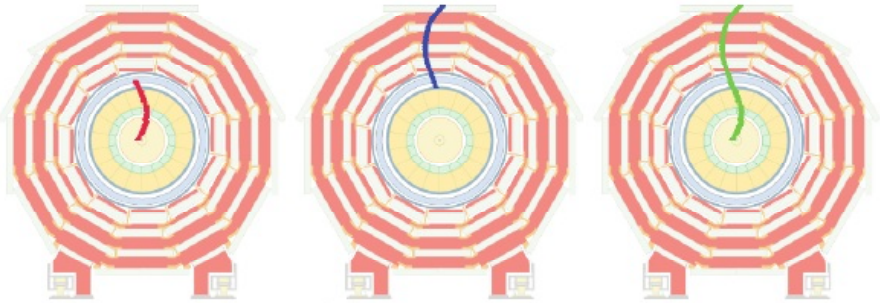

Figure 3.6: *Muon candidates classication: (a) tracker track,(b) standalone track and (c) global muon.*

a schematic image of the three kinds of reconstructed muons.
Therefore, three categories of $Z \rightarrow \mu^+\mu^-$ candidates are built, according to the type of input muons used in the reconstruction [1]:

- two global muons, colled golden candidates;
- a global muon + a standalone muon;
- a global muon + a tracker track muon.

Figure 3.7,showns the number of the reconstructed Z golden candidates per event, taken from the collection $Z \rightarrow \mu^+\mu^-$ Monte Carlo signal events. We can see that:

- In the 98% of cases, the algorithm reconstructs correctly one Z per event;
- In the 5% of cases, the algorithm fails and no Z particles are reconstructed;
- Finally at percent level, the algorithm reconstructs two or more Z candidates per event.

In this case, besides a Z reconstructed correctly, there is one or more fake Z candidates, coming from the random combination of a muons. These fake Z's

[1] In principle we could have a Z category for each of possible type of muons combination, for example two tracker track muons with opposite charge. However in order to minimize the combinatorial background it's required that at least one muon is global.

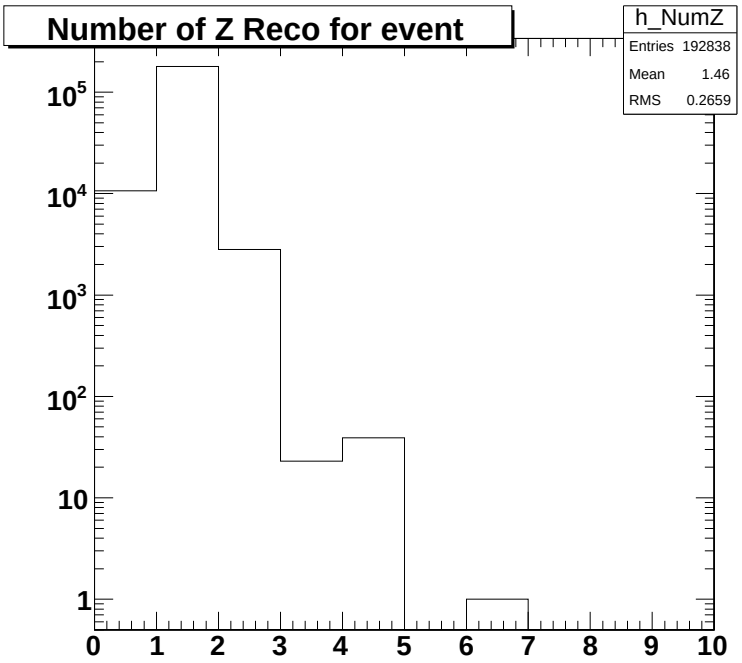

Figure 3.7: *Number of golden Z candidates reconstructed in a $Z \rightarrow \mu^+\mu^-$ signal event.*

cannot be associated [2] to a MC generated Z and forms part of the combinatorial background. In Fig. 3.8 the main kinematic distributions for this combinatorial background are shown; in particular the invariant mass is peaked at low values and decreases rapidly for increasing mass.
The same kinematic distributions (invariant mass, η, p_T, and ϕ) of the generated and reconstructed $Z \rightarrow \mu^+\mu^-$ decays from ″Summer08‟Monte Carlo production[3]

[2]The Monte Carlo truth matching is based on a distance defined in terms of the pseudorapidity η and of the azimuthal angle ϕ. A final state reconstructed particle is associated to a particle from the Monte Carlo generator if $\Delta R < 0.015$ where:

$$\Delta R = \sqrt{(\Delta\eta)^2 + (\Delta\phi)^2} \tag{3.1}$$

and $\Delta\eta$ and $\Delta\phi$ are the differences in pseudorapidity and azimuthal angle between the vertexes of the trajectory of the particles. The Monte Carlo truth matching of a composite object, like a reconstructed $Z \rightarrow \mu^+\mu^-$ is done in two steps:

1. Matching the reconstructed muons coming from Z candidate decays;

[3]The Summer08 production is an official CMS Monte Carlo production made during the summer 2008. It is generated with Pythia generator, simulation and reconstruction chain, assuming a center of mass energy of $\sqrt{s} = 10$ TeV and ideal conditions of the detector.

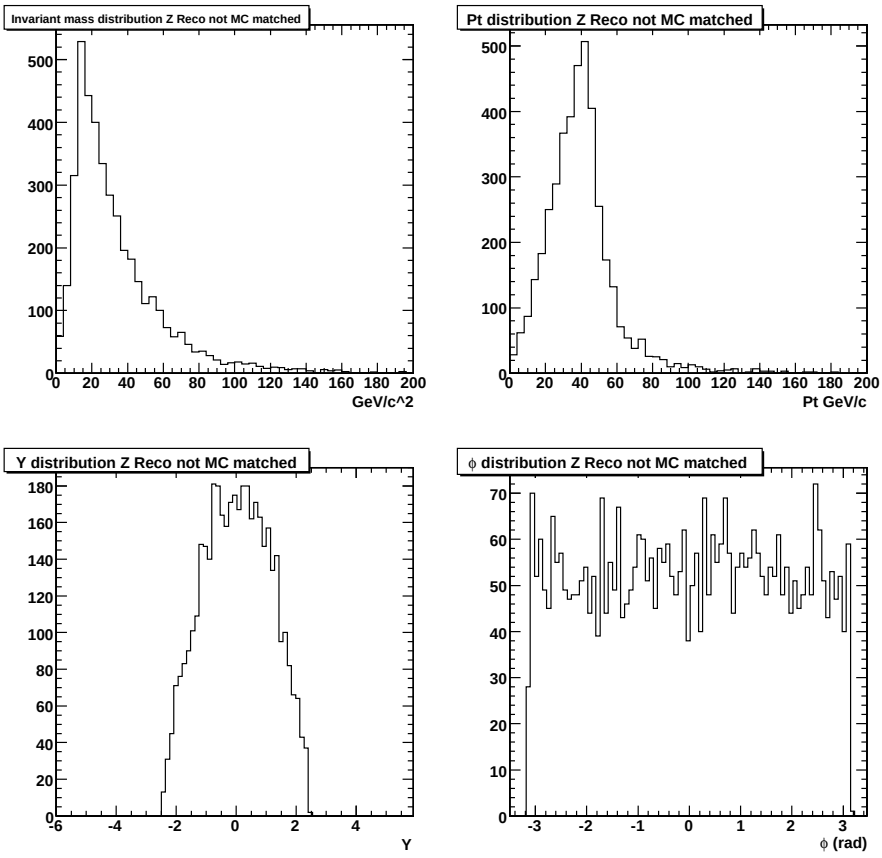

Figure 3.8: *Kinematic distributions of $Z \rightarrow \mu^+\mu^-$ not Monte Carlo matched (combinatorial background). Top Left: Invariant mass distribution; Top Right: p_T distribution; Bottom Left: rapidity (Y) distribution; Botton Right: Azimuthal angle (ϕ) distribution.*

are compared in Figure 3.9.The good agreement beetwen the distributions of the two semples underlines the goodness of Z reconstruction algorithms and in particular of the muons. Most of the Z bosons are produced in forward region. This is related to the Z production mechanism in a pp collision which takes place from the annihilation of a $q\overline{q}$ pair (Fig. 3.10),where $\overline{q}$ necessarily is a sea-quark. Since a valence quark has, on avarage, a momentum greater than sea anti-quark the Z momentum results will have a non-zero longitudinal component (see Fig 3.11).
In figure 3.12 the transverse momentum, pseudorapidity and azimuthal angle distributions of the muons from the $Z \rightarrow \mu^+\mu^-$ candidates are plotted. The isotropy on orthogonal plane to the beam axis is shown by uniform azimuthal distribution, while the η distribution points out that the muons are mainly emit-

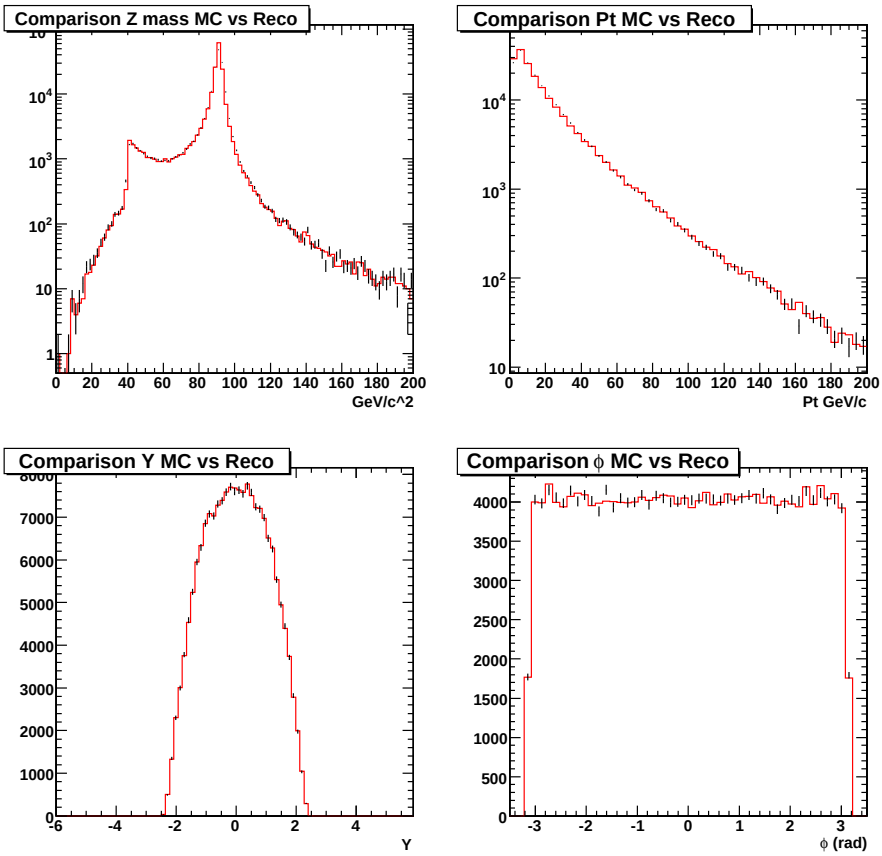

Figure 3.9: *Comparison between the kinematic distributions of generated $Z \rightarrow \mu^+\mu^-$ decays (red points) and reconstructed ones (black points). Top Left: Invariant mass distribution; Top Right: p_T distribution; Bottom Left: rapidity (Y) distribution; Botton Right: Azimuthal angle (ϕ) distribution.*

ted at $\eta = 0$, that is orthogonally to the beam axis. In addition the generator cut for $|\eta| < 2.5$ can be clearly seen. The figure 3.13 shows the p_T resolutions of the global muons,tracker track, and standalone muons coming from $Z \rightarrow \mu^+\mu^-$ decays. We can observe that the p_T resolution of global and tracker track are comparable and it is better than standalone one.

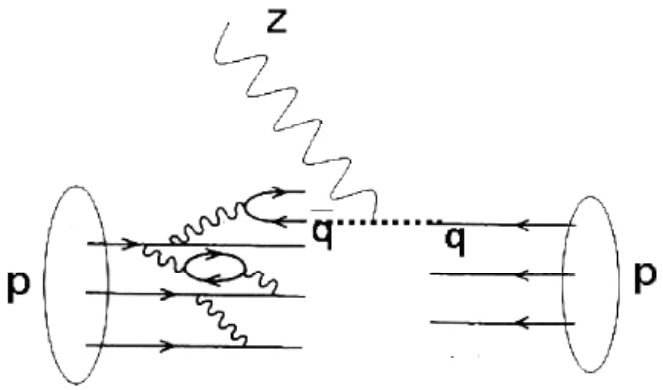

Figure 3.10: *Annihilation of a valence quark and a sea quark into a Z boson. The valence quark momentum is, on average, greater than sea quark one, resulting in a forward directed Z boson.*

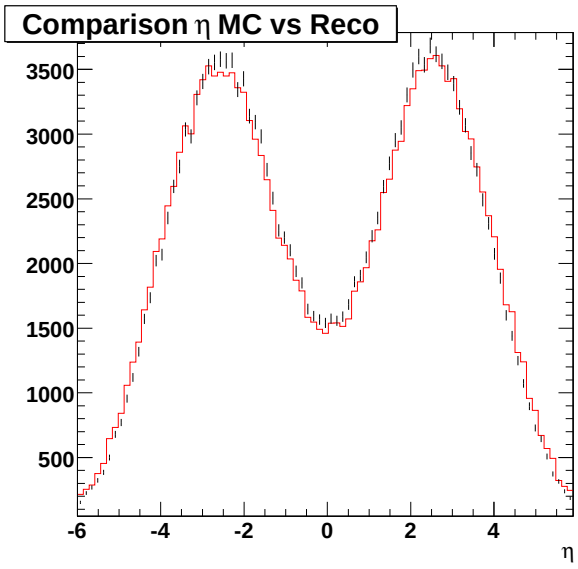

Figure 3.11: *Comparison between pseudorapidity (η) distribution of generated $Z \to \mu^+\mu^-$ decays (red points) and reconstructed ones (black points).*

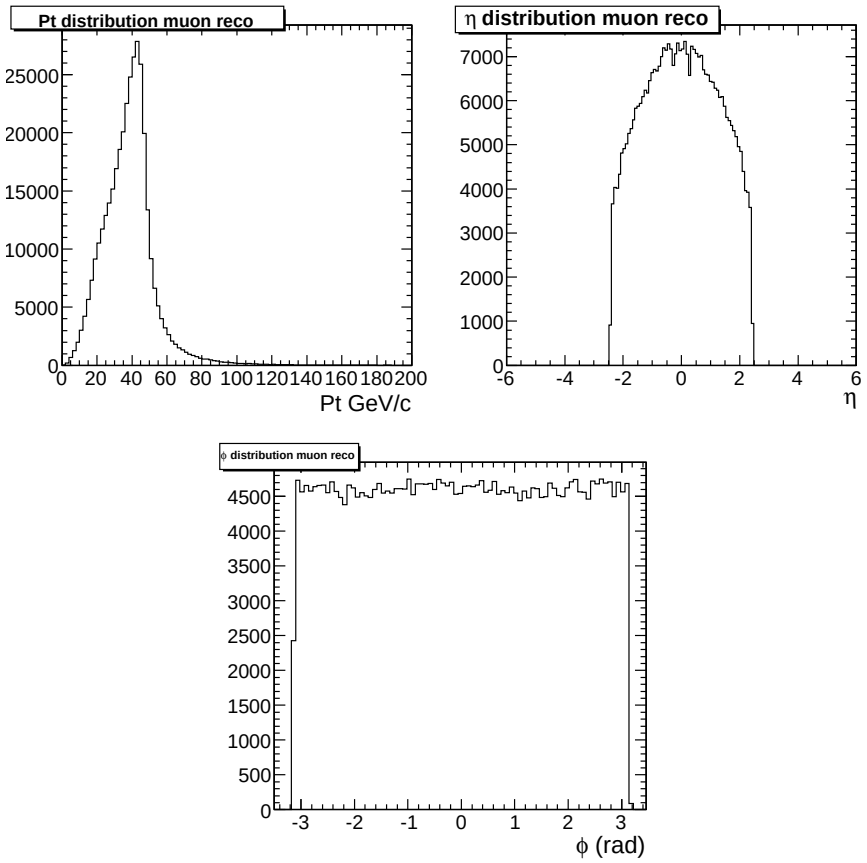

Figure 3.12: *Kinematic distributions of muons coming from reconstructed $Z \rightarrow \mu^+\mu^-$ candidates. Top Left: p_T distribution; Top Right: pseudorapidity (η) distribution; Botton: Azimuthal angle (ϕ) distribution.*

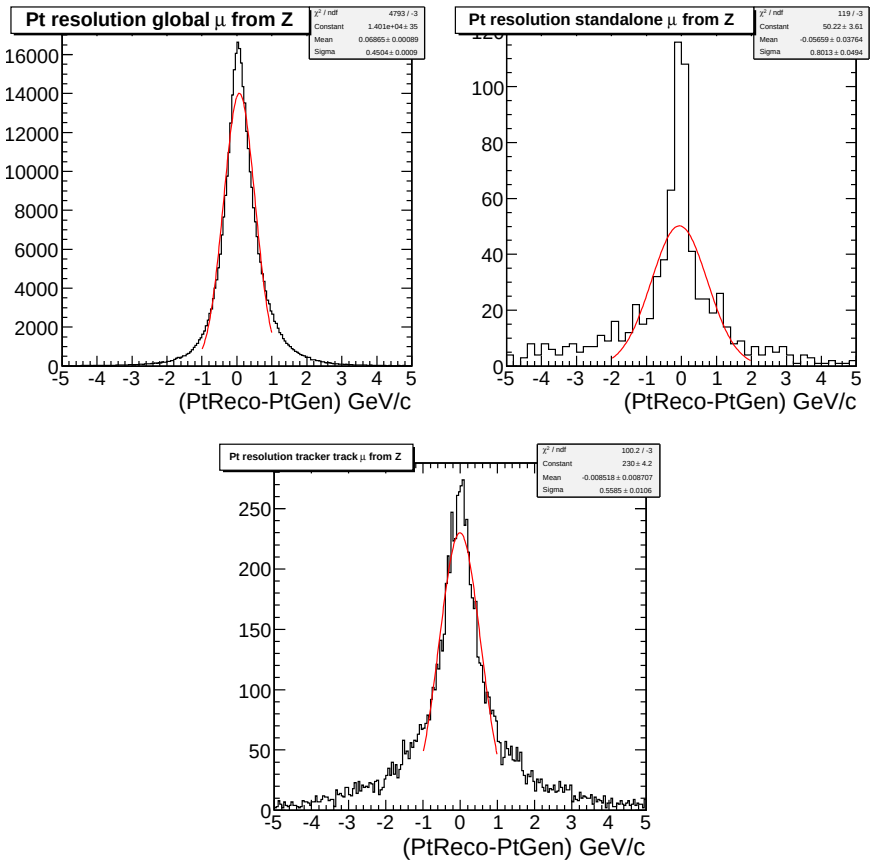

Figure 3.13: *p_T resolution of different kind of muons coming from reconstructed $Z \rightarrow \mu^+\mu^-$ candidates. Top Left: p_T resolution of global muons; Top Right: p_T resolution of standalone muons; Botton: p_T resolution of tracker track muons. For each distribution the gaussian fit (red line) is superimposed.*

Chapter 4

Study of the inclusive process $pp \rightarrow Z + X \rightarrow \mu^+\mu^- + X$ and cross section measurement

The properties of the Z boson have been measured with high precision by several experiments.

During the 1990s LEP and SLC experiments [66, 67, 68, 69, 70] accumulated 17 million and 600 thousand of Z decays, respectively. These data allowed the most precise measurements on Z properties, such as the cross-section ($e^+e^- \rightarrow Z \rightarrow \overline{q}q, l^+l^-$), the mass ($m_Z$), the Z line-shape width (Γ_Z), its couplings to fermions, the forward-backward and polarised asymmetries:

$$m_Z = 91.1875 \pm 0.0021\ GeV/c^2, \tag{4.1}$$

$$\Gamma_Z = 2.4952 \pm 0.0023\ GeV/c^2, \tag{4.2}$$

$$\rho_0 = \frac{{m_W}^2}{{m_Z}^2 \cos^2\theta_W} = 1.0050 \pm 0.0010, \tag{4.3}$$

$$\sin\theta_{eff} = 0.23153 \pm 0.00016. \tag{4.4}$$

These results were compared to the predictions of the SM and found to be in agreement. In addition the inderect measurement of the number of generations of fermions with a light neutrino was determined from the precise measurements of the partial widths (Fig. 4.1),

$$\Gamma_Z = \Gamma_{ee} + \Gamma_{\mu\mu} + \Gamma_{\tau\tau} + \Gamma_{had} + \Gamma_{inv}, \tag{4.4}$$

where

$$\Gamma_{had} = \sum_{q \neq t} \Gamma_{q\bar{q}}, \tag{4.4}$$

and

$$\Gamma_{inv} = N_\nu \Gamma_{\nu\bar{\nu}}. \tag{4.4}$$

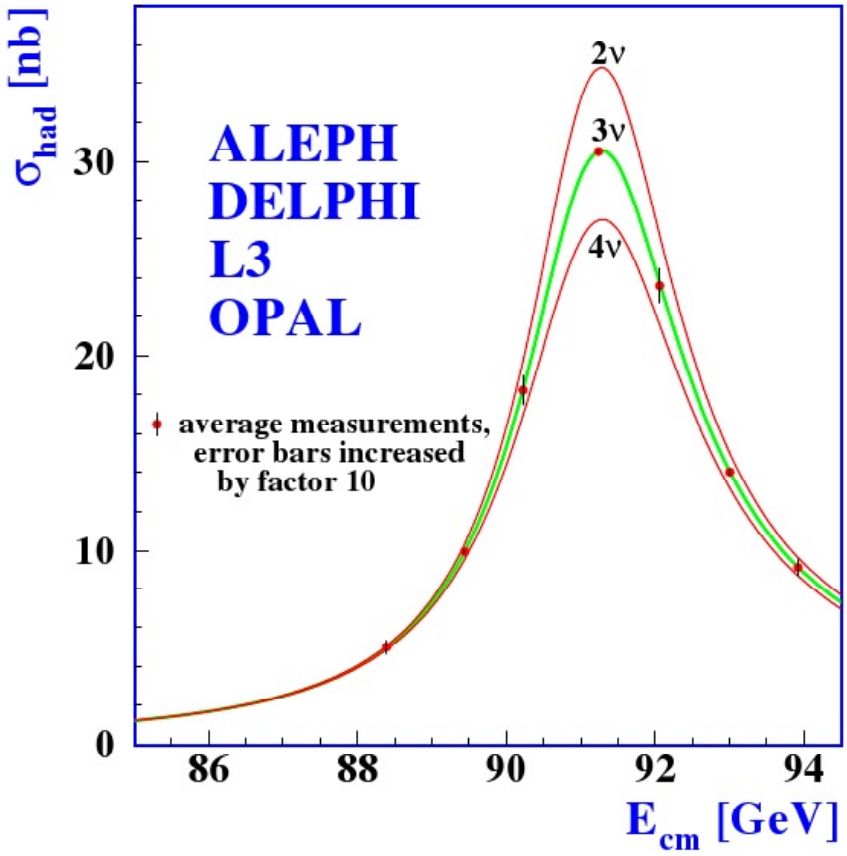

Figure 4.1: *Measurements of the hadron production cross-section around the Z resonance. The curves indicate the predicted cross-section for two, three and four neutrino species with SM couplings and negligible mass.*

The number of light neutrino species is determined to be 2.9840 ± 0.0082, in agreement with the three observed generations of fundamental fermions. Moreover, for the first time, the experimental precision was sufficient to probe the predictions of the SM at the loop level, demonstrating not only that it is a good model at low energies but that, as a quantum field theory, it gives an adequate description of experimental observations up to much higher scales. Through radiative corrections evaluated in the framework of the Standard Model, the Z-pole data was also used to predict the mass of the top quark, $m_t = 173 \pm 13 GeV/c^2$, and the mass of the W boson, $m_W = 80.363 \pm 0.032 GeV/c^2$. These indirect constraints are compared to the direct measurements, providing a stringent test of the Standard Model. Using in addition the direct measurements of m_t and m_W , the mass of the as yet unobserved Standard Model Higgs boson is predicted with a relative uncertainty of about 50% and found to be less than $285 GeV/c^2$ at 95%

confidence level.

At LHC the inclusive process $pp \to Z+X \to l^+l^-$ ($l = e, \mu$), will be one of the first processes to be studied from the very early phase of data-taking, thanks to its relatively large cross section and clear signature. It is relevant to observe that the LHC measurements of Z will be less precise of those at leptonic machine described above. At same time the Z properties but they will be the *Standard Candle* for many LHC measurements. Indeed they will be essential for the calibration of the detector and to establish its performances. Events also constitute the main source of background for many searches beyond the Standard Model to be carried out at the LHC, and therefore a precise understanding of these processes is critical before any discovery can be made. Their inclusive study represents a first step in the detailed understanding of reference physics processes at the LHC: transverse momentum spectra, associated jet activity, beyond-leading-order effects and parton density functions.

In this thesis [71] a study of the inclusive cross section of the process $pp \to Z + X \to \mu^+\mu^- + X$ is presented. The method to extract the cross section is based on a simultaneous fit of the yield of $Z \to \mu^+\mu^-$ events, the average reconstruction muon efficiencies in the tracker and in the muon detector, the High Level Trigger efficiency, as well as the efficiency of the cut applied to select isolated muons without any estimate of those efficiencies from Monte Carlo (MC). The extracted Z yield has to be just corrected for the geometrical acceptance and for the integrated luminosity in order to measure the cross section.

4.1 Data samples

We have used the following Summer08 MC samples generated with the Pythia generator, simulation and reconstruction chain, assuming a center of mass energy of $\sqrt{s} = 10$ TeV and ideal conditions of the detector:

- $pp \to Z/\gamma^* X \to \mu^+\mu^- X$, $M_{\mu^+\mu^-} > 20 GeV/c^2$;
- $pp \to W^{\pm} X \to \mu^{\pm}\nu_{\mu} X$;
- QCD jets events ($\widehat{p_T} > 20$GeV/c) containing at least one muon with $p_T > 15$GeV/c (*InclusiveMuPT15*);
- $t\bar{t}$ (*TauolaTTbar*).
- $pp \to Z/\gamma^* X \to \tau^+\tau^- X$;

The number of events for each sample, the product of the LO cross section (σ) times the generator filter efficiency (ϵ_{filter}), and the equivalent integrated luminosity ($\int L\text{dt}$) are shown in Table 4.1. More details about the analyzed samples can be found on the EWK TWiki page [72, 73].

Sample	Events	$\sigma \times \epsilon_{\text{filter}}$ (pb)	$\int L\text{dt}$ (pb^{-1})
$pp \to ZX \to \mu^+\mu^- X$	1,062,500	627	1694.34
$pp \to W^{\pm}X \to \mu^{\pm}\nu_{\mu}X$	1,091,841	8198	133.17
QCD jets, muon $p_T > 15$ GeV/c	5,479,643	121,675	45
$t\bar{t}$	147,000	241.7	608
$pp \to ZX \to \tau^+\tau^- X$	1,073,000	1086	133

Table 4.1: *Analyzed data samples.*

The analyzed samples are first processed through a preselection phase (″skimming ″) where HLT requirements are applied. At skimming level, it is also required the presence of at least two reconstructed muons or one muon plus one tracker track. The dimuon skims were run at the Tier-2 site of Legnaro. After that, in order to further reduce the data samples, a secondary skim (sub-skim) was run and the output was published at Naples Tier-3 site for local analysis.

4.2 Method description

The number of produced $Z \to \mu^+\mu^-$ events in a collected data sample can be determined from the number of observed events with two reconstructed isolated global muons having an invariant mass within a range centered at the Z mass peak, corrected by the efficiency of reconstructing the two muons, the HLT selection efficiency, and the efficiency of the isolation cut.

We want to determine both the yield of produced Z events, corrected by the efficiency effects, and the involved efficiency terms from data.

We consider, as muon candidates, global muons, stand alone muons and tracks. We build $Z \to \mu^+\mu^-$ candidates as pairs of muon candidates, and we define the following statistically independent categories of events with at least one reconstructed $Z \to \mu^+\mu^-$ candidates:

- $Z_{\mu\mu}$: a pair of isolated global muons. This category can be further split into two independent samples:
  - $Z_{\mu\mu}^{\text{2HLT}}$: a pair of isolated global muons, both matched to HLT trigger primitives
  - $Z_{\mu\mu}^{\text{1HLT}}$: a pair of isolated global muons only one matched to an HLT trigger primitive
- $Z_{\mu s}$: a pair of one isolated global muon and one isolated standalone muon; the global muon must be matched to HLT trigger primitives
- $Z_{\mu t}$: a pair of one isolated global muon and one isolated tracker track; the global muon must be matched to HLT trigger primitives

- $Z_{\mu\mu}^{\text{non iso}}$: a pair of global muons, where at least one is non isolated; at least one muon must be matched to HLT trigger primitives.

The four categories are explicitly forced to be mutually exclusive in our event selection: if one event falls in the first category it is excluded from the second; if it does not fall in the first category and falls in the second, it is excluded from the third, and so on, in order to have non-overlapping, hence statistically independent, event samples. In case of multiple di-muon candidates for an event falling in one of the categories, all the possible combinations are added to the mass spectrum.

We introduce the differential event yields for signal plus background with the following Probability Density Functions (PDF) for each of the four categories:

$$\frac{\mathrm{dN}_{\mu\mu}}{\mathrm{dm}} = f_{\mu\mu}(m) = N_{\mu\mu} f_{peak}(m) \tag{4.5}$$

$$\frac{\mathrm{dN}_{\mu\mu}^{\mathrm{2HLT}}}{\mathrm{dm}} = f_{\mu\mu}(m)^{\mathrm{2HLT}} = N_{\mu\mu}^{\mathrm{2HLT}} f_{peak}(m) \tag{4.6}$$

$$\frac{\mathrm{dN}_{\mu\mu}^{\mathrm{1HLT}}}{\mathrm{dm}} = f_{\mu\mu}(m)^{\mathrm{1HLT}} = N_{\mu\mu}^{\mathrm{1HLT}} f_{peak}(m) \tag{4.7}$$

$$\frac{\mathrm{dN}_{\mu\mathrm{s}}}{\mathrm{dm}} = f_{\mu s}(m) = N_{\mu s} f_{peak}^{s}(m) + b_{\mu s}(m) \tag{4.8}$$

$$\frac{\mathrm{dN}_{\mu\mathrm{t}}}{\mathrm{dm}} = f_{\mu t}(m) = N_{\mu t} f_{peak}(m) + b_{\mu t}(m) \tag{4.9}$$

$$\frac{\mathrm{dN}_{\mu\mu}^{\text{non iso}}}{\mathrm{dm}} = f_{\mu\mu}^{\text{non iso}}(m) = N_{\mu\mu}^{\text{non iso}} f_{peak}(m) + b_{\mu\mu}^{\text{non iso}}(m) \tag{4.10}$$

$$\tag{4.11}$$

Above, the total signal yield in the different categories is factorized in the terms $N_{\mu\mu} = N_{\mu\mu}^{\mathrm{2HLT}} + N_{\mu\mu}^{\mathrm{1HLT}}$, $N_{\mu s}$, $N_{\mu t}$ and $N_{\mu\mu}^{\text{non iso}}$, so that the functions $f_{peak}(m)$ and $f_{peak}^{s}(m)$ are normalized to the unity. We have assumed, according to our Monte Carlo estimates, that the background in the samples with two isolated global muons is negligible: we expect $\approx 0.1\%$ of background from non-Z processes, and 0.030% from combinatorial background in Z events producing fake di-muon combinations.

The signal yield in the four categories can be further rewritten in terms of the number of produced $Z \to \mu^+\mu^-$ events, $N_{Z\to\mu^+\mu^-}$, and average efficiencies for muon reconstruction in the tracker (ϵ_{trk}), in the muon detector as standalone tracks (ϵ_{sa}), the average efficiency of the isolation cut (ϵ_{iso}), and the average HLT efficiency (ϵ_{HLT}):

$$
\begin{aligned}
N_{\mu\mu}^{\rm 2HLT} &= N_{Z\to\mu^+\mu^-}\epsilon_{\rm HLT}^2\epsilon_{\rm iso}^2\epsilon_{trk}^2\epsilon_{sa}^2 && (4.12)\\
N_{\mu\mu}^{\rm 1HLT} &= 2N_{Z\to\mu^+\mu^-}\epsilon_{\rm HLT}(1-\epsilon_{\rm HLT})\epsilon_{\rm iso}^2\epsilon_{trk}^2\epsilon_{sa}^2 && (4.13)\\
N_{\mu s} &= 2N_{Z\to\mu^+\mu^-}\epsilon_{\rm HLT}\epsilon_{\rm iso}^2\epsilon_{trk}(1-\epsilon_{trk})\epsilon_{sa}^2 && (4.14)\\
N_{\mu t} &= 2N_{Z\to\mu^+\mu^-}\epsilon_{\rm HLT}\epsilon_{\rm iso}^2\epsilon_{trk}^2\epsilon_{sa}(1-\epsilon_{sa}) && (4.15)\\
N_{\mu\mu}^{\rm non\,iso} &= N_{Z\to\mu^+\mu^-}(1-(1-\epsilon_{\rm HLT})^2)(1-\epsilon_{\rm iso}^2)\epsilon_{trk}^2\epsilon_{sa}^2 && (4.16)
\end{aligned}
$$

This factorization is done neglecting the average correlation of the efficiency different terms. This assumption will be justified and discussed in more details in Section 4.7.

With the assumption that the peak distribution is identical in the categories $Z_{\mu\mu}$, $Z_{\mu t}$ and $Z_{\mu\mu}^{\rm non\,iso}$, and neglecting the background in the $Z_{\mu\mu}$ category, we take as distribution for $f_{peak}(m)$ the normalized histogram of the di-muon invariant mass in the $Z_{\mu\mu}$ category. We have rebinned the distribution in order to match the bin width in the $Z_{\mu t}$ and $Z_{\mu\mu}^{\rm non\,iso}$ categories, which is an integer multiple of the $Z_{\mu\mu}$ one. In Fig. 4.2 and 4.3 we show the level of agreement of the invariant mass distribution for $Z_{\mu\mu}$ candidates selected in signal events with the distributions for $Z_{\mu t}$ and $Z_{\mu\mu}^{\rm non\,iso}$ candidates.

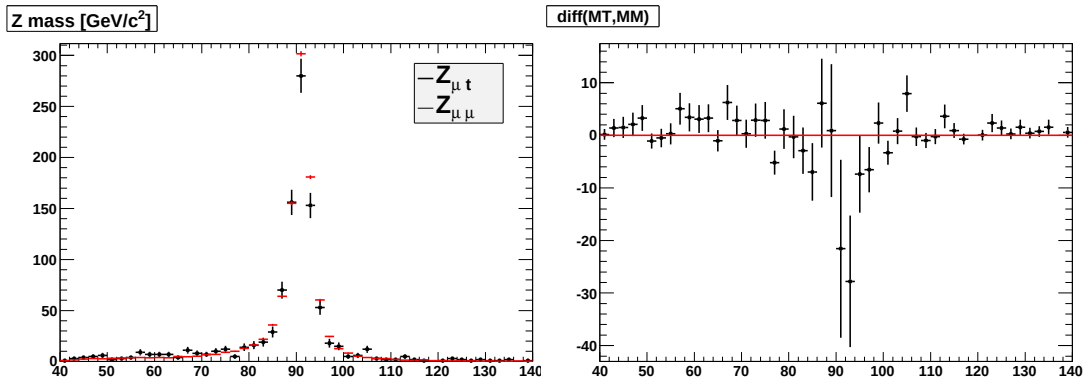

Figure 4.2: *Left: invariant mass (GeV/c^2) distribution for selected $Z_{\mu\mu}$ (red points) and $Z_{\mu t}$ (black points) candidates in signal events. The $Z_{\mu\mu}$ distribution is normalized in order to have the same number of events as the $Z_{\mu t}$ sample. Right: difference between the $Z_{\mu\mu}$ and $Z_{\mu t}$ distributions.*

We have also assumed that the isolation efficiency is identical for global muons, tracks and standalone muons. For the latter, in particular, the worse direction resolution may produce, in principle, a slightly different isolation efficiency. We measured on the Monte Carlo signal sample that the difference in isolation efficiency is very small, and compatible with zero within errors:

$$\epsilon_{\rm iso}^{\rm s.a.} - \epsilon_{\rm iso}^{\rm glob.} = 0.007 \pm 0.057\% \ .$$

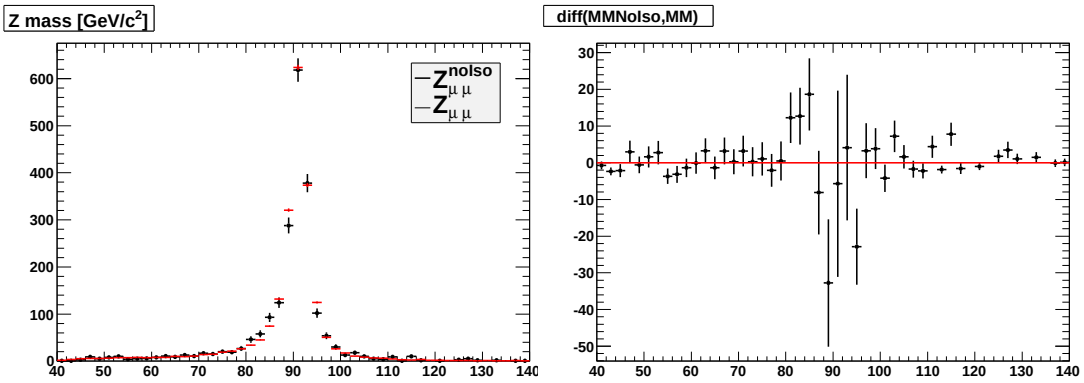

Figure 4.3: *Left: invariant mass (GeV/c^2) distribution for selected $Z_{\mu\mu}$ (red points) and $Z_{\mu\mu}^{\text{non iso}}$ (black points) candidates in signal events. The $Z_{\mu\mu}$ distribution is normalized in order to have the same number of events as the $Z_{\mu\mu}^{\text{non iso}}$ sample. Right: difference between the $Z_{\mu\mu}$ and $Z_{\mu\mu}^{\text{non iso}}$ distributions.*

In order to determine from data a model for the PDF of the peak function for the $Z_{\mu s}$ category, $f_{peak}^{s}(m)$, we consider the $Z_{\mu\mu}$ candidates, and for one of the muons we take the momentum measured from the muon detector track fit only, in order to mimic a standalone muon. We avoid to put the same event twice in the histogram, by chosing alternatively the first (second) muon for even (odd) events respectively. Figure 4.4 compares the invariant mass distribution of the selected $Z_{\mu s}$ candidates with the shape obtained from $Z_{\mu\mu}$ candidates.

Background functions are modeled as products of exponential terms with polynomials of different order for the three samples for which the background is not neglected:

$$b_{\mu t}(m) = N_{\mu t}^{b}(1 + a_1 m + a_2 m^2)e^{-\alpha m} \quad (4.17)$$

$$b_{\mu\mu}^{\text{non iso}}(m) = N_{\mu\mu}^{b\ \text{non iso}}(1 + b_1 m)e^{-\beta m} \quad (4.18)$$

$$b_{\mu s}(m) = N_{\mu s}^{b} e^{-\gamma m} \quad (4.19)$$

The unknown best fit parameters are obtained by minimizing the following global χ^2:

$$\chi^2 = \frac{(N_{\mu\mu}^{2\text{HLT}} - N_{Z\to\mu^+\mu^-}\epsilon_{\text{HLT}}^2\epsilon_{\text{iso}}^2\epsilon_{trk}^2\epsilon_{sa}^2)^2}{N_{\mu\mu}^{2\text{HLT}}} + \frac{(N_{\mu\mu}^{1\text{HLT}} - 2N_{Z\to\mu^+\mu^-}\epsilon_{\text{HLT}}(1-\epsilon_{\text{HLT}})\epsilon_{\text{iso}}^2\epsilon_{trk}^2\epsilon_{sa}^2)^2}{N_{\mu\mu}^{1\text{HLT}}} + \chi_{\mu s}^2 + \chi_{\mu t}^2 + \chi_{\mu\mu}^{\text{non iso }2},$$

where $\chi_{\mu s}^2$, $\chi_{\mu t}^2$ and $\chi_{\mu\mu}^{\text{non iso }2}$ are the χ^2 of the di-muon mass binned histograms

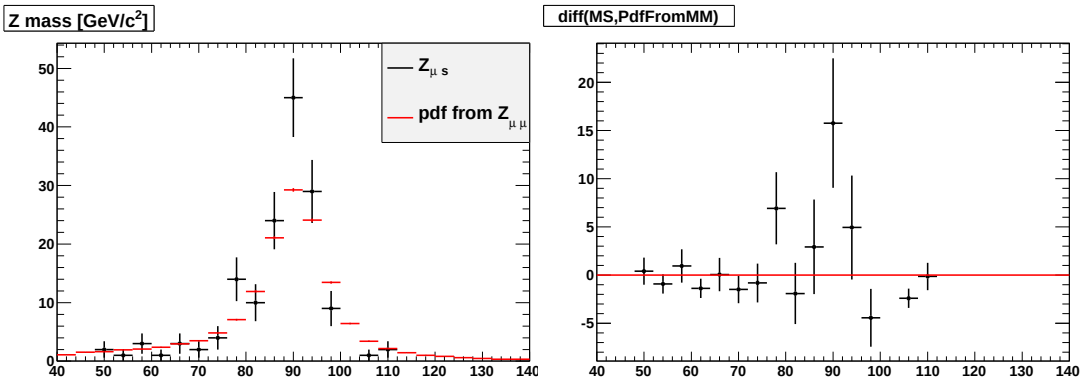

Figure 4.4: *Left: invariant mass (GeV/c^2) distribution for selected $Z_{\mu s}$ candidates in signal events (black points) superimposed to the pdf (red points) determined from $Z_{\mu\mu}$ candidates by using, for one of the muons in the pair, the momentum of the associated standalone muon. Right: difference between the $Z_{\mu s}$ and PDF determined from $Z_{\mu\mu}$ distributions.*

for the three categories $Z_{\mu s}$, $Z_{\mu t}$, and $Z_{\mu\mu}^{\text{non iso}}$. We perform the fit in the range $60 < m < 120$ GeV/c^2.

In the scenario of the first data-taking runs, the sample $Z_{\mu s}$, which has the lowest statistics, could be difficoult to fit with a global binned χ^2 approach. In that case an Unbinned Maximum Likelihood fit for the $Z_{\mu s}$ category can be more satisfactory. It can be performed simultaneously with the binned χ^2 from the other samples, by minimizing the following Negative-Log-Likelihood function:

$$\begin{aligned} -2\ln L \;=\; & \frac{(N_{\mu\mu}^{\text{2HLT}} - N_{Z\to\mu^+\mu^-}\epsilon_{\text{HLT}}^2\epsilon_{\text{iso}}^2\epsilon_{trk}^2\epsilon_{sa}^2)^2}{N_{\mu\mu}^{\text{2HLT}}} + \\ & \frac{(N_{\mu\mu}^{\text{1HLT}} - 2N_{Z\to\mu^+\mu^-}\epsilon_{\text{HLT}}(1-\epsilon_{\text{HLT}})\epsilon_{\text{iso}}^2\epsilon_{trk}^2\epsilon_{sa}^2)^2}{N_{\mu\mu}^{\text{1HLT}}} + \\ & \chi_{\mu t}^2 + \chi_{\mu\mu}^{\text{non iso }2} - 2\ln L_{\mu s}. \end{aligned}$$

4.3 Event selection

Events are required to satisfy the single non-isolated muon trigger with $p_T > 15 GeV/c^2$. Muons used for Z reconstruction are checked for matching with an HLT primitive (see Sect. 4.2 for the HLT matching requirement used in the different samples of Z candidates).

We require that both muon candidates, either global or standalone muons, or tracker tracks, must satisfy:

$$p_T > 20 \text{ GeV/c} ,$$

$$|\eta| < 2 \ .$$

We define as isolation variable the sum of the transverse momenta of all tracks within a cone of radius $\Delta R = \sqrt{\Delta\phi^2 + \Delta\eta^2} = 0.3$ having a transverse momentum larger than 1.5 GeV/c:

$$I_{trk} = \sum_{\substack{0.015<\Delta R<0.3 \\ p_T^{(i)}>1.5 \text{ GeV/c} \\ i=1,\ldots,n}} p_T^{(i)} \ . \tag{4.13}$$

We require:

$$I_{trk} < 3 \text{ GeV/c} \ .$$

Figures 4.5 to 4.9 show the invariant mass distributions of the selected Z candidates for each category considered in the analysis. The plots refer to an input data sample of signal and background events corresponding to an equivalent integrated luminosity of $\int L\mathrm{d}t = 45$ pb^{-1} (where we have used all the QCD MC background statistics available). Table 4.2 reports the number of selected candidates for signal and background in the $[60 - 120]$ GeV/c^2 mass range.

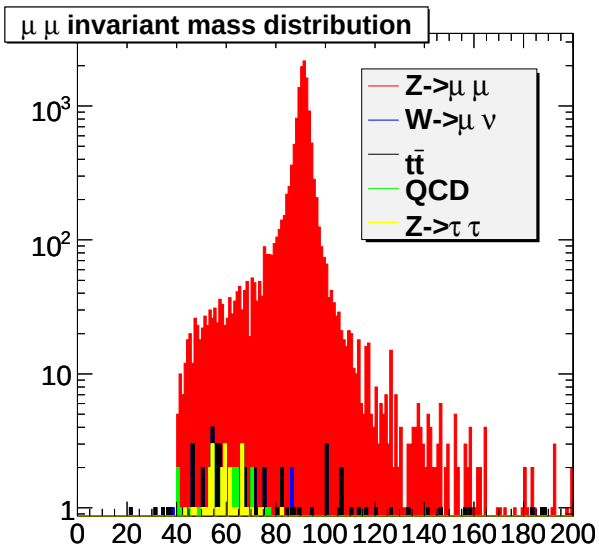

Figure 4.5: *Invariant mass (GeV/c^2) distribution of $Z_{\mu\mu}^{\mathrm{2HLT}}$ candidates for signal and background events corresponding to an equivalent luminosity of 45 pb^{-1}.*

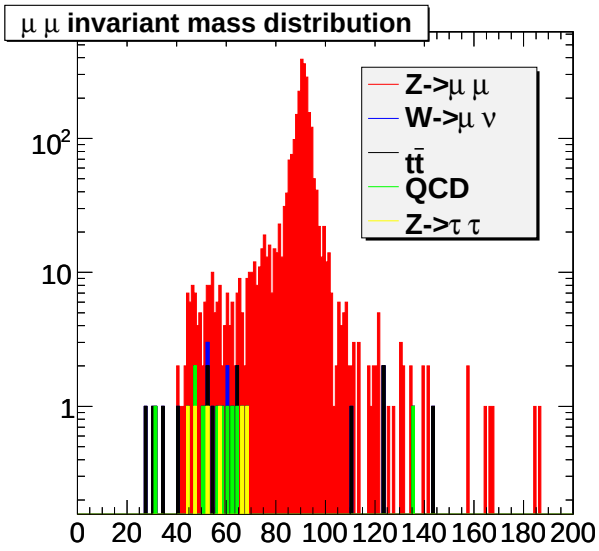

Figure 4.6: *Invariant mass (GeV/c^2) distribution of $Z_{\mu\mu}^{\rm 1HLT}$ candidates for signal and background events corresponding to an equivalent luminosity of 45 pb^{-1}.*

4.4 Fit results

We have performed the fit on the 45 pb^{-1} signal + background data sample. We neglected the background in the $Z_{\mu\mu}^{\rm 2HLT}$, $Z_{\mu\mu}^{\rm 1HLT}$, and $Z_{\mu s}$. Indeed, see table 4.2, the background entries, in the fit region, for the first two samples are of the order of per mil, while for $Z_{\mu s}$ are negligible due to low statistic. Figures 4.10-4.12 show the fit result superimposed to the histograms for the $Z_{\mu s}$, $Z_{\mu t}$, and $Z_{\mu\mu}^{\rm non\,iso}$ samples. Table 4.3 reports the yield and efficiencies determined from the fit. The MC truth values of the average efficiencies, obtained from a sample of signal events, also reported in the table (see Sect. 4.6), and as we can see they are in agreement into a σ with the fit results.

We have also considered other samples with different statistics of signal and background events, in order to study the performance of the fit in different luminosity scenarios and the stability of fit results. In particular, we studied the cases of an integrated luminosity of 5, 10, and 133 pb^{-1} and report the fit results in the table 4.4.

In Figures 4.13, 4.14, and 4.15 we plot the main fit parameters for the various considered integrated luminosity. In Figure 4.15, the fitted cross section has been normalized to the value obtained at the highest luminosity. The fit values are stable and the efficiencies in agreement with the MC truth average values within about 1 to 1.5 σ. At 5 pb^{-1}, the fit results start to show larger error and an initial

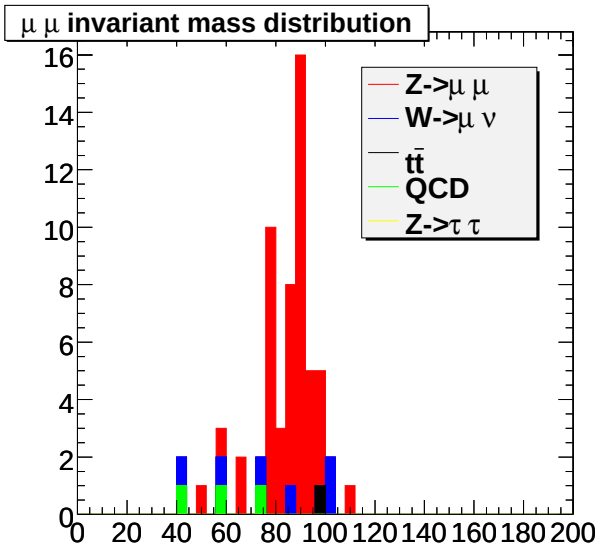

Figure 4.7: *Invariant mass (GeV/c^2) distribution of $Z_{\mu s}$ candidates for signal and background events corresponding to an equivalent luminosity of 45 pb^{-1}.*

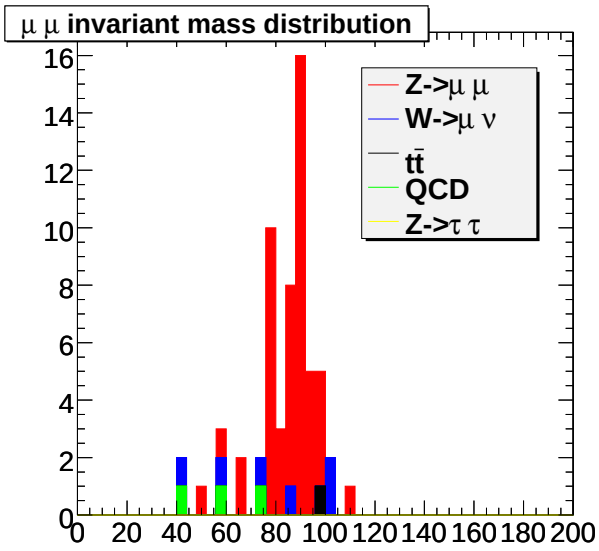

Figure 4.8: *Invariant mass (GeV/c^2) distribution of $Z_{\mu t}$ candidates for signal and background events corresponding to an equivalent luminosity of 45 pb^{-1}.*

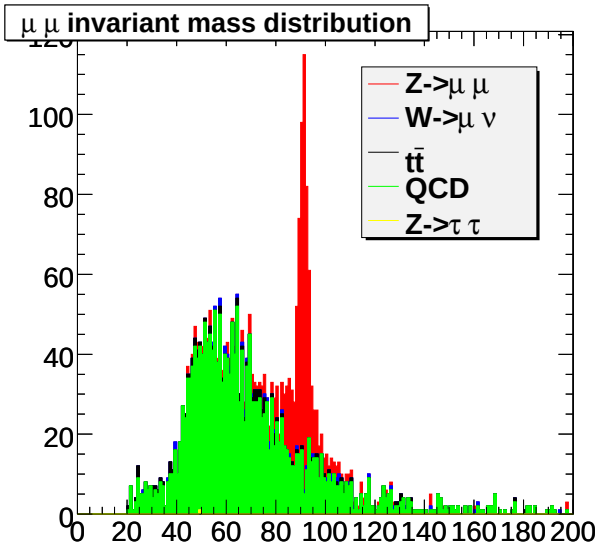

Figure 4.9: *Invariant mass (GeV/c^2) distribution of $Z_{\mu\mu}^{\text{non iso}}$ candidates for signal and background events corresponding to an equivalent luminosity of 45 pb^{-1}.*

MC sample	$Z_{\mu\mu}$	$Z_{\mu s}$	$Z_{\mu t}$	$Z_{\mu\mu}^{\text{non iso}}$
$Z \rightarrow \mu^+\mu^-$	15870 ± 130	49 ± 7	320 ± 20	640 ± 30
$W^{\pm} \rightarrow \mu^{\pm}\nu_{\mu}$	2 ± 1	4 ± 2	320 ± 20	34 ± 6
$t\bar{t}$	24 ± 5	1 ± 1	90 ± 9	40 ± 6
QCD	9 ± 3	1 ± 1	330 ± 20	1090 ± 30
$Z \rightarrow \tau^+\tau^-$	19 ± 4	No events	69 ± 8	No events

Table 4.2: *Number of candidates in each category after the selection with an invariant mass in the range [60-120] GeV/c^2. Here $Z_{\mu\mu} = Z_{\mu\mu}^{\text{1HLT}} + Z_{\mu\mu}^{\text{2HLT}}$. The separate contributions from signal and background processes are shown. An integrated luminosity of 45 pb^{-1} is assumed.*

$\int L\mathrm{dt} = 45\mathrm{pb}^{-1}$	fit results	MC-truth efficiencies
ϵ_{HLT}	0.9161 ± 0.0017	0.917 ± 0.002
ϵ_{iso}	0.9816 ± 0.0012	0.9785 ± 0.0009
ϵ_{sa}	0.9899 ± 0.0008	0.9907 ± 0.0006
ϵ_{trk}	0.9983 ±0.0002	0.9986 ± 0.0002
$N_{Z\to\mu^+\mu^-}$	17000 ± 136	
χ^2/ndof	1.03708	

Table 4.3: *Comparison between fit results with the fit performed on a sample corresponding to an integrated luminosity of* $45\mathrm{pb}^{-1}$ *and MC-truth values of the average efficiencies.*

	Fit results	**MC − truth**
$\boldsymbol{\int L\mathrm{dt} = 133\mathrm{pb}^{-1}}$		
ϵ_{HLT}	0.915 ± 0.001	0.917 ± 0.002
ϵ_{iso}	0.9787 ± 0.0006	0.9785 ± 0.0009
ϵ_{sa}	0.9895 ± 0.0005	0.9907 ± 0.0006
ϵ_{trk}	0.99836 ± 0.00013	0.9986 ± 0.0002
$N_{Z\to\mu^+\mu^-}$	50555 ± 234	
χ^2/ndof	1.51032	
$\boldsymbol{\int L\mathrm{dt} = 10\mathrm{pb}^{-1}}$		
ϵ_{HLT}	0.913 ±0.004	0.917 ± 0.002
ϵ_{iso}	0.982± 0.002	0.9785 ± 0.0009
ϵ_{sa}	0.9895 ± 0.0017	0.9907 ± 0.0006
ϵ_{trk}	0.9978 ± 0.0007	0.9986 ± 0.0002
$N_{Z\to\mu^+\mu^-}$	3811± 64	
χ^2/ndof	1.4888	
$\boldsymbol{\int L\mathrm{dt} = 5\mathrm{pb}^{-1}}$		
ϵ_{HLT}	0.908 ±0.005	0.917 ± 0.002
ϵ_{iso}	0.986± 0.003	0.9785 ± 0.0009
ϵ_{sa}	0.991 ± 0.002	0.9907 ± 0.0006
ϵ_{trk}	0.9970 ± 0.0011	0.9986 ± 0.0002
$N_{Z\to\mu^+\mu^-}$	1894± 45	
χ^2/ndof	1.0186	

Table 4.4: *Fit results performed on samples corresponding to an integrated luminosity of* 133, 10 *and* 5 pb^{-1}. *MC-truth values of the average efficiencies are also shown for comparison.*

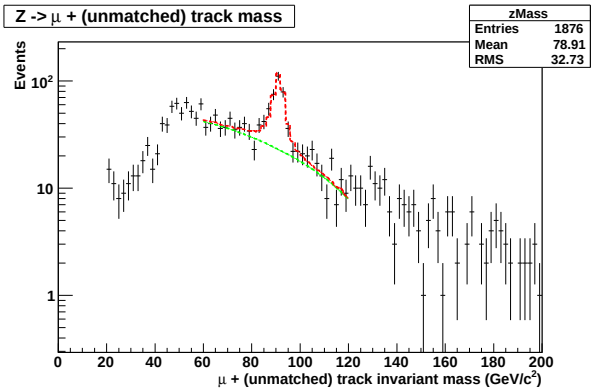

Figure 4.10: *Fit curve superimposed to the invariant mass histogram of $Z_{\mu t}$ candidates for a sample corresponding to an integrated luminosity of* 45 pb^{-1}.

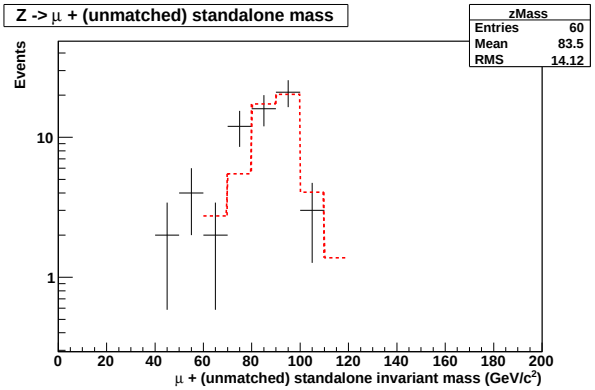

Figure 4.11: *Fit curve superimposed to the invariant mass histogram of $Z_{\mu s}$ candidates for a sample corresponding to an integrated luminosity of* 45 pb^{-1}.

deviation from the others, due to the low statistic of $Z_{\mu s}$ sample. In this case, an Unbinned Maximum Likelihood fit approach could lead to a better stability. In table 4.5 is reported the comparison between $\chi^2 - likelihood$ and χ^2 fit at an integrated luminosity of 5 pb^{-1}. We can see that the results of the combined $\chi^2 - likelihood$ fit are in agreement with the MC-truth better than the simple χ^2 fit ones, in particular the ϵ_{trk} that is sensitive to the low statisitics of $Z_{\mu s}$ sample. This kind of fit allows to have a robust fit also with a few statistics, and the results are better than ones obtained with a simple χ^2 fit.

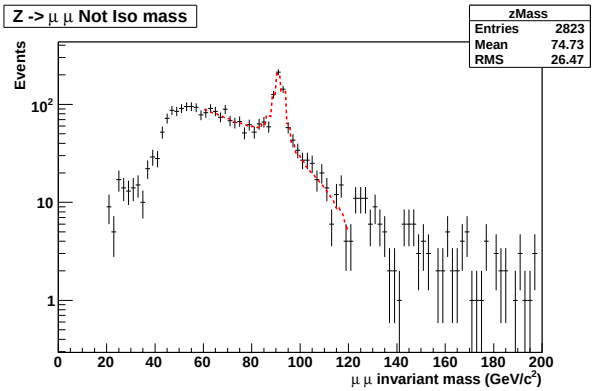

Figure 4.12: *Fit curve superimposed to the invariant mass histogram of* $Z_{\mu\mu}^{\text{non iso}}$ *candidates for a sample corresponding to an integrated luminosity of* 45 pb^{-1}.

	Combined $\chi^2 - likelihood$ Fit	χ^2 Fit
ϵ_{HLT}	0.910 ± 0.005	0.908 ±0.005
ϵ_{iso}	0.988 ± 0.002	0.986 ±0.003
ϵ_{sa}	0.993 ± 0.002	0.991 ±0.002
ϵ_{trk}	0.998 ±0.0008	0.9970 ±0.00011
$N_{Z\to\mu^+\mu^-}$	1896 ± 45	1894 ± 45

Table 4.5: *Comparison of the fit results of combined* $\chi^2 - likelihood$ *fit and* χ^2 *fit performed on a sample corresponding to an integrated luminosity of* 5pb^{-1}.

4.4.1 Toy Monte Carlo studies

In order to study the possible bias introduced by our fit method, we made a toy Monte Carlo simulating the distributions of our sample for thousands of difference experiments. The generated histograms are then given in input to the fit. We have generated 1000 toy MC experiments and have studied the pull distributions of the fitted parameters of physical interest. We have also studied the behaviour of the pulls for different luminosity scenarios by changing the statistics in the generated samples.

For a 10 pb^{-1} statistics, the pull plot of the yield, the parameter needed for the cross section determination, is satisfying (see Fig. 4.17), with no bias and the width of the distribution consistent with 1 within 2 σ. We observe a small bias in the fitted tracker efficiency (see Fig. 4.16)), with a slight asymmetry of the pull distribution. This can be related to the small statistics of the $Z_{\mu s}$ sample, which is sensitive to the tracker efficiency, leading also to some fit instabilities. The

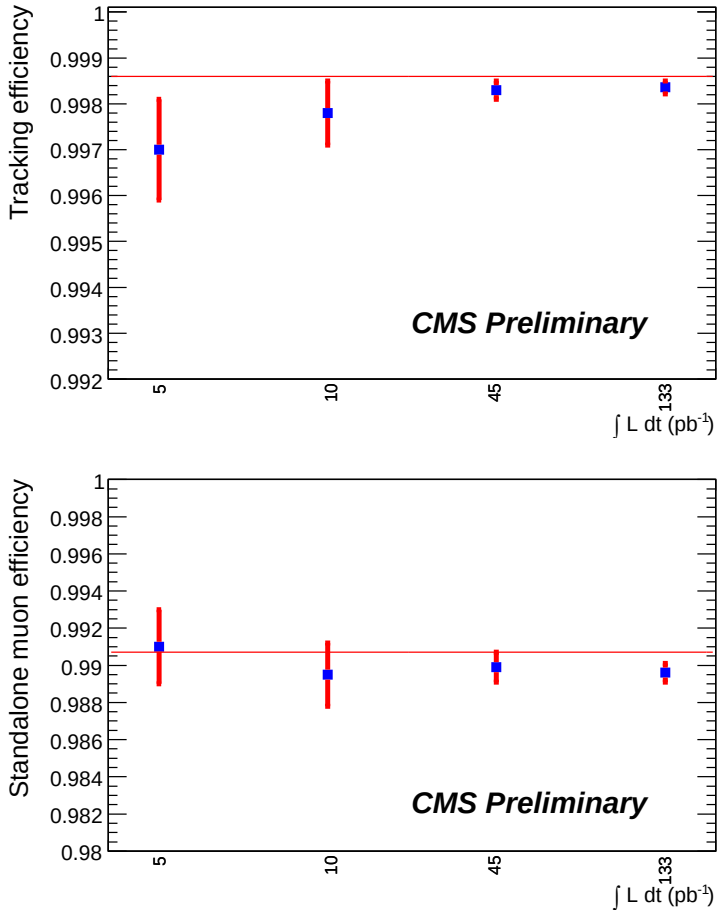

Figure 4.13: *Fitted traker (top) and muon detector (bottom) efficiencies for different integrated luminosity scenarios. The Monte Carlo true value is superimposed as a solid red horizontal line.*

bias is lower for the other efficiencies. That the observed bias is related to the low statistic of the analyzed sample, is shown by the fact that it decreases as the statistic of sample increases. However, we observe that the yield distribution, that is the number that we need for the calculation of the cross section, is unbiased.

When we increase the statistics in the samples to 45 pb^{-1}, the pull of the yield is well-behaved (see Fig. 4.18), while a small bias in the efficiencies (see Fig. 4.19) is still present.

When we increase the statistics in the samples up to 13.3 fb^{-1}, all the pulls are well-behaved, with a gaussian shape centered at zero and a width compatible with 1 (see Fig. 4.20 and 4.21). Figure 4.22 shows the distribution of the χ^2 from the fit. Discrepancies from the theoretical χ^2 distribution are evident, that

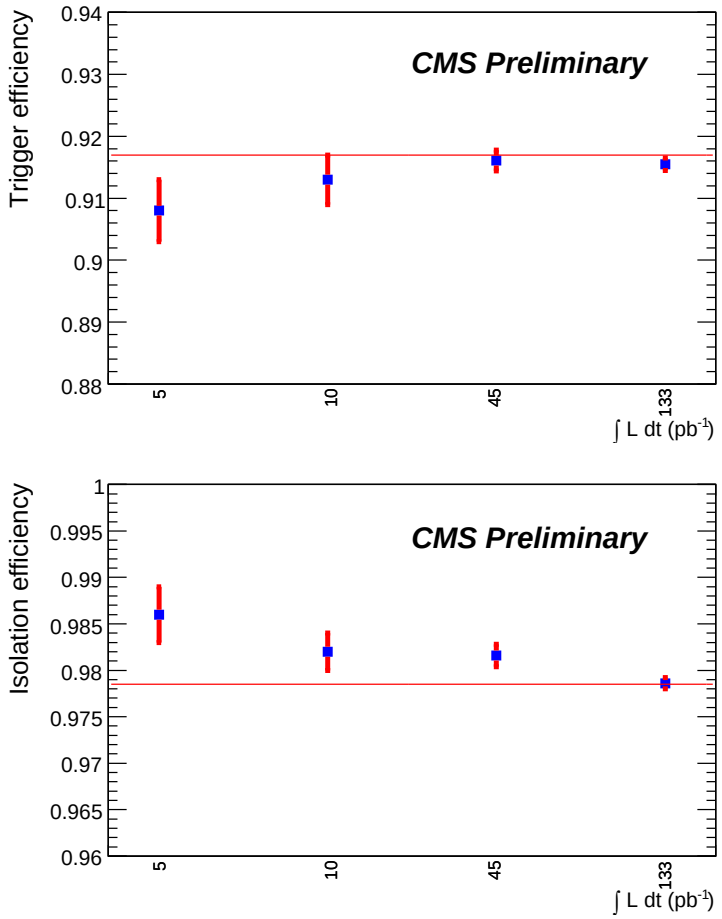

Figure 4.14: *Fitted HLT (top) and isolation (bottom) efficiencies for different integrated luminosity scenarios. The Monte Carlo true value is superimposed as a solid red horizontal line.*

leads to a reinterpretation of the probability of the χ^2 from the fit.

4.5 Comparison with the Tag and Probe method

We ran the T&P [18] code on the signal only specifying the same selection criteria we apply in the analysis.
With the available statistics, we could set a grid in p_T vs η of 4×4 bins, in the range $20 < p_T < 100 GeV/c$ and $2 < \eta < 2$. A thinner binning would have resulted in very large statistical errors in several bins, and large bin to bin fluctuation. We compared the average efficiencies obtained with the fit and T&P methods. Table 4.6 reports the average recontruction efficiencies obtained by fit method

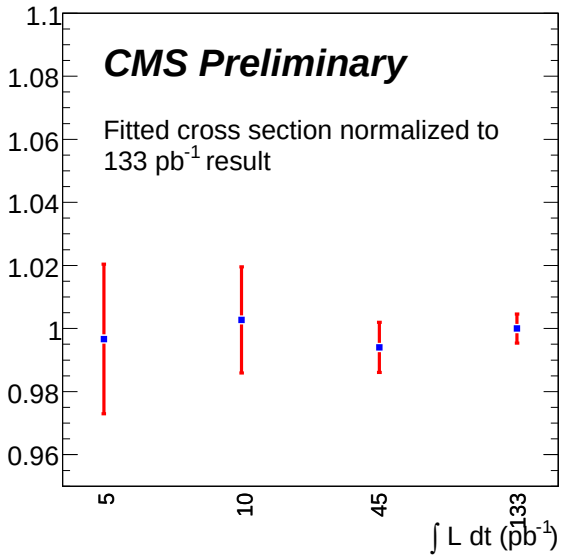

Figure 4.15: *Fitted cross section for different integrated luminosity sc*enarios. The results have been normalized to the 133 pb^{-1} determination.

and T&P respectively. The values are in good agreement into the error range even if for the calculation. Figure 4.23 shows the comparison of the dimuon

Parameters	T&P average efficiency	Fit result
ϵ_{sa}	0.929 ± 0.002	0.934 ± 0.002
ϵ_{trk}	0.9968 ± 0.0004	0.9968 ± 0.0005

Table 4.6: *Comparison between* T&P *average reconstruction efficiencies and Fit results. These values are calculated with CSA08* $Z \rightarrow \mu^+\mu^-$ *signal sample. CSA08 samples was generated with the Pythia generator, simulation and reconstruction chain, assuming a center of mass energy of* $\sqrt{s} = 10\ TeV$ *and conditions forseen after* 10 pb^{-1} *data taken of the detector.*

invariant mass distribution eweighed event by event with T&P efficiencies and with the average efficiency obtained from the fit. The two distributions are in good agreement to each other.

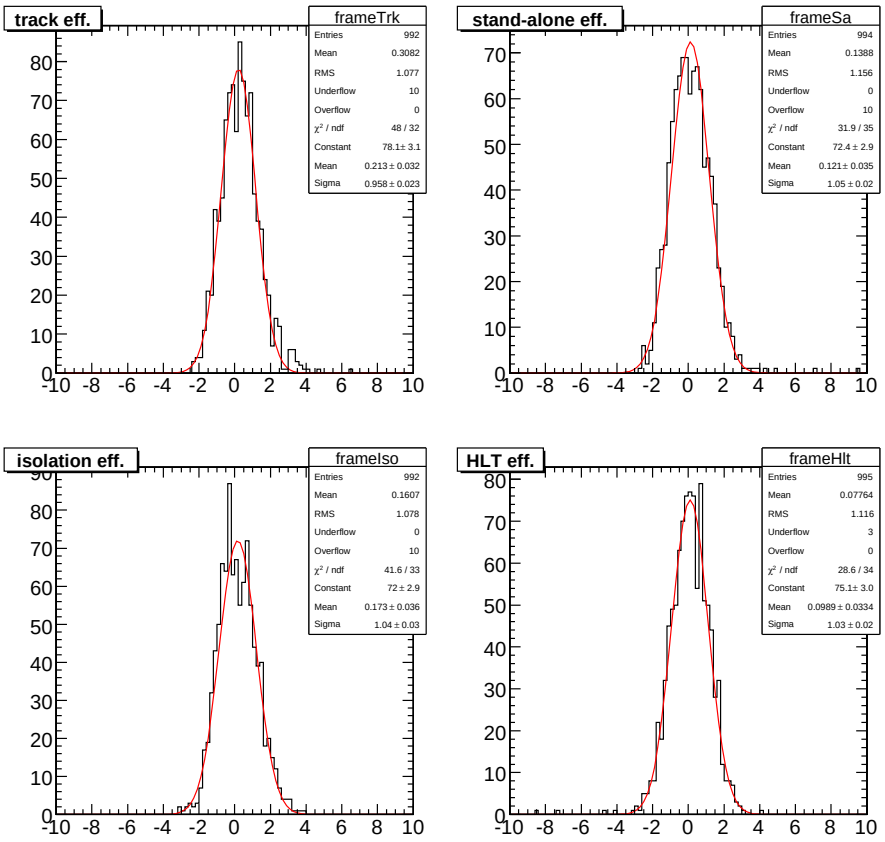

Figure 4.16: *Pull distributions of efficiencies determined in a 10 pb^{-1} sample. Upper left plot: tracker efficiency; Upper right: Standalone efficiency; Lower left: Isolation efficiency; Lower right: trigger efficiency.*

4.6 Monte Carlo efficiencies

The reconstruction efficiencies from the fit are compared to MC truth information in order to check the correctness of the method. Figures 4.24 to 4.31 show the standalone muon and the tracker track reconstruction efficiencies, the isolation cut efficiency, and the HLT efficiency as a function of η and ϕ.

4.7 Correlation studies

In the following sections we consider the possible effect of:

- kinematic correlation between the two muons

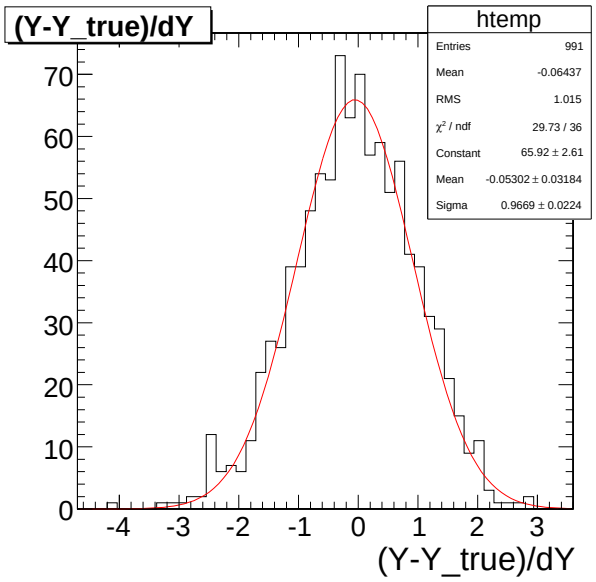

Figure 4.17: *Pull distribution of $N_{\mu\mu}$ at 10 pb^{-1}.*

- correlation of muon detector reconstruction and HLT efficiency
- correlation of tracker reconstruction and isolation efficiency

4.7.1 Efficiency correlation between the two muons

In the above fit model we assumed that we can factorize the efficiency terms for the two muons (that are products of reconstruction, isolation and HLT efficiencies). We now justify this assumptions, that consists in neglecting the correlation of the efficiency terms, and provide a method to estimate the uncertainty caused by this assumption.

In the case of ideal efficiencies, the differential Z yield, as a function of the two muon three-momenta, can be written as:

$$\frac{\mathrm{d}^3\mathrm{n}^0}{\mathrm{d}^3\mathrm{p}_1\mathrm{d}^3\mathrm{p}_2} = N^0 f^0(\vec{p_1}, \vec{p_2}) \ , \tag{4.13}$$

where N^0 is the total number of produced events, $\vec{p_1}$ and $\vec{p_2}$ are the two muons three-momenta, $f^0(\vec{p_1}, \vec{p_2})$ is the probability density function that takes into account the process matrix element, phase space, and detector resolutions.

The differential Z yield as a function of the muon pair invariant mass is:

$$\frac{\mathrm{dn}^0}{\mathrm{dm}} = N^0 \int \mathrm{d}^3\mathrm{p}_1\mathrm{d}^3\mathrm{p}_2\mathrm{f}^0(\tilde{\mathrm{p}_1}, \tilde{\mathrm{p}_2})\delta(\mathrm{m}_{12}(\tilde{\mathrm{p}_1}, \tilde{\mathrm{p}_2}) - \mathrm{m}) \ \ , \tag{4.13}$$

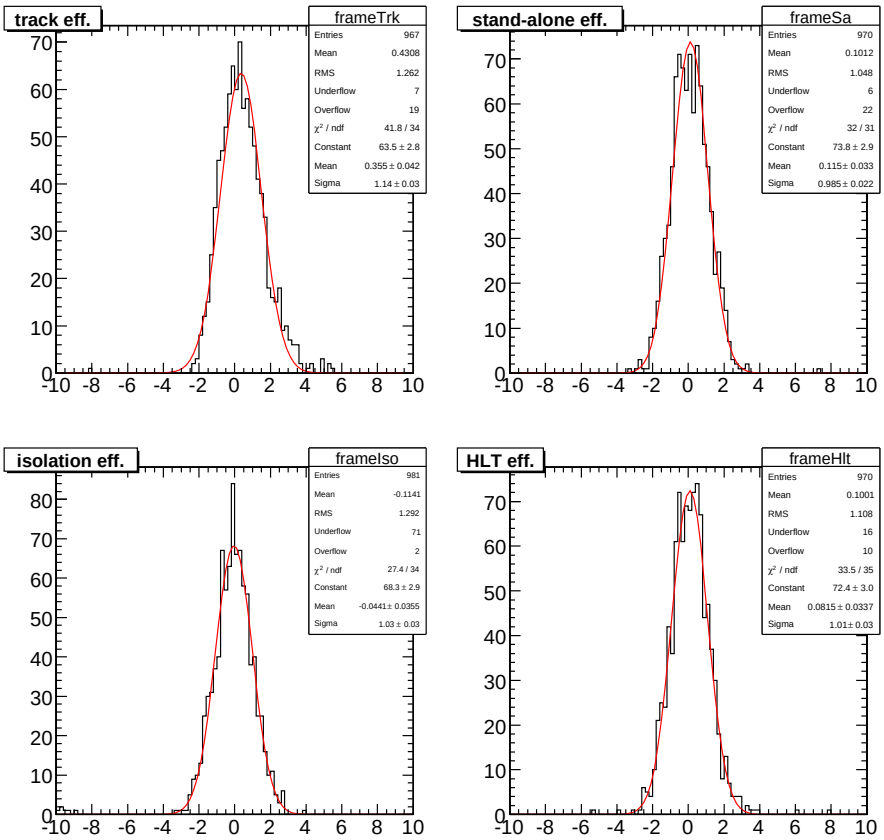

Figure 4.18: *Pull distributions of efficiencies determined in a 45 pb^{-1} sample. Upper left plot: tracker efficiency; Upper right: Standalone efficiency; Lower left: Isolation efficiency; Lower right: trigger efficiency.*

where $m_{12}(\vec{p_1}, \vec{p_2}) = 2p_1p_2(1 - \cos\theta_{12})$ is the di-muon invariant mass (neglecting the muon mass).

In order to take into account the effect of the non-ideal efficiencies, we introduce the efficiency terms for the two muons as: $\epsilon_1(\vec{p_1})$, $\epsilon_2(\vec{p_2})$, whose interpretation varies for the different samples we consider. In the case of the sample reconstructed as a pair of global muons, for instance, the two functions ϵ_1 and ϵ_2 coincide, and are equal to the product $\epsilon_{trk}(\vec{p})\epsilon_{sa}(\vec{p})\epsilon_{\rm iso}(\vec{p})\epsilon_{\rm HLT}(\vec{p})$.

Taking into account the efficiency terms, the differential yield from (4.7.1) becomes of the form:

$$\frac{\mathrm{dn}}{\mathrm{dm}} = N^0 \int \mathrm{d^3p_1 d^3p_2 f^0}(\tilde{\mathrm{p}_1}, \tilde{\mathrm{p}_2})\delta(\mathrm{m_{12}}(\tilde{\mathrm{p}_1}, \tilde{\mathrm{p}_2}) - \mathrm{m})\epsilon_1(\tilde{\mathrm{p}_1})\epsilon_2(\tilde{\mathrm{p}_2}) \quad , \tag{4.13}$$

Category	$\epsilon_1(\vec{p_1})$	$\epsilon_2(\vec{p_2})$
$Z_{\mu\mu}^{\text{2HLT}}$	$\epsilon_{trk}(\vec{p_1})\epsilon_{sa}(\vec{p_1})\epsilon_{\text{iso}}(\vec{p_1})\epsilon_{\text{HLT}}(\vec{p_1})$	$\epsilon_{trk}(\vec{p_2})\epsilon_{sa}(\vec{p_2})\epsilon_{\text{iso}}(\vec{p_2})\epsilon_{\text{HLT}}(\vec{p_2})$
$Z_{\mu\mu}^{\text{1HLT}}$	$\epsilon_{trk}(\vec{p_1})\epsilon_{sa}(\vec{p_1})\epsilon_{\text{iso}}(\vec{p_1})\epsilon_{\text{HLT}}(\vec{p_1})$	$\epsilon_{trk}(\vec{p_2})\epsilon_{sa}(\vec{p_2})\epsilon_{\text{iso}}(\vec{p_2})(1-\epsilon_{\text{HLT}}(\vec{p_2}))$
	$\epsilon_{trk}(\vec{p_1})\epsilon_{sa}(\vec{p_1})\epsilon_{\text{iso}}(\vec{p_1})(1-\epsilon_{\text{HLT}}(\vec{p_1}))$	$\epsilon_{trk}(\vec{p_2})\epsilon_{sa}(\vec{p_2})\epsilon_{\text{iso}}(\vec{p_2})\epsilon_{\text{HLT}}(\vec{p_2})$
$Z_{\mu s}$	$\epsilon_{trk}(\vec{p_1})\epsilon_{sa}(\vec{p_1})\epsilon_{\text{iso}}(\vec{p_1})\epsilon_{\text{HLT}}(\vec{p_1})$	$(1-\epsilon_{trk}(\vec{p_2}))\epsilon_{sa}(\vec{p_2})\epsilon_{\text{iso}}(\vec{p_2})$
	$(1-\epsilon_{trk}(\vec{p_1}))\epsilon_{sa}(\vec{p_1})\epsilon_{\text{iso}}(\vec{p_1})$	$\epsilon_{trk}(\vec{p_2})\epsilon_{sa}(\vec{p_2})\epsilon_{\text{iso}}(\vec{p_2})\epsilon_{\text{HLT}}(\vec{p_2})$
$Z_{\mu t}$	$\epsilon_{trk}(\vec{p_1})\epsilon_{sa}(\vec{p_1})\epsilon_{\text{iso}}(\vec{p_1})\epsilon_{\text{HLT}}(\vec{p_1})$	$\epsilon_{trk}(\vec{p_2})(1-\epsilon_{sa}(\vec{p_2}))\epsilon_{\text{iso}}(\vec{p_2})$
	$\epsilon_{trk}(\vec{p_1})(1-\epsilon_{sa}(\vec{p_1}))\epsilon_{\text{iso}}(\vec{p_1})$	$\epsilon_{trk}(\vec{p_2})\epsilon_{sa}(\vec{p_2})\epsilon_{\text{iso}}(\vec{p_2})\epsilon_{\text{HLT}}(\vec{p_2})$
$Z_{\mu\mu}^{\text{non iso}}$	$\epsilon_{trk}(\vec{p_1})\epsilon_{sa}(\vec{p_1})\epsilon_{\text{iso}}(\vec{p_1})\epsilon_{\text{HLT}}(\vec{p_1})$	$\epsilon_{trk}(\vec{p_2})\epsilon_{sa}(\vec{p_2})(1-\epsilon_{\text{iso}}(\vec{p_2}))\epsilon_{\text{HLT}}(\vec{p_2})$
	$\epsilon_{trk}(\vec{p_1})\epsilon_{sa}(\vec{p_1})(1-\epsilon_{\text{iso}}(\vec{p_1}))\epsilon_{\text{HLT}}(\vec{p_1})$	$\epsilon_{trk}(\vec{p_2})\epsilon_{sa}(\vec{p_2})\epsilon_{\text{iso}}(\vec{p_2})\epsilon_{\text{HLT}}(\vec{p_2})$
	$\epsilon_{trk}(\vec{p_1})\epsilon_{sa}(\vec{p_1})(1-\epsilon_{\text{iso}}(\vec{p_1}))\epsilon_{\text{HLT}}(\vec{p_1})$	$\epsilon_{trk}(\vec{p_2})\epsilon_{sa}(\vec{p_2})(1-\epsilon_{\text{iso}}(\vec{p_2}))\epsilon_{\text{HLT}}(\vec{p_2})$
	$\epsilon_{trk}(\vec{p_1})\epsilon_{sa}(\vec{p_1})\epsilon_{\text{iso}}(\vec{p_1})\epsilon_{\text{HLT}}(\vec{p_1})$	$\epsilon_{trk}(\vec{p_2})\epsilon_{sa}(\vec{p_2})(1-\epsilon_{\text{iso}}(\vec{p_2}))\epsilon_{\text{HLT}}(\vec{p_2})$
	$\epsilon_{trk}(\vec{p_1})\epsilon_{sa}(\vec{p_1})(1-\epsilon_{\text{iso}}(\vec{p_1}))\epsilon_{\text{HLT}}(\vec{p_1})$	$\epsilon_{trk}(\vec{p_2})\epsilon_{sa}(\vec{p_2})\epsilon_{\text{iso}}(\vec{p_2})(1-\epsilon_{\text{HLT}}(\vec{p_2}))$
	$\epsilon_{trk}(\vec{p_1})\epsilon_{sa}(\vec{p_1})(1-\epsilon_{\text{iso}}(\vec{p_1}))\epsilon_{\text{HLT}}(\vec{p_1})$	$\epsilon_{trk}(\vec{p_2})\epsilon_{sa}(\vec{p_2})(1-\epsilon_{\text{iso}}(\vec{p_2}))(1-\epsilon_{\text{HLT}}(\vec{p_2}))$
	$\epsilon_{trk}(\vec{p_1})\epsilon_{sa}(\vec{p_1})\epsilon_{\text{iso}}(\vec{p_1})(1-\epsilon_{\text{HLT}}(\vec{p_1}))$	$\epsilon_{trk}(\vec{p_2})\epsilon_{sa}(\vec{p_2})(1-\epsilon_{\text{iso}}(\vec{p_2}))\epsilon_{\text{HLT}}(\vec{p_2})$
	$\epsilon_{trk}(\vec{p_1})\epsilon_{sa}(\vec{p_1})(1-\epsilon_{\text{iso}}(\vec{p_1}))(1-\epsilon_{\text{HLT}}(\vec{p_1}))$	$\epsilon_{trk}(\vec{p_2})\epsilon_{sa}(\vec{p_2})\epsilon_{\text{iso}}(\vec{p_2})\epsilon_{\text{HLT}}(\vec{p_2})$
	$\epsilon_{trk}(\vec{p_1})\epsilon_{sa}(\vec{p_1})(1-\epsilon_{\text{iso}}(\vec{p_1}))(1-\epsilon_{\text{HLT}}(\vec{p_1}))$	$\epsilon_{trk}(\vec{p_2})\epsilon_{sa}(\vec{p_2})(1-\epsilon_{\text{iso}}(\vec{p_2}))\epsilon_{\text{HLT}}(\vec{p_2})$

Table 4.7: *List of the efficiency terms to be used in Equation (4.7.1) for the different reconstructed Z categories.*

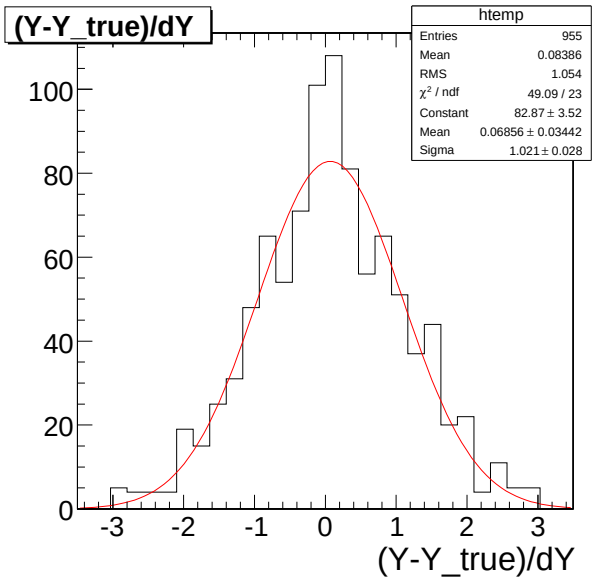

Figure 4.19: *Pull distribution of $N_{\mu\mu}$ at 45 pb^{-1}.*

or sum of similar terms with different $\epsilon_1(\vec{p_1})$ and $\epsilon_2(\vec{p_2})$. The efficiency terms for the other categories are reported in Table 4.7 for completeness.

In the fit model above we made the approximation that the efficiency terms can be factorized as average terms $\bar{\epsilon_1}$, $\bar{\epsilon_2}$:

$$\frac{\mathrm{dn}}{\mathrm{dm}} \simeq \frac{\mathrm{dn}'}{\mathrm{dm}} = N^0 \bar{\epsilon_1}\bar{\epsilon_2} \int \mathrm{d^3p_1 d^3p_2 f^0}(\tilde{\mathrm{p}_1}, \tilde{\mathrm{p}_2}) \delta(\mathrm{m_{12}}(\tilde{\mathrm{p}_1}, \tilde{\mathrm{p}_2}) - \mathrm{m}) \quad . \tag{4.13}$$

where:

$$\bar{\epsilon_1} \;=\; \langle \epsilon_1(\vec{p_1}) \rangle = \int \mathrm{d^3p_1 d^3p_2 f^0}(\tilde{\mathrm{p}_1}, \tilde{\mathrm{p}_2}) \epsilon_1(\tilde{\mathrm{p}_1}) \;, \tag{4.14}$$

$$\bar{\epsilon_2} \;=\; \langle \epsilon_2(\vec{p_2}) \rangle = \int \mathrm{d^3p_1 d^3p_2 f^0}(\tilde{\mathrm{p}_1}, \tilde{\mathrm{p}_2}) \epsilon_2(\tilde{\mathrm{p}_2}) \;. \tag{4.15}$$

The difference between the approximated and exact expressions, due to the normalization of $f(\vec{p_1}, \vec{p_2})$:

$$\int \mathrm{d^3p_1 d^3p_2 f^0}(\tilde{\mathrm{p}_1}, \tilde{\mathrm{p}_2}) = 1 \;. \tag{4.15}$$

is:

$$\frac{\mathrm{dn}}{\mathrm{dm}} - \frac{\mathrm{dn}'}{\mathrm{dm}} = N^0 \int \mathrm{d^3p_1 d^3p_2 f^0}(\tilde{\mathrm{p}_1}, \tilde{\mathrm{p}_2}) \delta(\mathrm{m_{12}}(\tilde{\mathrm{p}_1}, \tilde{\mathrm{p}_2}) - \mathrm{m})(\epsilon_1(\tilde{\mathrm{p}_1})\epsilon_2(\tilde{\mathrm{p}_2}) - \bar{\epsilon_1}\bar{\epsilon_2}) \;, \tag{4.15}$$

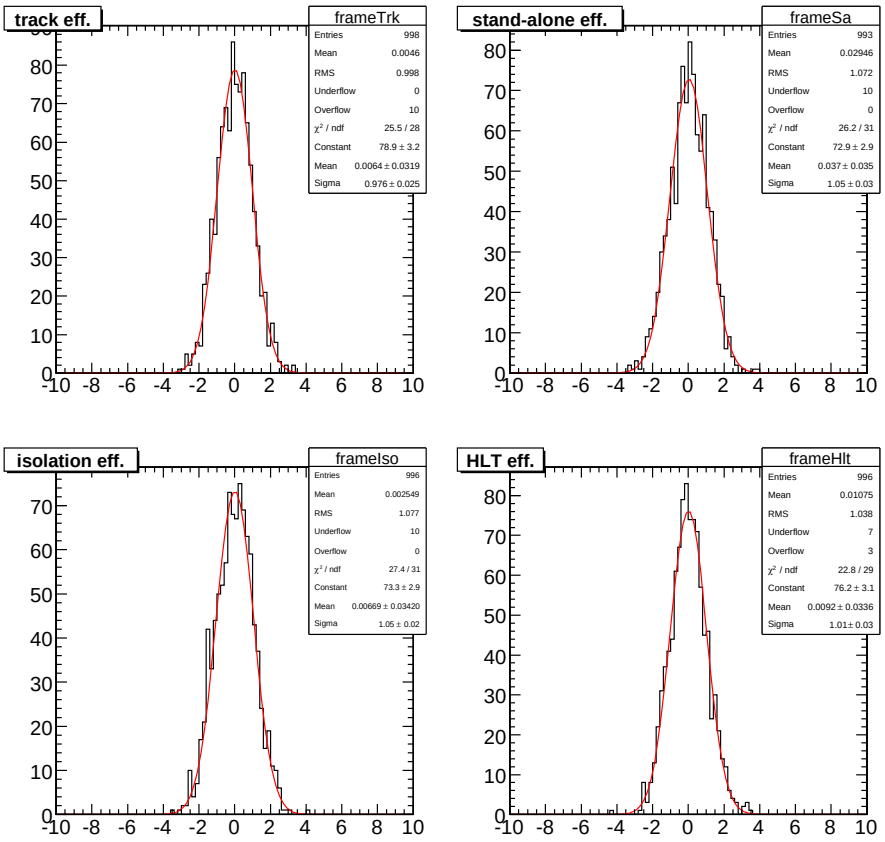

Figure 4.20: *Pull distributions of efficiencies determined in a 13.3 fb^{-1} sample. Upper left plot: tracker efficiency; Upper right: Standalone efficiency; Lower left: Isolation efficiency; Lower right: trigger efficiency.*

Integrating over the mass m, in order to extract the cross section, in a range $[m_1, m_2]$, one has:

$$N = \int_{m_1}^{m_2} \mathrm{dm} \frac{\mathrm{dn}}{\mathrm{dm}} , \tag{4.16}$$

$$N' = \int_{m_1}^{m_2} \mathrm{dm} \frac{\mathrm{dn}'}{\mathrm{dm}} , \tag{4.17}$$

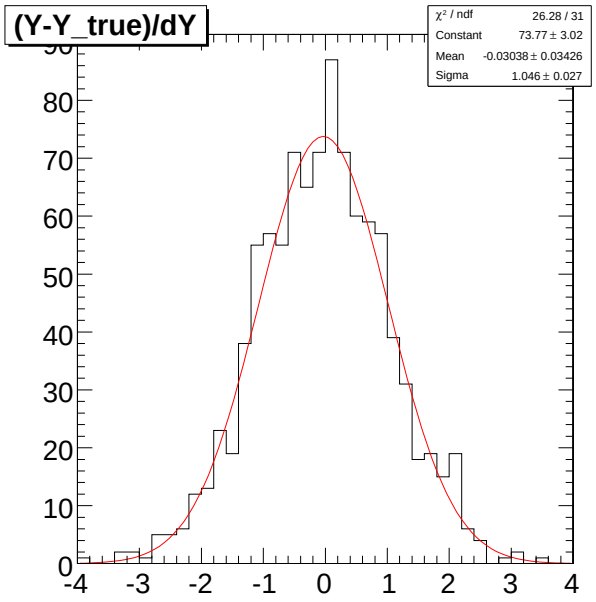

Figure 4.21: *Pull distribution of $N_{\mu\mu}$ at 13.3 fb^{-1}.*

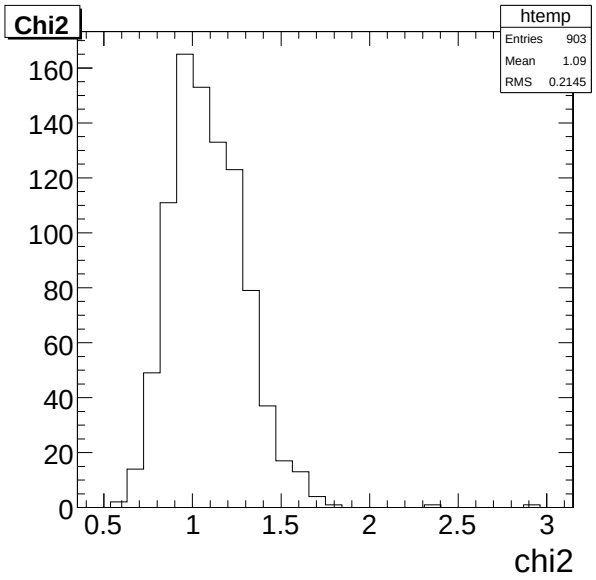

Figure 4.22: *Distribution of χ^2 at 45 pb^{-1}.*

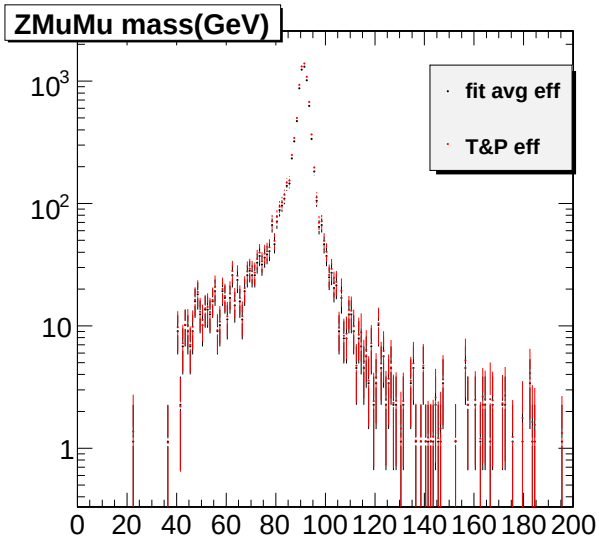

Figure 4.23: *Comparison of di-muon invariant mass distribution reweighed event by event with T& P efficiencies (in red) and with the average efficiencies from the Fit (black). The plot was obtained with CSA08 data sample.*

hence:

$$\begin{aligned} N - N' &= N^0 \int \mathrm{d^3p_1 d^3p_2 f^0}(\tilde{\mathrm{p}_1}, \tilde{\mathrm{p}_2})(\epsilon_1(\tilde{\mathrm{p}_1})\epsilon_2(\tilde{\mathrm{p}_2}) - \bar{\epsilon_1}\bar{\epsilon_2}) \\ &= N^0\langle \epsilon_1(\vec{p_1})\epsilon_2(\vec{p_2}) - \bar{\epsilon_1}\bar{\epsilon_2}\rangle \\ &= N^0\langle (\epsilon_1(\vec{p_1}) - \bar{\epsilon_1})(\epsilon_2(\vec{p_2}) - \bar{\epsilon_2})\rangle \\ &= N^0 \mathrm{cov}(\epsilon_1(\tilde{\mathrm{p}_1}), \epsilon_2(\tilde{\mathrm{p}_2})) = \mathrm{N^0 cov_{12}} \ , \end{aligned}$$

or equivalently:

$$\frac{N - N'}{N^0} = \frac{\Delta N}{N^0} = \mathrm{cov}(\epsilon_1(\tilde{\mathrm{p}_1}), \epsilon_2(\tilde{\mathrm{p}_2})) \ . \tag{4.13}$$

So, the assumption we made is equivalent to neglect the correlation term between the two muon efficiencies, $\mathrm{cov_{12}}$.

Note that the above term is quadratic in the dispersion of the efficiencies in the p_t and η range considered. So, if we assume that $\epsilon_k(\vec{p_k}) - \bar{\epsilon_k}$ $(k = 1, 2)$ is at most δ, the relative systematic error introduced by the approximation will be smaller then δ^2. This would give a first way to estimate an upper limit to this systematic effect just looking at the efficiency excursion in the T&P efficiency tables: a 10% effect would give a 1% effect.

A more precise way to estimate this effect could be done using the T&P efficiency tables ($\epsilon_k^{tp}(\vec{p})$). We could estimate the needed terms as discrete averages

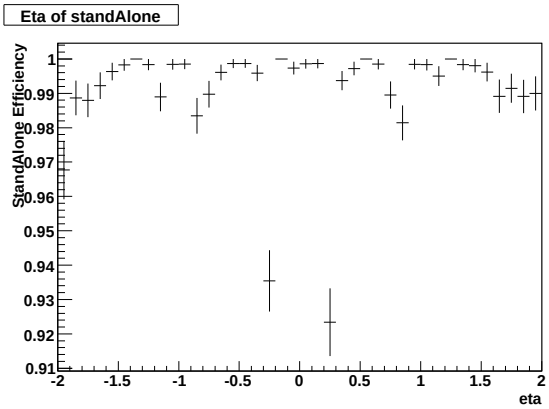

Figure 4.24: *Standalone muon efficiency vs η according to MC truth.*

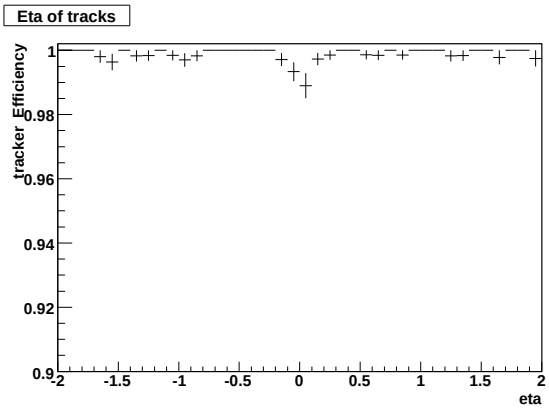

Figure 4.25: *Tracker track efficiency vs η according to MC truth.*

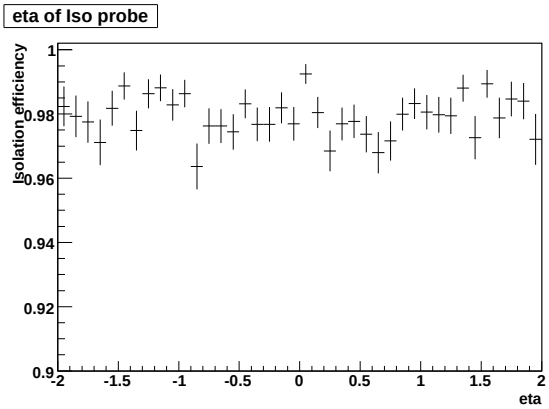

Figure 4.26: *Isolation cut efficiency vs η according to MC truth.*

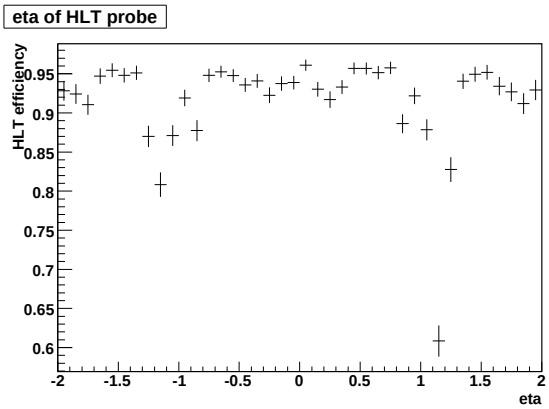

Figure 4.27: *HLT efficiency vs η according to MC truth for global muons.*

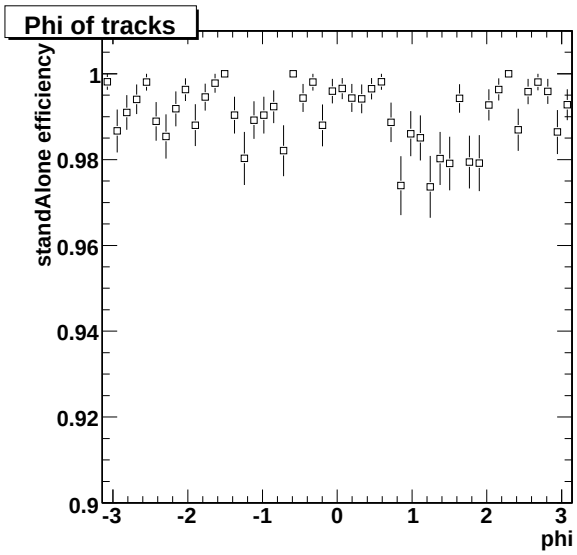

Figure 4.28: *Standalone muon efficiency vs ϕ according to MC truth.*

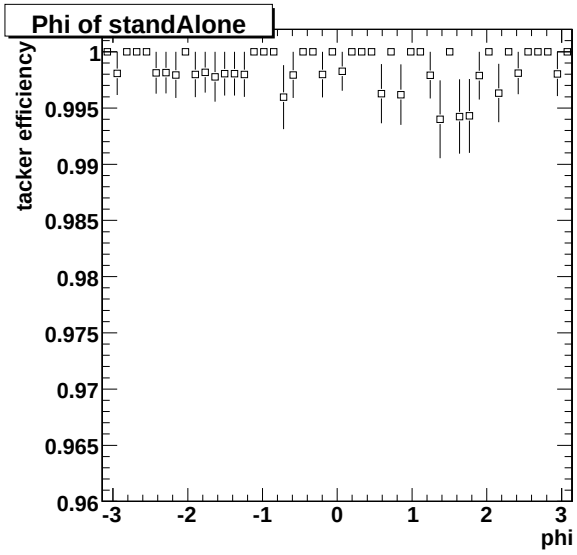

Figure 4.29: *Tracker track efficiency vs ϕ according to MC truth.*

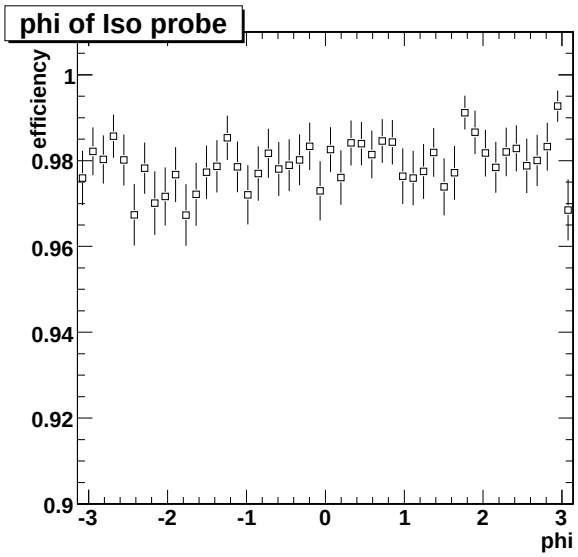

Figure 4.30: *Isolation cut efficiency vs ϕ according to MC truth.*

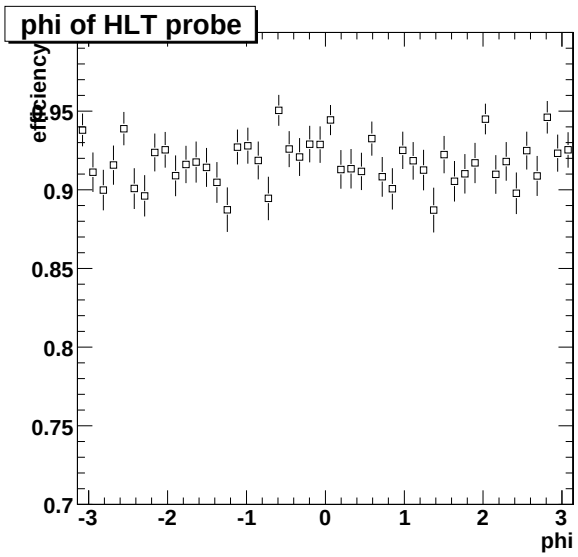

Figure 4.31: *HLT efficiency vs ϕ according to MC truth for global muons.*

over the signal sample:

$$\bar{\epsilon}^{k}_{tp} = \frac{1}{N^{\mu,\,k}_{\rm obs}} \sum_{i=1,...n}^{N^{\mu,\,k}_{\rm obs}} \epsilon^{k}_{tp}(\vec{p_i}) \tag{4.13}$$

and:

$$\begin{aligned} {\rm cov}^{\rm tp}_{12} &= \frac{1}{N^{Z}_{\rm obs}} \sum_{i=1,...n}^{N^{Z}_{\rm obs}} (\epsilon^{tp}_{1}(\vec{p_{1(i)}}) - \bar{\epsilon}^{tp}_{1})(\epsilon^{tp}_{2}(\vec{p_{2(i)}}) - \bar{\epsilon}^{tp}_{2}) & (4.14) \\ &= \frac{1}{N^{Z}_{\rm obs}} \sum_{i=1,...n}^{N^{Z}_{\rm obs}} \epsilon^{tp}_{1}(\vec{p_{1(i)}})\epsilon^{tp}_{2}(\vec{p_{2(i)}}) - \bar{\epsilon}^{tp}_{1}\bar{\epsilon}^{tp}_{2} \ . & (4.15) \end{aligned}$$

Above, $N^{Z}_{\rm obs}$ is the number of observed Z events and is the number of observed muons in Z events for the two category $k = 1,\, 2$ or for the unique category, in case of Z reconstructed from a pair of global muons. We performed this studies and we estimate to be 0.011%. Such a low value justifies the assumption that the average efficiencies can be factorized in the fit.

4.7.2 Correlation between HLT efficiency and Reconstruction efficiency

In this section we discuss the correlation between HLT and reconstruction efficiency. This correlation cannot be neglected a-priori and brings to the definition of an effective average HLT efficiency.

We rewrite Equation (4.14) as follows:

$$\bar{\epsilon_i} = \langle \epsilon_i(\vec{p_i}) \rangle = \int {\rm d^3p_1 d^3p_2 f^0}(\tilde{\rm p_1}, \tilde{\rm p_2}) \epsilon_{\rm i}(\tilde{\rm p_i}) \ , {\rm i} = 1, 2 \ , \tag{4.15}$$

where $\epsilon_i(\vec{p_i})$, $i = 1, 2$, is one of the terms listed in Table 4.7. We define for simplicity, omitting the subscript i:

$$\bar{\epsilon} = \langle \epsilon(\vec{p}) \rangle = \int {\rm d^3p f^0}(\tilde{\rm p}) \epsilon(\tilde{\rm p}) \ , \tag{4.15}$$

where, for $i = 1$, $f^0(\vec{p_1}) = \int {\rm d^3p_2 f^0}(\tilde{\rm p_1}, \tilde{\rm p_2})$, and similarily for $i = 2$, $f^0(\vec{p_2}) = \int {\rm d^3p_1 f^0}(\tilde{\rm p_1}, \tilde{\rm p_2})$.

In the case of the sample reconstructed as a pair of global muons, for instance, the average:

$$\bar{\epsilon} = \langle \epsilon_{trk}(\vec{p}) \epsilon_{sa}(\vec{p}) \epsilon_{\rm iso}(\vec{p}) \epsilon_{\rm HLT}(\vec{p}) \rangle \tag{4.15}$$

will not coincide with the product of the averages: $\langle \epsilon_{trk}(\vec{p}) \rangle \langle \epsilon_{sa}(\vec{p}) \rangle \langle \epsilon_{\rm iso}(\vec{p}) \rangle \langle \epsilon_{\rm HLT}(\vec{p}) \rangle$, and again we can assume factorization wherever correlation terms can be neglected. This is a reasonable assumption for $\epsilon_{\rm iso}(\vec{p})$, that is uncorrelated with

respect to the other terms, and $\epsilon_{trk}(\vec{p})$, while it is probably not the case for $\epsilon_{sa}(\vec{p})$ and $\epsilon_{\rm HLT}(\vec{p})$, which can be correlated, since single muon trigger is very related to the geometry of the muon detector.

When we express the differential Z yields of the different categories, we have, for each of the two muons, efficiency terms that contain $\epsilon_{sa}(\vec{p})$ and $\epsilon_{\rm HLT}(\vec{p})$ either as products $\epsilon_{sa}(\vec{p}) \cdot \epsilon_{\rm HLT}(\vec{p})$, or as single terms containing just $\epsilon_{sa}(\vec{p})$. We never find single terms in $\epsilon_{\rm HLT}(\vec{p})$. Thus, when we compute the average terms, we are still allowed to use factorization in Equations (4.12), (4.13), (4.14), (4.15) and (4.16), but we have to re-define $\epsilon_{\rm HLT}$ as:

$$\epsilon_{\rm HLT} = \frac{\langle \epsilon_{sa}(\vec{p}) \cdot \epsilon_{\rm HLT}(\vec{p}) \rangle}{\langle \epsilon_{sa}(\vec{p}) \rangle} \ , \tag{4.15}$$

which coincides with the naive interpretation of average of the HLT efficiency only in case of negligible correlation beween efficiencies. Indeed, in this case we have:

$$\langle \epsilon_{sa}(\vec{p}) \cdot \epsilon_{\rm HLT}(\vec{p}) \rangle = \langle \epsilon_{sa}(\vec{p}) \rangle \langle \epsilon_{\rm HLT}(\vec{p}) \rangle \ . \tag{4.15}$$

and hence $\epsilon_{\rm HLT} = \langle \epsilon_{\rm HLT}(\vec{p}) \rangle$. We will not make this assumption, thus in the following $\epsilon_{\rm HLT}$ stands for the ratio given by Equation (4.7.2).

4.7.3 Correlation between tracking efficiency and isolation efficiency

A correlation between tracking efficiency and isolation efficiency may occour in case of very bad tracker noise or large event pile-up situation, in which a simultaneous loss of tracker efficiency and isolation power generated by excess of noise in some detector regions could be present.

If we don't neglect this correlation, a similar treatment as it was discussed in Section 4.7.2 can be done. In a similar way, we can re-define an "effective" isolation efficiency, similarly to Eq. (4.7.2):

$$\epsilon_{\rm iso} = \frac{\langle \epsilon_{trk}(\vec{p}) \cdot \epsilon_{\rm iso}(\vec{p}) \rangle}{\langle \epsilon_{trk}(\vec{p}) \rangle} \ . \tag{4.15}$$

All efficiency terms in the definition of Z categories from Equations (4.12), (4.13), (4.15) and (4.16) remain unchanged, but correlation must be takein into account in the efficiency term of the $Z_{\mu s}$ category, in Equation (4.14). The term, including correlation, is:

$$\begin{aligned} &\langle \epsilon_{trk}(\vec{p_1}) \epsilon_{\rm iso}(\vec{p_1}) (1 - \epsilon_{trk}(\vec{p_2})) \epsilon_{\rm iso}(\vec{p_2}) \rangle + \\ &\langle (1 - \epsilon_{trk}(\vec{p_1})) \epsilon_{\rm iso}(\vec{p_1}) \epsilon_{trk}(\vec{p_2}) \epsilon_{\rm iso}(\vec{p_2}) \rangle = \\ &\qquad 2 \langle \epsilon_{trk} \epsilon_{\rm iso} \rangle (\langle \epsilon_{\rm iso} \rangle - \langle \epsilon_{trk} \epsilon_{\rm iso} \rangle) \ . \end{aligned}$$

Replacing in the above term:

$$\langle \epsilon_{trk}\epsilon_{\rm iso} \rangle = \epsilon_{trk}\epsilon_{\rm iso}$$

$$\langle \epsilon_{\rm iso} \rangle = \epsilon_{\rm iso} - \frac{{\rm COV}_{\rm trk\,iso}}{\epsilon_{trk}} = \epsilon_{\rm iso}\left(1 - \frac{{\rm COV}_{\rm trk\,iso}}{\epsilon_{trk}\epsilon_{\rm iso}}\right) .$$

We can corrected Equations (4.14) including a possible correlation term:

$$N_{\mu s} = 2N_{Z\to\mu^+\mu^-}\epsilon_{\rm HLT}\epsilon^2_{\rm iso}\epsilon_{trk}\epsilon^2_{sa}\left((1-\epsilon_{trk}) - \frac{{\rm COV}_{\rm trk\,iso}}{\epsilon_{trk}\epsilon_{\rm iso}}\right) . \qquad (4.12)$$

This correction would only affect the $Z_{\mu s}$ category that is used to determine the tracker efficiency which we expect that, under normal detector operation, would be very close to one. So, we expect this category to be the one with the smallest statistics. A deviation of the number of $Z_{\mu s}$ events would result in a corresponding variation on the tracker inefficieny $(1-\epsilon_{trk})$, that would result in a much smaller relative variation of ϵ_{trk}, being ϵ_{trk} close to the unity.

If this covariance term would turn out to be significantly different from zero, as alternative, we can drop the isolation request to the stand-alone muon, and this will allow to fully absorbe the covariance term into the redefinition of $\epsilon_{\rm iso}$, as done in Section 4.7.2 for $\epsilon_{\rm HLT}$.

We hope that tracker background and event pile-up won't have such a serious impact, especially at low luminosity, to impair dramatically the tracker performance. Anyway, in order to extimate correctly the correlation term under those pessimistic conditions, a realistic estimate would need either a proper simulation of those detector and run conditions, or control samples from real data taken under those conditions. It's important to note that the same effect may also affect other currently used methods to estimate detector efficiencies, such as the Tag and Probe method.

4.8 Kinematic acceptance

The kinematic acceptance of the applied kinematic selection can be evaluated with Monte Carlo, and is somewhat sensitive to the generator adopted. We studied it on the generated sample, before applying the skim.

In order to use the Monte Carlo estimate, we need to verify that the acceptance estimated on generator particle and on reconstructed muons is identical and not affected too much from resolution effects. For this purpose, we considered all oppositely charged di-muon pairs matched to their Monte Carlo Z parent. On that sample, we determined the fraction of reconstructed di-muon pairs passing the kinematic selection, and the fraction of the corresponding matched Monte Carlo Z passing the same selection. The fractions obtained are:

$$\epsilon^{\rm kin}_{\rm MC} = 5415/8613 = 0.6287 \pm 0.0050 \qquad (4.13)$$

$$\epsilon^{\rm kin} = 5818/8613 = 0.6290 \pm 0.0050 \qquad (4.14)$$

Given the very good agreement of $\epsilon^{\rm kin}_{\rm MC}$ and $\epsilon^{\rm kin}$, we can safely determine the kinematic acceptance directly from Monte Carlo generator. On the full generated sample we estimate the acceptance to be:

$$\epsilon^{\rm kin} = 5424/9000 = 0.6027 \pm 0.0050 \tag{4.14}$$

This acceptance refers only to the events that pass the generator filter, so the complete acceptance should also take into account the filter efficiency.

4.9 Cross section results and comparisons

The $Z \to \mu^+\mu^-$ yield extracted from the fit is already corrected by the reconstruction efficiencies in the tracker and in the muon system,as well as by the isolation cut and HLT efficiencies. We can measure the inclusive cross section for the $pp \to Z + X \to \mu^+\mu^- + X$ process according to this relation:

$$\sigma_{\mu^+\mu^-} = \sigma_Z \times Br\left[Z \to \mu^+\mu^-\right] = \frac{N_{Z\to\mu^+\mu^-}}{\epsilon^{\rm kin}\overline{L}}. \tag{4.14}$$

Where $\overline{L}$ is the integrated luminosity:

$$\overline{L} = \int L dt. \tag{4.14}$$

Using the results of the fit performed for an integrated luminosity of 45 pb^{-1}, we obtain the following value for cross section measurement:

$$\sigma_{\mu^+\mu^-} = 626.8 \pm 5.9 \text{ pb} \ . \tag{4.14}$$

The value of generator cross section, already scaled for the generator efficiency, is 627,1. Therefore the values obtained is in good agreement with the expected value within 1σ.

4.10 Systematics on geometric acceptance

In our fit strategy, geometric acceptance is the only quantity we evaluate from Monte Carlo to obtain the cross section. A study on the associated systematic error is given, together with a more complete list of the various contributions to the systematics on the cross section measurement. We identified at least three systematic uncertainty contributions to the geometric acceptance:

- choice of the generator type: a comparison between Pythia6 (LO) and MC@NLO is reported;
- parton distribution functions (PDF) uncertainties;

- momentum scale uncertainty.

Passing from a LO to a NLO generator some small changes in the kinematic p_T distribution of the muons are evident. The table 4.8 reports the variation of the acceptance A for Pythia and MC@NLO generated. The values are given varying the mass cut, according to the formula for the acceptance (intended to pass from the fitted region to a slightly enlarged region):

$$A = \frac{N(p_T > 20, |\eta| < 2, 60 < m_{\mu\mu} < 120)}{N(m_{\mu\mu} > m_{cut})}. \tag{4.14}$$

	$m_{cut} = 20$	$m_{cut} = 30$	$m_{cut} = 40$
$\frac{A_{Pythia} - A_{MC@NLO}}{A_{Pythia}}$	-1.2%	-3.4%	-3.3%

Table 4.8: *Variation for the geometric acceptance between Pythia and MC@NLO $Z_{\mu\mu}$ events.*

The observed variation is of the order of few percent and increases with mass cut.
All the LHC measurements will be affected, especially during the fist years of data taking, by the PDF uncertainties. We have used PDF : taken from the following groups: CTEQ6 and MSTW2008. A PDF set belonging to these groups has 20 parameters, each with a plus/minus uncertainty. A recent technique, namely the PDF reweighting (see [74]), has been exploited to estimate the uncertainties due to the particular PDF set choice, obtaining the results reported into the tables 4.9 and 4.10.

	CTEQ		
	6L1 (Pythia6 LO)	6.1 (NLO)	6.5 (NLO)
A	0.2018 ± 0.0012	$0.217^{+2.7\%}_{-4.9\%}$	$0.215^{+3.1\%}_{-4.9\%}$
$\frac{A - A_{CTEQ6.5}}{A_{CTEQ6.5}}$	-4.5%	$+0.9\%$	0

Table 4.9: *Acceptance uncertainty due CTEQ PDF. The acceptance is defined for both muons having $p_T > 20GeV/c$, $|\eta| < 2.0$, and $M_{\mu^+\mu^-} > 40GeV/c^2$.*

Another important contribution to the systematics affecting our measurements is the miscalibration of the momentum scale. To simulate this effect a simple shift of $\pm$ 1% and 2% , and a gaussian smearing of 1% and 2% has been

	MSTW2008(68cl)		
	LO	NLO	NNLO
A	$0.197^{+1.3\%}_{-1.6\%}$	$0.223^{+1.6\%}_{-1.5\%}$	$0.221^{+1.5\%}_{-2.1\%}$
$\frac{A-A_{CTEQ6.5}}{A_{CTEQ6.5}}$	-8.0%	$+3.7\%$	$+2.8\%$

Table 4.10: *Acceptance uncertainty due to MSTW2008(68cl) PDF. The acceptance is defined for both muons having* $p_T > 20, |\eta| < 2.0$, *and* $M_{\mu^+\mu^-} > 40$.

	$+1\%$ on p_T	-1% on p_T
$\frac{A-A_{LO}}{A_{LO}}$	$+0.4\%$	-0.3%
	$+2\%$ on p_T	-2% on p_T
$\frac{A-A_{LO}}{A_{LO}}$	$+0.6\%$	-0.5%
	1% Gaussian smearing	2% Gaussian smearing
$\frac{A-A_{LO}}{A_{LO}}$	$+0.3\%$	-0.4%

Table 4.11: *Acceptance uncertainty due to momentum scale. The acceptance is defined for both muons having* $p_T > 20 GeV/c$, $|\eta| < 2.0$, *and* $m_{\mu\mu} > 40 GeV/c^2$.

applied to the muon momentum and the variation of the acceptance has been evaluated. The results are riported in table 4.11. A summary table 4.12 is given with all the systematic errors for the $Z_{\mu\mu}$ cross section measurements.

Source	Uncertainty
LHC Luminosity	10%
MC order choice	$\sim 3\%$
PDF uncertainty	$\sim 4\%$
Momentum scale	$\sim 0.5\%$
fit isolation cuts	$\sim 0.3\%$
correlation between Muon efficiencies	$\sim 0.01\%$

Table 4.12: *Preliminary list of systematics sources for $Z_{\mu\mu}$ cross section measurement.*

4.11 Conclusions

We have studied the feasibility of the measurement of the inclusive $Z \rightarrow \mu^+\mu^-$ production cross section at LHC with a simultaneous fit of the $Z \rightarrow \mu^+\mu^-$ yield, the reconstruction efficiency, the isolation cut efficiency as well as the HLT efficiency. The method is consistent if we neglect the correlation between the muon efficiencies for different three-momenta, which represents a second order effect in the efficiency dispersion. The results of the fit appear consistent with the Monte Carlo truth and stable as a function of different integrated luminosity. A toy Monte Carlo study shows that the implemented fit method is slightly biased at low integrated luminosity. However the $Z \rightarrow \mu^+\mu^-$ yield that we need for the cross-section calculation remains unbiased. This method is suitable at LHC start-up because input from Monte Carlo simulation is used only for the calculation of the geometrical acceptance, with a systematic error of the order of few percent. In addition, the results of this analysis could be used to calculate the muon reconstruction efficiencies in alternative to the T&P method, that needs much more statistic for the physical background suppression. Indeed, it could be possible to apply this analysis method in bins of $p_T \times \eta$ and to obtain the efficiency tables.
Finally the robustness of method, the rapidity of execution of the full analysis chain, makes the analysis usefull to be integrated in the off-line Data Quality Monitoring for the LHC luminosity monitoring, using the measured Z yield, and in prompt analysis chain.

Conclusion

This thesis has presented a study of the inclusive process $pp \rightarrow Z + X \rightarrow \mu+\mu^- + X$ with the CMS detector at LHC at a centre of mass energy of $\sqrt{s} = 10$ TeV, which up to the LHC schedule of summer 2009 has been considered the initial centre of the mass energy of LHC collisions. However, for the updated schedule this energy will be reached at the end of 2010. The Z production, with subsequent decay in two muons, has a large cross section, $\sim 2nb$, and it will be studied already with the first data taken at the LHC, thanks also to its very clear signature: two isolated high-p_T muons in the final state with an invariant mass consistent with the Z boson mass. The analyzed channel is very interesting because it will allow to calibrate the detector and estimate the efficiencies of muon reconstruction in the inner-tracker as well as in the muon system, already from the startup of the machine. It could also be used to monitor the LHC collider luminosity during all the period of activity. Furthermore it will be very important in the detection of New Physics events characterized by two muons. In this thesis an entirely data-driven analysis method of this channel has been developed. The analysis method presented will allow to measure the yield of signal events as well as muon reconstruction, trigger, and isolation cut efficiencies directly from data, without any assumption from Monte Carlo, resulting in a reduction of systematic uncertainties. An accurate study on the performances and the stability of the analysis results has been done using Monte Carlo samples of signal and backgrounds with statistic corresponding to different integrated luminosity. The obtained results are that the strategy developed is applicable already with an integrated luminosity of 5 pb^{-1}. A toy Monte Carlo study shows that for this integrated luminosity, the implemented fit is slightly biased in the determination of the efficiencies, even if the $Z \rightarrow \mu^+\mu^-$ yield, that we need for the cross-section calculation is unbiased. The cross section measurement has been obtained from the fitted yield, the known integrated luminosity of the sample, and also the kinematic acceptance. This last term is the unique parameter of this analysis estimated from Monte Carlo. The result is in very good agreement with the expected generator cross section, within 1 σ, with a statistical error of 1 % for a analysis made on a data sample corresponding to an integrated luminosity of 45 pb^{-1} . In addition a first study on the systematics affecting this measurement is presented. It shows that the systematic error due to the knowledge of the Parton

Distribution Function, to order of generator, and p_T muon scale are of the order of few percent. In conclusion the cross section measurement will be dominated, as well as all measurement that will be made at LHC, by a systematic error of the 10%, due to the uncertainty on the luminosity measurement. Indeed to calibrate LHC and to reach a precise measurement of LHC luminosity, it will need about 1 fb^{-1} of data taken. The work presented in this thesis has been included in a CMS internal note [71] officially accepted by the CMS collaboration so it is waiting to validate and to test on the first data taking of CMS.

List of Figures

List of Tables

Bibliography

[1] S.Glashow, Nucl. Phys. 22 579 (1961).

[2] S.Weinberg, Phys. Rev. Lett. 19 1264 (1967)

[3] A.Salam, Elementary particle Theory , Ed. N. Svarholm (1968).

[4] Y. Fukuda, et al., Phys. Rev. Lett. B 81 (1998) 1562.

[5] Q.R. Ahmad, et al., Phys. Rev. Lett. 87 (2001) 071301.

[6] J. Ellis, M. Jacob, Phys. Rep. (2004), this volume [doi:10.1016/j.physrep.2004.08.015].

[7] LHC Machine Lyndon Evans and Philip Bryant (editors) 2008 JINST 3 S08001 [doi: 10.1088/1748-0221/3/08/S08001]

[8] Herbert Goldstein, Meccanics, Zanichelli.

[9] F. Mandl G Shaw, Quantum Field Theory.

[10] Peter Higgs, Broken Symmetries and the Masses of Gauge Bosons. Phys. Rev. Lett.3 13, 508 (1964).

[11] Weinberg, Steven, The Quantum Theory of Fields, Volume 3: Supersymmetry, Cambridge University Press, Cambridge, (1999). ISBN 0-521-66000-9.

[12] P. Fayet, S. Ferrara, Phys. Rep. C 32 (1977) 249;

[13] H.P. Nilles, Phys. Rep. C 110 (1984);

[14] H.E. Haber, G.L. Kane, Phys. Rep. C 117 (1985) 75.

[15] K. D. Lane, An Introduction to technicolor," hep-ph/9401324.

[16] Kaluza, Theodor (1921). "Zum Unittsproblem in der Physik". Sitzungsber. Preuss. Akad. Wiss. Berlin. (Math. Phys.) 1921: 966972.

[17] CMS Analysis Note: Towards a measurement of the inclusive $W \to \mu\nu$ and $Z \to \mu^+\mu^-$ cross sections in pp collisions at $\sqrt{14}TeV$.

[18] The CMS Collaboration, Generic Tag and Probe Tool for Measuring Efficiency at CMS with Early Data, CMS AN-2008 (2008).

[19] Physics at the LHC, F. Gianotti Physics Reports 403404 (2004) 379 399.

[20] Top Physics at LHC with $t\bar{t}$ events,F. HUBAUT.arXiv:hep-ex/0605029v1 10 May 2006

[21] J. Christenson, et al., Phys. Rev. Lett. 13 (1964) 138.

[22] H. Wahl, Phys. Rep. (2004), this volume [doi:10.1016/j.physrep.2004.08.007];

[23] R. Forty, Phys. Rep. (2004), this volume [doi:10.1016B. Aubert, et al., Phys. Rev. Lett. 86 (2001) 2515.

[24] BABAR collaboration, The BABAR detector, Nucl. Instrum. Meth. A 479 (2000) 1.

[25] K. Abe, et al., Phys. Rev. Lett. 87 (2001) 091802.

[26] SLAC Linear Collider Conceptual Design Report, SLAC-R-229, Internal report, SLAC 1980.

[27] See for instance M. Lisa, What have we learned so far? An experimental perspective, talk given at Quark Matter 2004, Oakland, January 2004, http://www.lbl.gov/nsd/qm2004/program.html.

[28] LEP Disign Report, CERN-LEP/84-01, Internation report, CERN 1984.

[29] S Myer and E. Picasso, Contemp. Phys 31 (1990) 387-403.

[30] The ATLAS Experiment at the CERN Large Hadron Collider, 2008 JINST 3 S08003 (http://iopscience.iop.org/1748-0221/3/08/S08003)

[31] The CMS experiment at the CERN LHC, 2008 JINST

[32] The ALICE experiment at the CERN LHC, 2008 JINST 3 S08002 (http://iopscience.iop.org/1748-0221/3/08/S08002)

[33] The LHCb Detector at the LHC, 2008 JINST 3 S08005 (http://iopscience.iop.org/1748-0221/3/08/S08005)

[34] CMS collaboration, The CMS tracker system project: technical design report, CERN-LHCC-98-006, http://cdsweb.cern.ch/record/368412.

[35] CMS collaboration, The CMS tracker: addendum to the technical design report, CERN-LHCC-2000-016, http://cdsweb.cern.ch/record/490194.

[36] CMS collaboration, The electromagnetic calorimeter project: technical design report, CERN-LHCC-97-033, http://cdsweb.cern.ch/record/349375;

[37] CMS ECAL: addendum to the technical design report, CERN-LHCC-2002-027, http://cdsweb.cern.ch/record/581342.

[38] R. Loos et al., CMS ECAL Preshower and Endcap Engineering Design Review. v.2 - Preshower, CMS-2000-054-MEETING, CERN-ECAL-EDR-4, http://cdsweb.cern.ch/record/539819.

[39] CMS collaboration, The hadron calorimeter project: technical design report, CERN-LHCC-97-031, http://cdsweb.cern.ch/record/357153.

[40] S. Abdullin et al., Design, performance, and calibration of CMS hadron-barrel calorimeter wedges, Eur. Phys. J. 55 (2008) 159, CMS-NOTE-2006-138, http://cdsweb.cern.ch/record/1049915.

[41] D. DEnterria et al., CMS physics technical design report: addendum on high density QCD with heavy ions, J. Phys. G 34 (2007) 2307, CERN-LHCC-2007-009, http://cdsweb.cern.ch/record/1019832.

[42] CMS collaboration, The CMS muon project, technical design report, CERN-LHCC-97-032, http://cdsweb.cern.ch/record/343814.

[43] M. De Giorgi et al., Design and simulations of the trigger electronics for the CMS muon barrel chambers, Proceedings of the rst Workshop on Electronics for LHC Experiments, Lisbon Portugal (1995), CERN-LHCC-95-56, http://cdsweb.cern.ch/record/1062706.

[44] M. Aguilar-Benitez et al., Construction and test of the nal CMS barrel drift tube muon chamber prototype, Nucl. Instrum. Meth. A 480 (2002) 658.

[45] V. Barashko, Performance validation tests of the cathode strip chambers for CMS muon system, IEEE Nucl. Sci. Symp. Conf. Rec. 2 (2005) 827.

[46] R. Santonico and R. Cardarelli, Development of resistive plate counters, Nucl. Instrum. Meth. 187 (1981) 377.

[47] M. Abbrescia et al., Local and global performance of double-gap resistive plate chambers operated in avalanche mode, Nucl. Instrum. Meth. A 434 (1999) 244.

[48] CMS collaboration, The TriDAS project, technical design report. Volume 1: The level-1 trigger, CERN-LHCC-2000-038, http://cdsweb.cern.ch/record/706847.

[49] CMS collaboration, The TriDAS project, technical design report. Volume 2: Data acquisition and high-level trigger technical design report, CERN-LHCC-2002-026, http://cdsweb.cern.ch/record/578006.

[50] CMS Analysis Note: Muon Reconstruction in CMS Detector. CMS AN 2008/097.

[51] W. Adam, B. Mangano, T. Speer et al., Track Reconstruction in the CMS Tracker, CMS Note-2006/041 (2006).

[52] F.-P. Schilling, Track Reconstruction and Alignment with the CMS Silicon Tracker, CMS CR-2006/061 (2006).

[53] R. Fruhwirth, Application of Kalman ltering to track and vertex tting, Nucl. Instrum. Meth. A262 (1987) 444.

[54] R. Fruhwirth, W. Waltenberger and P. Vanlaer, Adaptive Vertex Fitting, CMS Note-2007/008 (2007).

[55] The CMS Collaboration, CMS Physics: Technical Design Report. Volume I: Detector Performance and Software, CERN/LHCC 2006-01, CMS TDR 8.1 (2006).

[56] C. Campagnari et al., Muon Identication in CMS, CMS AN-2008/098 (2008).

[57] T. Sjostrand, S. Mrenna, and P. Skands, PYTHIA 6.4 physics and manual, JHEP 05 (2006) 026, arXiv:hep-ph/0603175.

[58] G. Corcella et al., HERWIG 6.5 release note, arXiv:hep-ph/0210213.

[59] M. L. Mangano, M. Moretti, F. Piccinini, R. Pittau, and A. D. Polosa, ALPGEN, a generator for hard multiparton processes in hadronic collisions, JHEP 07 (2003) 001, arXiv:hep-ph/0206293.

[60] T. Gleisberg et al., SHERPA 1.alpha, a proof-of-concept version, JHEP 02 (2004) 056, arXiv:hep-ph/0311263.

[61] T. Stelzer and W. F. Long, Automatic generation of tree level helicity amplitudes, Comput. Phys. Commun. 81 (1994) 357371, arXiv:hep-ph/9401258.

[62] F. Maltoni and T. Stelzer, MadEvent: Automatic event generation with MadGraph, JHEP 02 (2003) 027, arXiv:hep-ph/0208156.

[63] S. Frixione and B. R. Webber, Matching NLO QCD computations and parton shower simulations, JHEP 06 (2002) 029, arXiv:hep-ph/0204244.

[64] CMS Collaboration, CMSSW, CMS reconstruction software, 2008. https://cmsdoc.cern.ch/cms/cpt/Software/html/General/.

[65] GEANT4 Collaboration, S. Agostinelli et al., GEANT4: A simulation toolkit, Nucl. Instrum. Meth. A506 (2003) 250303.

[66] ALEPH Collaboration, D. Buskulic et al., Nuc Instrum Meth. A360 (1995) 481-506.

[67] DELPHI Collaboration, P. Abreu et al., Nuc Instrum Meth. A378 (1996) 57-100.

[68] L3 Collaboration, A. Adam et al., Nucl. Instrum A383 (1996) 342-366.

[69] OPAL Collaboration, P.P. Allport et al., Nucl. Instrum A346 (1994) 476-495.

[70] SLD Collaboration, K. Abe et al., Nucl. Instrum A343 (1994) 74.

[71] CMS Analysis Note A. De Cosa, M. De Gruttola, S. Di Guida, F. Fabozzi, L. Lista, **P. Noli**: Determination of the $pp \to ZX \to \mu^+\mu^- X$ inclusive cross section with a simultaneous fit of Z yield, muon reconstruction efficiencies and High Level Trigger efficiency.

[72] Electroweak Physics group TWiki page: https://twiki.cern.ch/twiki/bin/view/CMS/TWikiEWK.

[73] Summer08 MC production TWiki page: https://twiki.cern.ch/twiki/bin/view/CMS/ProductionSummer2008d.

[74] CMS Analysis Note: P.Biallass et al., Parton Distribution Uncertainty Determination within CMSSW, CMS-AN-2009/049.